Features of the Charge Transfer in Nanoporous Silicon and Silicon Oxide with Adsorbed Water

E. N. Luk'yanova, S. N. Kozlov*, V. M. Demidovich, and G. B. Demidovich

Moscow State University, Moscow, 119899 Russia
* e-mail: kozlov@vega.phys.msu.su

Received December 26, 2000

Abstract—The experimental plots of electric conductivity versus temperature for a porous silicon and a silicon oxide with adsorbed water exhibit features at temperatures significantly below 0°C, which are related to an ice–water phase transition in nanopores of the solid matrix. © *2001 MAIK "Nauka/Interperiodica"*.

Systems featuring proton transport draw the attention of researchers because of the anomalously high mobility of protons, which is sometimes comparable with the mobility of electrons in solids [1]. Especially high proton mobilities are observed for proton conductors (such as water) confined in the pores of a solid matrix [2]. It was even suggested that proton transport might contribute to the anomalous high-temperature superconductivity in porous ceramics [2, 3]. We may therefore expect that a nanoporous solid–water system would exhibit unusual electrical properties at temperatures in the vicinity of the water–ice phase transition, where the conditions of proton transport in the system of hydrogen-bonded water molecules change significantly.

The problem of proton transfer via H_2O molecules adsorbed in the nanopores has become especially important in view of the concepts developed in recent years concerning a special physical structure of water dispersed in nanopores, in particular, of the "two-dimensional" ice structure [4–6]. At the same time, the considerable interest of researchers in the past decade was attracted to porous silicon (PS)—a material possessing unique physical properties [7] and compatible with the silicon technology widely employed in microelectronics. In this study, we attempted to detect features in the charge transport properties of the PS–water system at temperatures in the vicinity of the water–ice phase transition. In order to reveal the role of proton transport in the charge transfer process more certainly, we performed a series of experiments in the oxidized porous silicon (OPS)–water system.

PS layers with a thickness of 5–20 μm were created on a (100)-oriented *p*-Si single crystal surface by anodizing in an HF–ethanol (1 : 1) solution at a current density of 20 mA/cm^2. The PS layers formed under these conditions contain pores with a diameter of 2–3 nm and are characterized by a total porosity of ~70% [7, 8]. Some of the anodized samples were thermally oxidized in dry oxygen at a pressure of ~10^4 Pa. In order to prevent the nanoporous material from sintering at a high temperature, the oxidation was performed in two stages. First, a thin "stabilizing" oxide layer was formed by treating the samples in oxygen for 2 h at 300°C, after which the oxidation process was continued for 2.5 h at 750°C [7]. Finally, gas-permeable contacts with a diameter of 1 mm were formed on the sample surface by deposition in vacuum.

The samples were mounted in an experimental cell and kept for several days in vacuum. Then, the samples were exposed for 2–3 days to saturated water vapor until reaching a stationary conductivity of the silicon–PS(OPS)–metal structure (after contact with water vapor, the conductivity increased by several orders of magnitude [9]). For the conductivity measurements, the cell with a sample was cooled down to –20°C and slowly (over 2–3 h) heated to room temperature. Under these conditions, the sample temperature was always somewhat lower than that of the cell walls. Therefore, the water vapor pressure over the sample surface was always saturated and H_2O molecules were not desorbed from the pores. The sample temperature was monitored using a thermocouple pressed against the surface.

Figure 1 shows a typical curve of the current passing through a silicon–PS(H_2O)–metal sample structure plotted as a function of the temperature. As is seen, the sample conductivity rather sharply increases by almost one order of magnitude in the region of temperatures from –12 to –15°C. This jump in the conductivity is naturally explained by (i) an increase in the effective mobility of protons related to the appearance of additional degrees of freedom in water molecules as a result of the ice melting and by (ii) the formation of new trajectories for protons transferred via the system of hydrogen-bonded H_2O molecules. As is known, the melting temperature of small crystals may be significantly lower than that of a macroscopic crystal [10]. In particular, the melting temperature of ice in the PS nanocapillaries with a radius of 2–3 nm may decrease
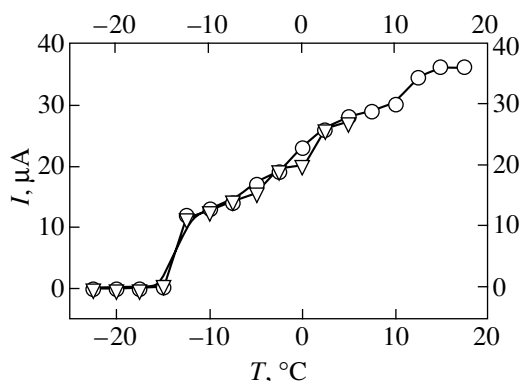
Fig. 1. A typical curve of the current versus temperature for a silicon–PS(H$_2$O)–metal sample with a porous silicon (PS) layer thickness of 7 μm measured at a voltage of +10 V applied to the metal electrode. Different symbols refer to two sequential experimental cycles.
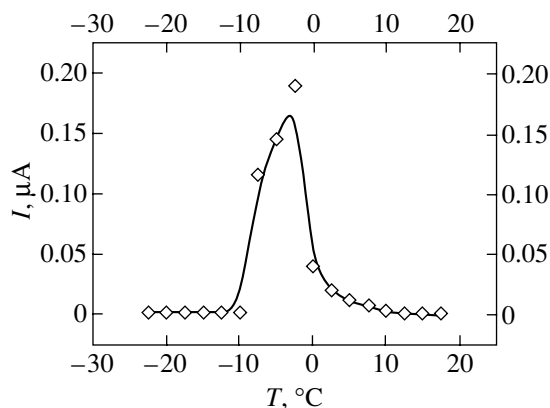
Fig. 2. A typical curve of the current versus temperature for a silicon–OPS(H$_2$O)–metal sample with an oxidized porous silicon (PS) layer thickness of 30 μm measured at a voltage of +10 V applied to the metal electrode.

by more than 10°C [11]. The observed jump in conductivity of the silicon–PS(H$_2$O)–metal structure is not related to irreversible deformation of a rather brittle PS structure accompanying the ice–water phase transition. Indeed, repeated experiments on the same sample completely reproduced the shape of the current versus temperature curve (Fig. 1).

In order to decrease contribution of the charge transfer via solid matrix to the conductivity of the porous matrix–water system, we performed experiments with OPS—a dielectric porous adsorbent possessing the same porosity as PS. Figure 2 shows a typical curve of the current versus temperature for a silicon–OPS(H$_2$O)–metal sample structure. In this case, a current through the structure is almost completely due to the proton transport in the system of hydrogen-bonded water molecules in the nanopores of OPS. For this reason, the current value is significantly lower as compared to that observed in the silicon–PS(H$_2$O)–metal structure (Fig. 1). As is seen in Fig. 2, there is still a

rather sharp jump in the sample conductivity at a temperature significantly below 0°C. A certain shift in the temperature at which the conductivity peak is observed (as compared to that in the silicon–PS(H$_2$O)–metal structure) is probably related to the effect of nanopore walls on the ice–water phase transition temperature. The surface of PS nanopores (coated with hydride groups [6]) is hydrophobic, whereas the surface of pores in OPS is partly hydrated and, hence, significantly less hydrophobic. As is known, a shift in the ice–water phase transition temperature in the adsorption layers is smaller on hydrophilic surfaces than on hydrophobic ones [11].

A rather unexpected fact is the decrease in conductivity of the silicon–OPS(H$_2$O)–metal structure observed when the temperature increases above −3…−2°C. It is not excluded that the nonmonotonic character of the current variation during gradual heating of the silicon–OPS(H$_2$O)–metal structure is related to the two-dimensional (2D) hexagonal structure of ice in the nanopores [4]. This ice behaves rather unusually and, for example, expands on heating [5]. As the temperature gradually increases, the 2D ice begins to melt first in deeper and thinner nanopores, while broader pore "openings" still remain "blocked" with ice. The liquid phase formed upon the 2D ice melting occupies a greater volume than the hexagonal ice and fills the voids available in the nanopores. This leads to the appearance of new pathways for the proton transport in nanocapillaries. As the temperature increases further, the ice "plugs" in the pore openings melt and water is partly squeezed out of the nanopores. Because of the inhomogeneous hydration of the pore surface, the nanocapillaries of water split into separate droplets, leading to a decrease in the sample conductivity. No such a decrease in conductivity is observed in silicon–PS(H$_2$O)–metal structure, probably, because of a significant contribution due to the electron transfer by the walls of PS nanopores.

Thus, we revealed features in the conductivity of a porous sold matrix with adsorbed water in the region of temperatures significantly below 0°C, which are explained by the ice–water phase transition in the nanocapillaries. It is essential that the method used for registration of the water–ice phase transition based on the conductivity measurements is considerably simpler as compared to the calorimetric and spectrophotometric techniques and allows the measurements to be performed on microobjects.

REFERENCES

1. D. Marx, M. E. Tuckerman, J. Hutter, and M. Parrinello, Nature **397**, 601 (1999).

2. V. Ya. Antonchenko, A. S. Davydov, and V. V. Il'in, *Principles of the Physics of Water* (Naukova Dumka, Kiev, 1991).

3. K. Kitazawa, K. Kishio, T. Hasegawa, and O. Nakamura, Jpn. J. Appl. Phys., Part 1 **26** (12), 1979 (1987).

4. M. Odelius, M. Bernasconi, and M. Parinello, Phys. Rev. Lett. **78** (14), 2855 (1997).

5. K. Koga, X. C. Zeng, and H. Tanaka, Phys. Rev. Lett. **79** (26), 5262 (1997).

6. J. Hu, X. D. Xiao, D. F. Ogletree, and M. Salmeron, Science **268**, 267 (1995).

7. A. G. Cullis, L. T. Canham, and P. D. Calcott, Appl. Phys. Rev. **82** (3), 909 (1997).

8. A. Halimaoui, in *Porous Silicon Science and Technology* (Springer-Verlag, Berlin, 1995), pp. 33–52.

9. V. M. Demidovich, G. B. Demidovich, S. N. Kozlov, and A. A. Petrov, Vestn. Mosk. Univ., Ser. 3: Fiz., Astron., No. 1, 55 (1998).

10. J. H. Bilgram, Phys. Rep. **153** (1), 1 (1987).

11. A. Bogdan, M. Kulmala, and N. Avramenko, Phys. Rev. Lett. **81** (5), 1042 (1998).

Translated by P. Pozdeev

A Quantum Loop in Magnetic Field and a Quantum Interference Rectifier

V. A. Geĭler* and I. Yu. Popov**

* Mordvinian State University, Saransk, Mordvinia, Russia
** Ioffe Physicotechnical Institute, Russian Academy of Sciences, St. Petersburg, 194021 Russia
Received October 9, 2000

Abstract—The electron transport in a curvilinear quantum wire exposed to a magnetic field was studied. A possible design of the quantum interference rectifier is suggested. © *2001 MAIK "Nauka/Interperiodica"*.

The rapid progress in nanoelectronics has led to the creation of principally new objects—quantum wires and dots—opening the way to such new devices as the quantum computer. To this end, it is necessary to develop various elements based on the quantum confinement principles. In connection with this, a number of publications have appeared suggesting the possible design of the quantum interference transistor, quantum capacitor, quantum switch, etc. (see, e.g., [1–8]). This is naturally accompanied by attempts at providing an adequate theoretical description of the quantum system. Since the description of any real system of this type is difficult, the analysis is usually restricted to various models. Proceeding from a pure theoretical analysis, it is possible to predict the properties of a real system and to find possible designs of the particular nanoelectronic devices.

The purpose of this study was to suggest possible designs of a quantum mesoscopic rectifier and a quantum switch controlled by an external magnetic field and to describe the electron transport in these quantum systems. The mathematical approach consists in solving the problem of scattering for a curvilinear quantum wire exposed to a magnetic field oriented perpendicularly to the system plane. The quantum wire is described in a one-dimensional approximation. The results of analysis are used to describe a new quantum device.

Let us consider a bent quantum wire (Fig. 1) composed of three parts: two semi-infinite straight segments (L_1 and L_2) connected by an arc (L_{arc}) with a radius r and a sector angle φ_0. We assume that the whole loop is placed into a magnetic field B, which is homogeneous in the region of the arc and falls to zero outside. On the L_1 and L_2 segments, the operator of momentum is $\hat{k} = -\hbar i d/dx$. In the L_{arc} region, we consider a calibration-invariant momentum operator in the form

$$\hat{p} = \frac{\hbar}{r}\left(\frac{1}{i}\frac{d}{d\varphi} + \Phi\right),$$

where $\Phi = \pi r^2 B/\Phi_0$, $\Phi_0 = 2\pi\hbar c/|e|$ is the magnetic flux

quantum, and the parameter (angle) φ varies within $0 \leq \varphi \leq \varphi_0$.

The system Hamiltonian is $H_1 = H_2 = \hat{k}^2/(2m)$ (on segments L_1 and L_2) and $H_{arc} = \hat{p}^2/(2m)$ (on L_{arc}). At points A_1 and A_2 (Fig. 1), the wavefunction must obey the calibration-invariant boundary relationships. At point A_1,

$$\Psi_1(0) = \Psi_{arc}(0), \quad \hat{k}\Psi_1(0) = -\hat{p}\Psi_{arc}(0), \quad (1)$$

and at point A_2,

$$\Psi_{arc}(\varphi_0) = \Psi_2(0), \quad \hat{p}\Psi_{arc}(\varphi_0) = \hat{k}\Psi_2(0). \quad (2)$$

The difference in signs in the boundary conditions (1) and (2) is related to the opposite directions selected in L_1 and L_{arc}.

A solution to the scattering problem is found in the following form:

$$\Psi_1(x) = \exp(ikx/\hbar), \quad \text{on} \quad L_1,$$
$$\Psi_{arc}(\varphi) = a_1\exp(ip_1 r\varphi/\hbar)$$
$$+ a_2\exp(ip_2 r\varphi/\hbar), \quad \text{on} \quad L_{arc},$$
$$\Psi_2(x) = b_1\exp(ikx/\hbar) + b_2\exp(-ikx/\hbar), \quad \text{on} \quad L_2,$$

where p_1 and p_2 are defined as

$$p_1 = k - \frac{\hbar\Phi}{r}, \qquad p_2 = -k - \frac{\hbar\Phi}{r}$$

and determined from the energy conservation law

$$\frac{1}{2m}\left(p + \frac{\hbar\Phi}{r}\right)^2 = \frac{k^2}{2m}.$$

Conditions (1) lead to the relationships

$$\begin{cases} a_1 + a_2 = 1, \\ a_1 - a_2 = -1, \end{cases}$$

from which we determine the coefficients a_1 and a_2 and the wavefunction

$$\Psi_{\mathrm{arc}}(\varphi) = \exp(-i(rk + \hbar\Phi)\varphi/\hbar).$$

Using conditions (2), we determine the coefficients b_1 and b_2

$$\begin{cases} b_1 + b_2 = \exp(-i(rk + \hbar\Phi)\varphi_0/\hbar), \\ b_1 = b_2 = -\exp(-i(rk + \hbar\Phi)\varphi_0/\hbar), \end{cases}$$

which yield the wavefunction

$$\Psi_2(x) = \exp(-i(rk + \hbar\Phi)\varphi_0/\hbar)\exp(-ikx/\hbar).$$

Finally, the coefficient of transmission from L_2 to L_1 is

$$t_{2 \to 1} = \exp(i(rk + \hbar\Phi)\varphi_0/\hbar). \tag{3}$$

The back propagation coefficient is determined by an analogous scheme using a solution in the following form:

$$\Psi_2(x) = \exp(ikx/\hbar),$$

$$\Psi_{\mathrm{arc}}(\varphi) = a_1\exp(ip_1r\varphi/\hbar) + a_2\exp(ip_2r\varphi/\hbar),$$

$$\Psi_1(x) = b_1\exp(ikx/\hbar) + b_2\exp(-ikx/\hbar).$$

The above procedure yields the coefficient of transmission from L_1 to L_2

$$t_{1 \to 2} = \exp(i(rk - \hbar\Phi)\varphi_0/\hbar). \tag{4}$$

Let us consider the possible applications of these results. Note that both transmission coefficients possess the absolute values equal to unity, differing only in the phase of the wavefunction. Therefore, the results can be manifested only in the interference effects. We can propose two possible interference devices.

The first device is a quantum switch (Fig. 2). In this device, the input electron wave coming from L_{in} splits into two identical waves at point C_1. These waves pass by the arcs L_1 and L_2 in opposite directions to meet at point C_2 with the phase gain factors $\exp[i(kr - \hbar\Phi)\varphi_0/\hbar]$ and $\exp[i(kr + \hbar\Phi)\varphi_0/\hbar]$. In the output segment L_{out}, the two waver superimpose. If the phase difference is $\pi + 2\pi n$, so that $\varphi_0\Phi = \pi/2 + \pi n$ (where n is an integer), the transmitted wave is absent. Thus, the system operates as a switch controlled by the magnetic field B.

The second device is the quantum interference rectifier (Fig. 3). Here, the input electron wave coming from L_{left} also splits into two at point C_1, but the phase is gained only in loop L_2 as described by the factor $\exp[2\pi i(kr - \hbar\Phi)/\hbar]$. Consider the case when $2\pi(kr/\hbar - \Phi) = 2\pi n$, so that $kr/\hbar - \Phi = n$ (where n is an integer). Then, the output wave superposition in L_{right} yields the
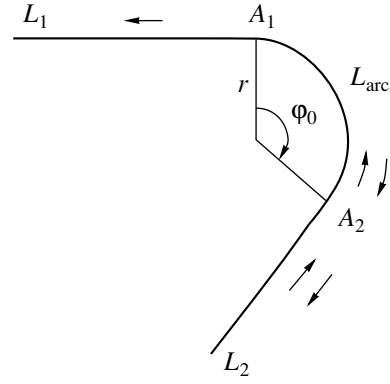
Fig. 1. Curvilinear quantum-wire loop with a radius r and an arc sector angle φ_0.
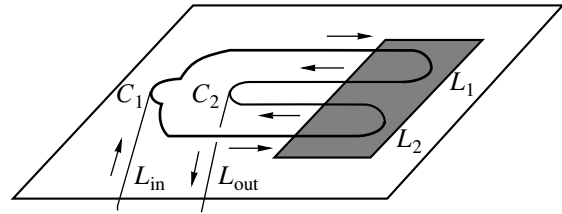
Fig. 2. Quantum switch. Shaded area corresponds to nonzero magnetic field. Fig. 2. Quantum switch. Shaded area indicates nonzero magnetic field.
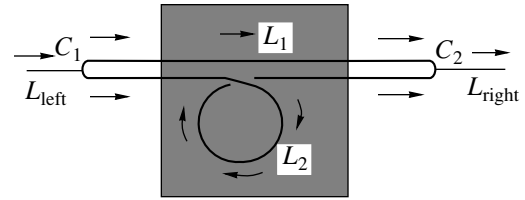
Fig. 3. Quantum rectifier. Shaded area corresponds to nonzero magnetic field.

coefficient of transmission from left to right equal to unity. In the reverse direction, the phase gain factor $\exp[2\pi i(kr + \hbar\Phi)/\hbar]$. In the case when $2\pi(kr\hbar^{-1} + \Phi) = \pi + 2\pi n'$, we obtain $kr\hbar^{-1} + \Phi = 1/2 + n'$ (where n' is an integer). Then the output wave superposition in L_{left} yields the coefficient of transmission from right to left equal to zero. Thus, provided that both conditions are fulfilled ($kr\hbar^{-1} - \Phi = n$, $kr\hbar^{-1} + \Phi = 1/2 + n'$), the proposed device operates as a rectifier. Taking into account that k^2 is fixed at the Fermi level, the two conditions can be simultaneously satisfied by varying two parameters (r and B).

REFERENCES

1. F. Sols, F. Macucci, U. Ravaioli, and K. Hess, Appl. Phys. Lett. **54**, 350 (1989).

2. P. Exner and P. Seba, Phys. Lett. A **129**, 477 (1988).

3. W. Porod, Z. Shao, and C. S. Lent, Phys. Rev. B **48**, 8495 (1993).

4. C. W. Beenakker and H. van Houten, in *Solid State Physics: Advances in Research and Applications*, Ed. by H. Ehrenreich and D. Turnbull (Academic, San Diego, 1991), Vol. 44, p. 1.

5. M. Büttiker, Phys. Rev. Lett. **57**, 1761 (1986).

6. K. Nicolic and R. Sordan, Phys. Rev. B **58**, 9631 (1998).

7. B. S. Pavlov, I. Yu. Popov, and O. S. Pershenko, Izv. Vyssh. Uchebn. Zaved., Priborostr. **45** (1-2), 31 (2000).

8. B. S. Pavlov, I. Yu. Popov, V. A. Geyler, and O. S. Pershenko, Europhys. Lett. **52**, 133 (2000).

Translated by P. Pozdeev

The Electric Conductivity of a Laser Plasma Excited at a Ceramic Surface

A. V. Gradoboev

Tomsk Polytechnical University, Tomsk, Russia
e-mail: grad@media.tomsk.su
Received December 26, 2000

Abstract—The electric conductivity of a laser plasma, excited at the surface of a 22KhS ceramics by a pulsed laser radiation, was studied in the presence of an external electric field oriented perpendicularly to the laser beam direction. Depending on the output laser power density, there are three characteristic regimes: (i) the absence of a laser plasma possessing electric conductivity; (ii) the formation of a conducting plasma in which the current is proportional to the laser power density and to the square of the applied electric field strength; (iii) the formation of a conducting plasma in which the current depends linearly both on the laser power density and on the applied electric field strength. © *2001 MAIK "Nauka/Interperiodica"*.

At present, there is a large amount of data concerning various characteristics of the plasma excited by laser radiation at the surface of solids [1–4]. These data were obtained for the most part by measuring the X-ray emission [4], optical [5–6], and thermal [7] properties of the laser-induced plasmas. A considerably smaller number of investigations were devoted to the properties of laser plasmas in applied electric fields [8].

When a pulsed laser radiation acts upon a solid surface, a plasma is formed at the surface which consists of the ions from ambient medium and/or the target material. The resulting plasma torch decays with time as a result of diffusion of the plasma components into the environment and/or their adsorption on the target surface. Application of an external electric field to the region of plasma torch leads to the concentration of the plasma components on the corresponding electrodes. This process depends on the electric characteristics of the plasma components and can be used to control the process of the plasma torch decay. Practical implementation of the process of field-controlled plasma torch decay may increase the efficiency and quality of the target processing and reduce the probability of redeposition of the laser-evaporated target material.

Our purpose was to study the electric conductivity of a laser plasma excited at a ceramic surface and detect variations caused by application of an external electric field.

We have studied a plasma excited at the surface of a widely used commercial ceramic of the 22KhS type by radiation of a pulsed laser at a wavelength of 1.06 μm, pulse duration 1 ms, and a power density W_p ranging from 3×10^4 to 1×10^6 W/cm^2. This radiation power density does not produce destruction in ceramic samples or metal electrodes. The W_p value was controlled by focusing the laser beam or by changing the laser

regime. The experiments were conducted in air at atmospheric pressure and room temperature. The 22KhS ceramic targets had a rectangular shape.

Figure 1 shows a schematic diagram of the experimental setup used for the plasma conductivity investigation. A ceramic sample *1* (made of the 22KhS ceramics) was mounted between electrodes *2* and *3*. By changing the geometry of sample *1* and the voltage applied to the electrodes from source *4*, it was possible to control within broad limits the electric field strength acting upon the sample. A pulsed radiation beam from laser *5* was normally incident onto the sample surface and was perpendicular to the electric field direction. The plasma current measured by a storage oscillograph *6* was proportional to a voltage drop on a high-precision resistor R_c. The output signal was detected using the laser source and the storage oscillograph operated in a lock-in mode provided by a synchronization unit *7*. It must be noted that the laser beam cross section in all experiments was markedly greater than the total area of the sample together with metal electrodes.

The electric conductivity of a plasma excited at the surface of a ceramic target was characterized by the
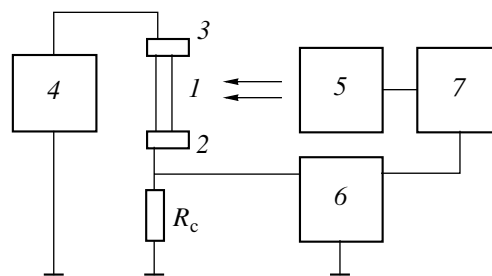
Fig. 1. A schematic diagram of the experimental setup used to study the plasma conductivity in an applied electric field (see the text for explanation).

I, A
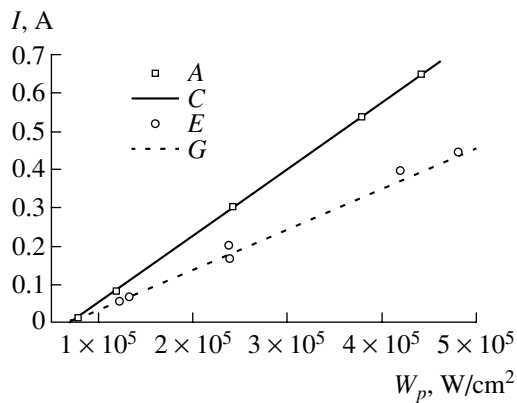
Fig. 2. The plots of plasma current I versus laser power density W_p for different values of the field strength applied to a 22KhS ceramic sample: (A, C) 15 V/cm; (E, G) 7.5 V/cm (lines C and G show the results of statistical processing of the experimental data).

I, A
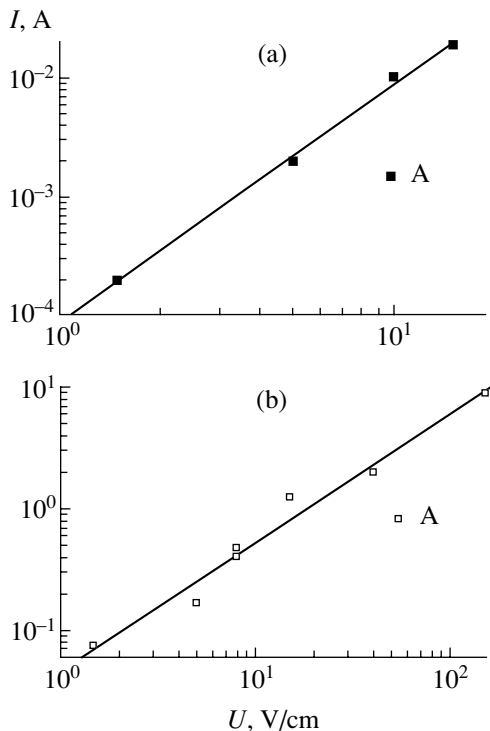
Fig. 3. The plots of plasma current I versus electric field strength U measured at various values of the laser power density: (a) region II, $W_p = 8.7 \times 10^4$ W/cm^2; (b) region III, $W_p = 4.7 \times 10^5$ W/cm^2.

plasma current measured as the amplitude of the current pulse passing through the plasma at a preset electric field strength and a given laser power density. The time characteristics of the plasma current relaxation are a subject for special consideration that falls outside the scope of this publication.

Figure 2 shows plots of the plasma current versus laser power density for different values of the applied field strength. As is seen, there is a clearly pronounced

power threshold for the appearance of plasma possessing electric conductivity, the level of which is about 7×10^4 W/cm^2. Another important result is that the plasma current is directly proportional to the laser power density.

It was also of interest to study the plasma current I as a function of the electric field strength U. Figure 3 shows such curves measured at various values of the laser power density. As is seen from these data, there exists a region of W_p values in which the plasma current is proportional to the square of the electric field strength (see Fig. 3a) and another region in which the plasma current is a linear function of the field strength (Fig. 3b). The plot of plasma current versus The results of our experiments clearly indicated the boundaries of these characteristic regions featuring the formation of conducting plasmas.

Finally, we will formulate the main results and conclusions. The experiments revealed three characteristic regions of the laser power density from the standpoint of the formation of conducting plasma. In region I ($W_p < 7 \times 10^4$ W/cm^2), no laser plasma possessing electric conductivity is formed near the surface of the 22KhS ceramic target. In region II (7×10^4 W/cm$^2 < W_p < 1 \times 10^5$ W/cm^2), the laser radiation excites a conducting plasma in which the current is proportional to the laser power density and to the square of the applied electric field strength. In region III ($W_p > 1 \times 10^5$ W/cm^2), the laser radiation also excites a conducting plasma in which the current linearly depends both on the laser power density and on the applied electric field strength. This behavior is retained up to $W_p = 1 \times 10^6$ W/cm^2.

Further investigations are necessary to establish characteristics of the plasma current relaxation with time and to study the plasma conductivity as a function of the laser radiation wavelength and pulse duration.

REFERENCES

1. J. Ready, *Effects of High Power Laser Radiation* (Plenum, New York, 1971; Mir, Moscow, 1974).
2. M. A. Sultanov, Dokl. Akad. Nauk Tadzh. SSR **29** (10), 598 (1986).
3. A. N. Panchenko and V. F. Tarasenko, Fiz. Plazmy **14** (6), 761 (1988) [Sov. J. Plasma Phys. **14**, 450 (1988)].
4. D. R. Kania, J. Appl. Phys. **66** (5), 1935 (1989).
5. M. Autric, P. Vigliano, D. Astic, *et al.*, Proc. Soc. Photo-Opt. Instrum. Eng. **1020**, 103 (1988).
6. V. A. Podvyaznikov, E. L. Tyurin, and V. K. Chevokin, Preprint No. 110, Inst. Obshch. Fiz. Akad. Nauk SSSR (General Physics Institute, USSR Academy of Sciences, 1988), pp. 1–30.
7. M. G. Anuchin and V. V. Volenko, Kvantovaya Élektron. (Moscow) **16** (2), 311 (1989).
8. V. P. Volkov, P. A. Skiba, and A. G. Sechko, Vestsi Akad. Navuk BSSR, Ser. Fiz-Mat. Navuk, No. 2, 65 (1992).

Translated by P. Pozdeev

Adsorbed Molecules Form Ordered Structures on the Surface of Metals Exposed to an Electric Field

S. V. Zaĭtsev

Institute of Theoretical and Experimental Physics, State Scientific Center of the Russian Federation, Moscow, Russia
e-mail: Sergey.Zaitsev@itep.ru
Received December 13, 2000

Abstract—Submonomolecular films deposited onto a metal surface in an electric field exhibit the phenomenon of self-organization. The ordering is manifested by the formation of molecular chains featuring the mass transfer. This results in the appearance of a stable dynamic network structure, which exists within a certain optimum temperature interval. It is suggested that this phenomenon is related to the electric interactions in a system of dipoles, one end of each dipole being free and another moving on the substrate surface with friction. Modeling of the evolution of this system with time qualitatively agrees with the experiment. These results can be used in high-voltage and vacuum electronics, space technologies, and nanoelectronics. © 2001 MAIK "Nauka/Interperiodica".

The progress of technology is now related to a considerable extent to the advances in nanotechnology, which explains the considerable interest in the development of methods for controlling the molecular motions. It is especially important not only to control individual molecules (there are considerable achievements in this respect) but to provide for the production of "large-scale" molecular structures as well. The passage to this level now meets considerable difficulties [1]. A possible way of solving this task consists in using the self-organization effects. This requires a thorough investigation of the response of molecular associations to various external factors.

A powerful means of controlling the motions of molecules is offered by the electric field. We have studied evolution of a submonomolecular film deposited from the gas phase onto a conducting substrate in an electric field oriented perpendicularly to the substrate surface. The experiments were performed with molecules possessing a large dipole moment (water, naphthalene) and a series of metal substrates including tungsten, molybdenum, and stainless steel. The substrates had the shape of a needle with a ball at the tip formed by fusion in an electric discharge. The ball radius could be controlled by electropolishing. The experiments were usually performed using balls with a diameter <2 μm. The sample was placed into a vacuum chamber containing adsorbate molecules in the gas phase. Mounted at a distance of 3 cm in front of the ball, there was a system of secondary-electron microchannel plates (SEMCPs) and a screen emitting light under the electron impact conditions. The serial SEMCP arrangement provided a total gain on the order of 10^8, which allowed both individual molecules and adsorbed films to be observed at relatively weak electric field strengths (exposed to the field with a strength $>10^8$ V/m, the adsorbed molecules are field-desorbed from the metal surface).

When the electric field with a strength from 10^6 to 10^8 V/m is created at the sample surface, the molecules in the gas phase are polarized and adsorbed on the ball surface. The field strength at the free ends of adsorbed molecules is locally higher as compared to the average value on the surface. This near-surface region features most probable field ionization of the residual gases and other molecules not having reached the metal surface. The ions are accelerated by the electric field toward the microchannel plate and create an image on the screen. The projection effect ensured acceleration sufficient for imaging individual molecules on the surface at a minimum curvature radius of the sample (below 0.1 μm).

The sample surface is covered, as a rule, by a monomolecular adsorption film. This agrees with the existing theoretical notions, according to which the field ionization of a molecule is hindered when the molecule approaches the charged surface to a distance shorter than certain critical value [2]. When the number of adsorbed molecules increases, the molecules tend to unite so as to form planar aggregates. Our observations of such molecular structures revealed certain regularities in their behavior. The planar aggregates tend to form either at the sample surface (where the field strength is maximum) or at the local protrusions on the surface. The aggregates permanently feature collective motions, which give rise to periodical formation of "protuberances" representing molecular flows that protrude out and are pulled back in a fraction of second. If an adjacent planar aggregate occurs on the surface at a distance comparable to the lengths of such protrusions, the protuberances may touch one another and form a
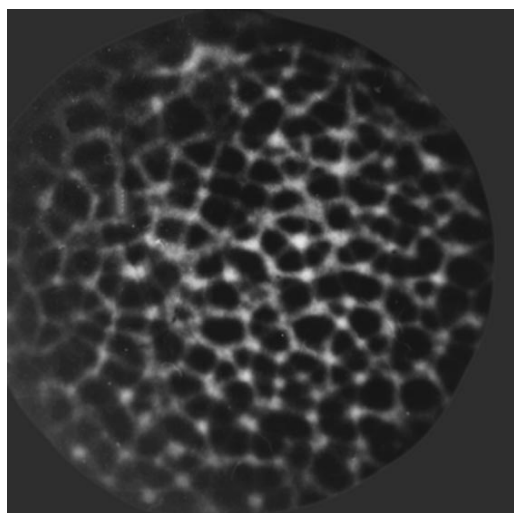
Fig. 1. A network of adsorbed water molecules, which is formed on a tungsten ball surface under the action of electric field (ball diameter, ~1 μm).
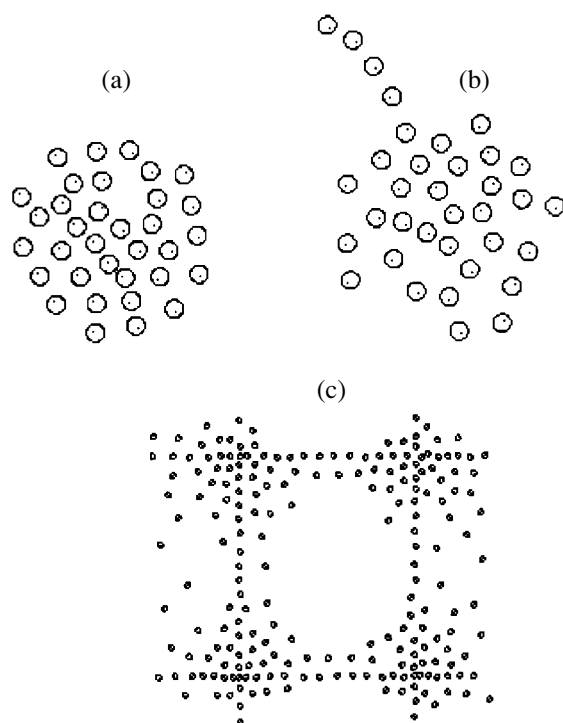
Fig. 2. The results of mathematical modeling of evolution of a submonolayer film adsorbed on a metal substrate in the electric field perpendicular to the substrate surface: (a) a disordered group of molecules occurs for some time in a stable state; (b) "protuberances" in the form of linear chains are periodically protruding from the group; (c) four molecular groups occurring in a square lattice sites are linked by the dynamic bonds of protruding chains.

long-living contact. The contact may break with time, but some other form instead so that the general character of the structure is retained.

Behavior of the adsorbed film depends on the substrate temperature. Most stable structure form at room temperature (Fig. 1). Increasing the substrate temperature above 100°C led to image blurring, while cooling led to the disappearance of the ordering signs.

We may suggest that the observed behavior of adsorbed molecules is related to electric interactions in a system comprising a large number of dipoles having one end free and another moving on the substrate surface with friction. In order to check for this hypothesis, we performed a mathematical modeling of the evolution of a system of such dipoles occurring on the surface and experiencing attraction toward the center and random thermal fluctuations. The results of modeling are presented in Figs. 2a–2c. It was found that some groups of dipoles exhibit, after a certain period of relative stability (Fig. 2a), the development of ordered internal flows. This results in the periodical formation of "protuberances" representing particle chains (Fig. 2b) living for some time, after which the system returns back to the completely disordered state. If other groups particles occur at a distance comparable with the length of protruding chains, the counterflows lead to the formation of long-living contacts between these groups (Fig. 2c). Long-term observations show that these interconnecting chains serve as paths for the substance transfer (exchange) between groups.

Thus, the model shows a qualitative agreement with experiment. This by no means implies that all details of the microscopic mechanism are established, since the possibilities of using numerical modeling for the analysis of complex systems are restricted [3]. Nevertheless, the results of preliminary analysis give us hope that the proposed model is capable of predicting many aspects in the behavior of films adsorbed on metal electrodes which play key roles in many phenomena such as electric breakdown and parasite noise in electronic devices. We believe that the established features may be useful in solving the problem of adsorbed films detrimentally affecting space vehicles. On the other hand, the observed self-organization phenomenon can be used for the obtaining of nanostructures. A special feature of these structures is the ability of self-healing, although the existence of such systems requires a permanent energy supply.

REFERENCES

1. M. Hoummady and H. Fujita, Nanotechnology **10** (1), 29 (1999).

2. M. K. Miller and G. D. W. Smith, *Atom Probe Microanalysis: Principles and Applications to Material Problems* (Materials Research Society, Pittsburgh, 1989; Mir, Moscow, 1993).

3. G. Nicolis and I. Prigogine, *Exploring Complexity* (Freeman, New York, 1989; Mir, Moscow, 1990).

Translated by P. Pozdeev

The *P–H–T* Effects on the Electric Resistance and Magnetoresistance of La$_{0.7}$Sr$_{0.1}$Pb$_{0.2}$MnO$_3$ Single Crystal Films

S. S. Kucherenko, V. P. Pashchenko, P. I. Polyakov*, S. I. Khartsev, and V. A. Shtaba

Donetsk Physicotechnical Institute, National Academy of Sciences of Ukraine, Donetsk, Ukraine
* e-mail: poljakov@host.dipt.donetsk.ua
Received December 6, 2000

Abstract—The effects of high hydrostatic pressures (P) and magnetic fields (H) in a broad temperature range (T = 77–325 K) on the electric resistance (R) and magnetoresistance ($\Delta R/R_0$) was studied in laser-deposited La$_{0.7}$Sr$_{0.1}$Pb$_{0.2}$MnO$_3$ single crystal films on (100)-oriented SrTiO$_3$ substrates. A maximum response to the P and H variations was observed in the temperature interval of phase transitions (T = 310–325 K). A growth in the pressure P leads to an increase in both R and $\Delta R/R_0$ values, while an increase in the magnetic field strength H is accompanied by an increase in $\Delta R/R_0$ and a drop in the electric resistance R of the single crystal films studied. © 2001 MAIK "Nauka/Interperiodica".

Introduction. Rare-earth (RE) magnets with a perovskite structure, featuring the giant magnetoresistance (GMR) effect, have been extensively studied in recent years [1, 2]. The task of elucidating the nature of the GMR phenomenon and selecting high-quality magnetoresistive materials is facilitated by investigations of the effects of pressure, magnetic field strength, and temperature on the structure and properties of RE magnets [3].

Among the modern RE magnets, most promising are the manganite-lanthanum perovskites doped with divalent cations, such as La$_{1-x}^{3+}$Me$_x^{2+}$Mn$_{1-x}^{3+}$Mn$_x^{4+}$O$_3^2$, where Me^{2+} = Ca^{2+}, Sr^{2+}, Ba^{2+}, Pb^{2+} [4]. The optimum properties, that is, large GMR parameters and high Curie temperatures (T_C), the metal–semiconductor transition (T_R), and the magnetoresistance peak (T_P), are exhibited by the compositions with x = 0.33 [5]. There is a large variety of the material types, including bulk ceramics [6] and single crystals [7], as well as thin films, obtained by chemical vapor deposition (CVD) [8], magnetron sputtering [9], and laser deposition techniques [10]. We believe that the laser-deposited thin-film materials possess the most interesting properties and have the best prospects.

Taking into account both the current importance and fundamental interest in studying the effects of isostatic pressures [11], we have investigated the properties of laser-deposited RE manganite single crystal films in a broad range of pressures, temperatures, and magnetic field strengths.

Sample preparation and characterization methods. Thin single crystal films of the La$_{0.7}$Sr$_{0.1}$Pb$_{0.2}$MnO$_3$ composition were obtained by the laser sputtering of single-phase ceramic targets (with a diameter of 24 mm and a thickness of 3–5 mm) with deposition onto (100)-oriented SrTiO$_3$ substrates. According to the X-ray diffraction data, the magnetoresistive samples possessed a rhombohedrally distorted perovskite structure ($R\bar{3}c$).

The electric resistance of thin films was measured by the four-point-probe technique in a broad range of temperatures T = 77– 350 K at various hydrostatic pres-
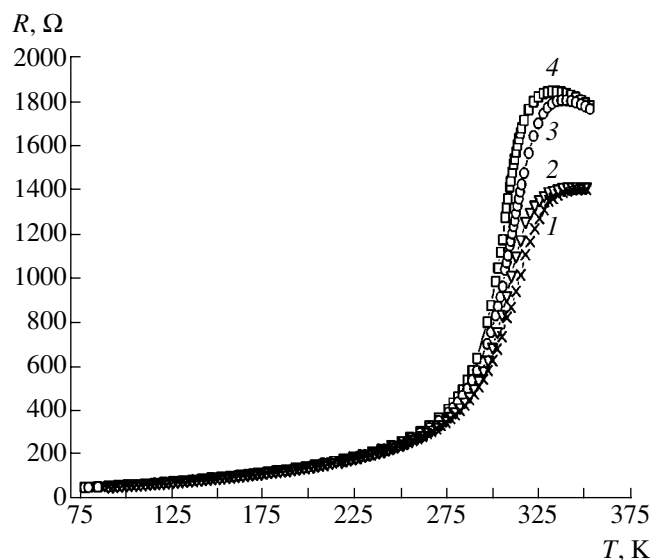
Fig. 1. Temperature dependence of the electric resistance of a laser-deposited La$_{0.7}$Sr$_{0.1}$Pb$_{0.2}$MnO$_3$ single crystal film measured at limiting values of the hydrostatic pressure P and applied magnetic field strength H: (*1*) P = 1.26 GPa, H = 8 kOe; (*2*) P = 1.26 GPa, H = 0; (*3*) P = 0, H = 8 kOe; (*4*) P = 0, H = 0.

$\Delta R/R_0$, %
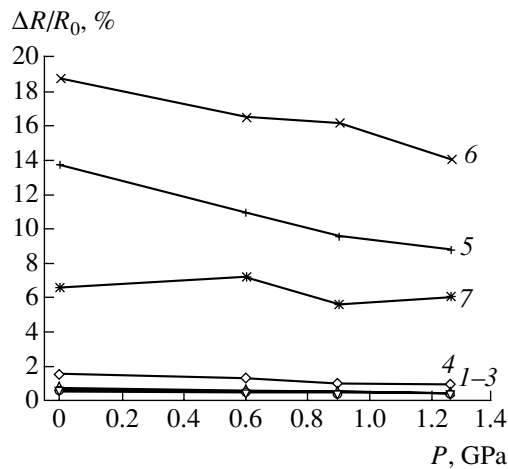
Fig. 2. The plots of magnetoresistance versus pressure measured at $H = 8$ kOe and various temperatures $T = 100$ (*1*), 150 (*2*), 200 (*3*), 250 (*4*), 300 (*5*), 310 (*6*), and 325 K (*7*).

$\Delta R/R_0$, %
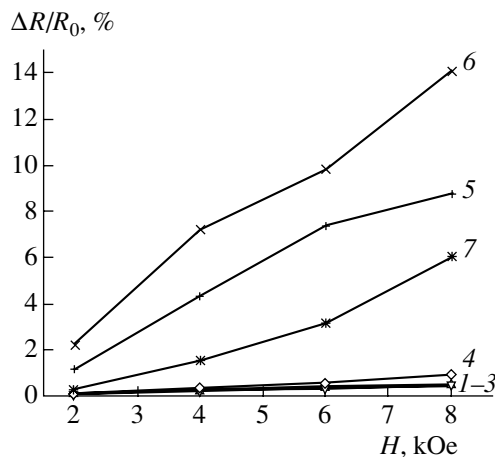
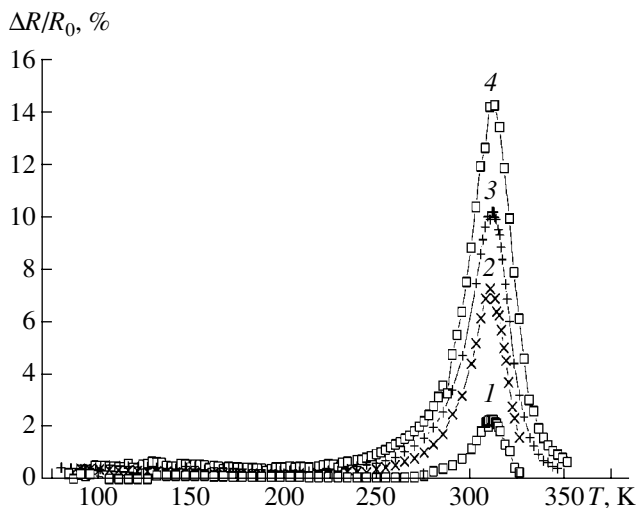**Fig. 3.** The plots of magnetoresistance versus pressure measured at $P = 1.26$ GPa and various temperatures $T = 100$ (*1*), 150 (*2*), 200 (*3*), 250 (*4*), 300 (*5*), 310 (*6*), and 325 K (*7*).

$\Delta R/R_0$, %

Fig. 4. The plots of magnetoresistance versus temperature measured at $P = 1.26$ GPa and various magnetic field strengths $H = 2$ (*1*), 4 (*2*), 6 (*3*), and 8 kOe (*4*).

sures $P = 0$–1.26 GPa and magnetic field strengths $H = 2, 4, 6,$ or 8 kOe. The resistance of a sample mounted in a high-pressure vessel [12] was measured with the magnetic field switched on (R_H) and off (R_0) at various temperatures (determined by measuring the resistance of a probing copper coil).

The experimental error of determination was 1% for the temperature, 1.5% for magnetic field strength, 0.01% for the electric resistance, 0.1% for the magnetoresistance $\left(\dfrac{\Delta R}{R_0} = \dfrac{R_0 - R_H}{R_0} \right)$, and 3% for the pressure.

Experimental results and discussion. Figure 1 shows the effect of minimum and maximum values of the hydrostatic pressure and applied magnetic field strength on the electric resistance of a $La_{0.7}Sr_{0.1}Pb_{0.2}MnO_3$ single crystal film measured in a broad temperature range. As seen, the high hydrostatic pressure and magnetic field produce analogous effects: an increase in P and H leads to a decrease in the sample resistance in the region of temperatures ($T_{R\max}$) corresponding to maximum resistance (i.e., in the vicinity of the metal-semiconductor phase transition). There is also a weak tendency of $T_{R\max}$ to grow with P and H.

It was of interest to follow the influence of high hydrostatic pressures on the magnitude of the magnetoresistance effect measured at various temperatures (Fig. 2). At elevated temperatures, a growth in the pressure leads to a decrease in the magnetoresistance ($\Delta R/R_0$), while a decrease in the temperature makes the $\Delta R/R_0$ value virtually independent of pressure. At low temperatures, the system is poorly sensitive even to high isostatic pressures (Fig. 2), as well as to the magnetic field (Fig. 3). There is a certain temperature interval (300–310 K) in which the effects of pressure P (Fig. 2) and magnetic field strength H (Fig. 3) on the magnetoresistance are most pronounced.

Of special interest is the effect of temperature and magnetic field on the magnetoresistance peak at $P = 1.26$ GPa (Fig. 4). As the magnetic field strength increases from 2 to 8 kOe, the magnetoresistance $\Delta R/R_0$ in the region of the phase transition ($T_p \approx 310$ K) grows from 2 to 15%, that is, by a factor of 7.5. We believe that the observed P–H–T effects on the electrical and magnetic properties of the samples studied are related primarily to the elastic and reversible changes in local states of manganese ions.

Conclusions. The complex experimental investigation of the effect of high hydrostatic pressures ($P = 0$–1.26 GPa), applied magnetic field ($H = 0$–8 kOe), and temperature ($T = 77$–350 K) on the resistance and magnetoresistance of laser-deposited $La_{0.7}Sr_{0.1}Pb_{0.2}MnO_3$ single crystal films showed the following.

1. Maximum values of the electric resistance are observed at $T_{R\max} \approx 325$ K, while the maximum magnetoresistance effect is observed at $T_P \approx 310$ K.

2. In the region of phase transitions, both the electric resistance and the magnetoresistance effect decrease with increasing hydrostatic pressure.

3. An increase in the applied magnetic field strength H leads to a decrease in R and an increase in $\Delta R/R_0$ in the temperature region of phase transitions ($T = 310$–325 K).

4. The influence of P and H on the electric resistance and magnetoresistance is maximum in the temperature interval of phase transitions and decreases both at low (77–250 K) and elevated (325 K) temperatures (i.e., far from $T_{R\max}$ and T_P).

REFERENCES

1. R. Mahendrian, S. K. Tiwary, A. K. Raychaudhuri, *et al.*, Phys. Rev. B **53** (6), 3348 (1996).

2. É. L. Nagaev, Usp. Fiz. Nauk **166** (8), 833 (1996) [Phys. Usp. **9**, 781 (1996)].

3. V. G. Bar'yakhtar, A. N. Pogoriliy, N. A. Belous, and A. I. Tovstolytkin, J. Magn. Magn. Mater. **196–197**, 525 (1999).

4. A. P. Ramizez, J. Phys.: Condens. Matter **9**, 8171 (1997).

5. A. Urushibara, Y. Moritomo, A. Asamitsu, *et al.*, Phys. Rev. B **51** (20), 14106 (1995).

6. V. P. Pashchenko, S. I. Khartsev, O. P. Cherenkov, *et al.*, Neorg. Mater. **35** (12), 1509 (1995).

7. A. M. Balbashov, M. K. Gubkin, V. V. Kireev, *et al.*, Zh. Éksp. Teor. Fiz. **117** (3), 542 (2000) [JETP **90**, 474 (2000)].

8. Yu. P. Sukhorukov, N. N. Lashkareva, E. A. Gan'shina, *et al.*, Pis'ma Zh. Tekh. Fiz. **25** (14), 6 (1999) [Tech. Phys. Lett. **25**, 551 (1999)].

9. S. I. Khartsev, V. N. Krivoruchko, and V. P. Pashchenko, Fiz. Nizk. Temp. **23** (8), 840 (1997) [Low Temp. Phys. **23**, 631 (1997)].

10. R. von Helmolt, J. Wecker, B. Holzapfel, *et al.*, Phys. Rev. Lett. **71** (14), 2331 (1993).

11. V. E. Arkhipov, V. S. Gaviko, K. M. Demchuk, *et al.*, Pis'ma Zh. Éksp. Teor. Fiz. **71** (3), 169 (2000) [JETP Lett. **71**, 114 (2000)].

12. A. V. Oleĭnik, P. I. Polyakov, and V. G. Synkov, Fiz. Tekh. Vys. Davleniĭ **4** (1), 88 (1994).

Translated by P. Pozdeev

Cleavage in the K8 Glass
under Submicrosecond Impact Loading

Yu. V. Sud'enkov

St. Petersburg State University, St. Petersburg, Russia
Received January 24, 2001

Abstract—The dynamic strength of an optical glass of the K8 type was studied under submicrosecond impact loading conditions. A 80-ns-long pressure impact was generated by a laser radiation pulse acting upon an aluminum foil. The free sample surface velocity was measured by a laser differential interferometer. The onset of fracture at the free surface was detected using a He–Ne laser radiation reflected from a crack appearing as a result of the glass cleavage. The experimental data on the dynamic strength of a glass under submicrosecond impact loading conditions are obtained for the first time. For the K8 glass studied, the critical cleavage stress amounts to 0.45 ± 0.03 GPa. Experimental investigations of the time characteristics of the fracture process, as well as the results of a fractographic analysis of the cleavage zone, do not unambiguously confirm the existence of the stage of damage accumulation during the fracture of inorganic glasses. © 2001 MAIK "Nauka/Interperiodica".

Inorganic glasses traditionally serve as model materials for the investigation of mechanical properties and fracture of brittle materials [1, 2]. However, data on the dynamic strength of inorganic glasses are few and rather contradictory [3, 4], and no information at all is available for the loading durations on the order of (or shorter than) 10^{-7} s. For this reason, and taking into account the wide use of the K8 glass in optical devices, we have studied the dynamic strength of this material.

The samples were loaded by 80-ns-long pressure pulses generated by a pulsed laser radiation acting upon an aluminum foil contacting with the sample [5]. The planar loading conditions were ensured by taking special measures to provide for a uniform energy distribution over the laser-irradiated sample area. The K8 glass samples had the shape of cylinders with a diameter of 24 mm and a height of 22 mm. The loaded area on a polished edge of a sample had a diameter of 10 mm. This ratio of the sample and loaded area diameters ensured that the unloading waves came from the cylinder walls with a delay time ($>2 \times 10^{-6}$ s) exceeding the loading impact duration. The longitudinal sound velocity in the K8 glass measured in the experiment was $c_1 = 5890 \pm 30$ m/s.

The velocity of motion of the free sample surface was measured by a laser differential interferometer with a stabilized working point, equipped with a photoelectric band counter [5]. Measuring the free surface velocity, we simultaneously determined the moment of sample fracture by detecting radiation of a He–Ne laser reflected from the plane appearing as a result of the sample cleavage. For this purpose, the laser beam was directed at an angle of ~45° onto the free sample surface and focused near the center of the loaded area.

Upon the sample fracture, the light reflected from the cleavage surface was collected with an objective focused on the cleavage zone (~0.2 mm below the surface) and detected by a photomultiplier. The output signals from photodetectors were measured with a TDS-754C.C oscillograph synchronized by signals from a photodiode receiving a part of the high-power pulsed laser radiation. The time resolution of the measuring system was not worse than 2 ns.

Figures 1a and 1b show the electric signals from photodetectors of the interferometer (curve *1*) and the reflected light monitor (curve *2*) in cases when the loading impact did not lead to fracture of the sample (Fig. 1b representing a magnified initial fragment of Fig. 1a). As is seen, a signal from the reflected light monitor is absent (curve *2*). The free surface displacement represents a single shock pulse (curve *1*) with a duration of $t_{sh} = 80$ ns, corresponding to the compression pulse coming to the surface at a time instant of $t = 3.76$ μs. The free surface velocity is $v = 18.2$ m/s, which corresponds to a stress magnitude of 0.136 GPa in the compression wave.

Figures 1c and 1d show the analogous signals measured in the case when the load was sufficient to cause fracture near the free sample surface. Here, the free surface velocity is $v = 58.6$ m/s (curve *1*), which corresponds to a stress of 0.438 GPa. The observed pattern is characteristic of the sample fracture by the cleavage mechanism. The loading pulse is followed by a cleavage pulse appearing as a result of reflection of the extension pulse from the fracture surface. The time delay of the cleavage pulse relative to the loading pulse must be equal to $t_s = 2h/c_1$, where h is the distance from the free surface to the cleavage surface. The oscillogram of the reflected light (curve *2*) displays a signal
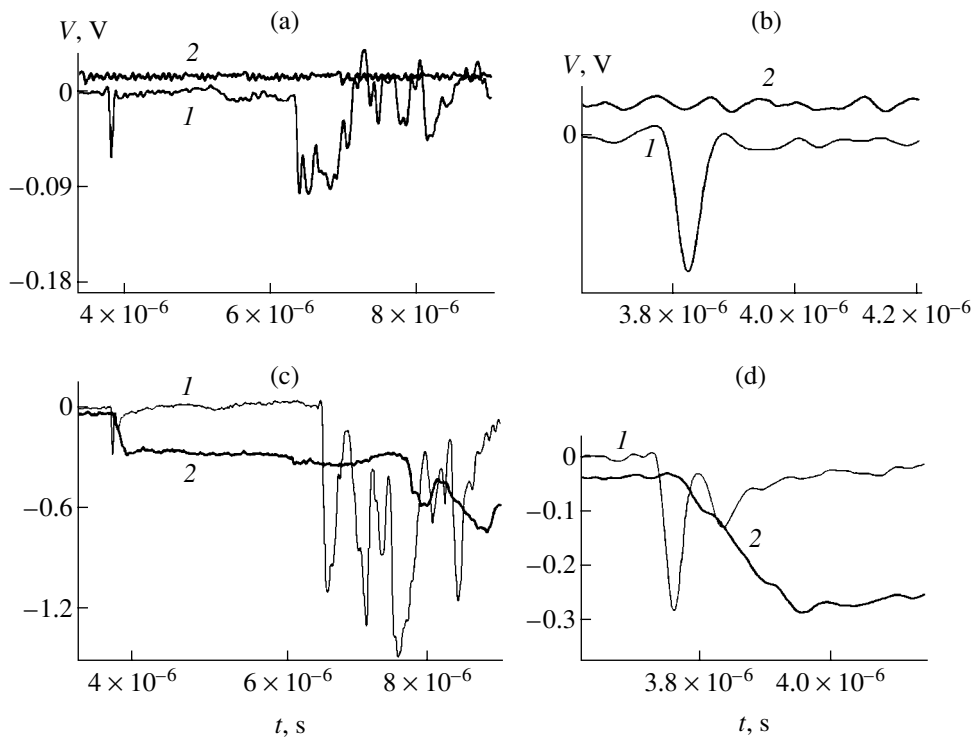
Fig. 1. Typical oscillograms of the output signals from photodetectors of (*1*) the interferometer and (*2*) the reflected light monitor in cases when the loading impact (a, b) did not or (c, d) did induce fracture near the free surface of a K8 glass sample.

corresponding to the crack formation. The delay of this signal relative to the loading pulse in the case of fracture by the cleavage mechanism must be equal to $t_1 = h/c_1$. Indeed, the experimentally measured values of $t_s = 65$ ns and $t_1 = 31$ ns lead to virtually coinciding calculated values of $h_s = 0.191$ mm and $h_1 = 0.186$ mm. The cleavage mechanism is also confirmed by the results of fractographic investigations.

Upon the sample cracking, the fracture develops in the cleavage zone. The oscillograms reflect development of the fracture (see the feature at $t = 6.2$ ms in curve *2* of Figs. 1c and 1d) and the corresponding free surface motion ($t = 6.32$ ms, curve *1*) related to the unloading waves coming from the cylinder side surface to the cleavage zone. The most intense formation of new fracture surfaces is observed at $t = 7.72$ μs (curve *2*), which corresponds to the arrival of the Rayleigh waves from the side surface to the cleavage zone.

Figure 2 shows micrographs illustrating the typical patterns of fracture near the free surface of the samples studied. The general pattern (Fig. 2a) corresponds to the cleavage followed by fracture of the cleavage zone, resembling a characteristic fracture observed in thin pates tested for symmetric bending. Figure 2b shows a fractogram of the surface of a cleavage crack formed parallel to the free surface at a depth of ≅0.19 mm. The cleavage shows a smooth surface with a band structure at the periphery. The smooth surface of the crack (Fig. 2c) contains defects in the form of pores with a size of ≤1 μm and a density of 8×10^6 cm^{-2}. These are
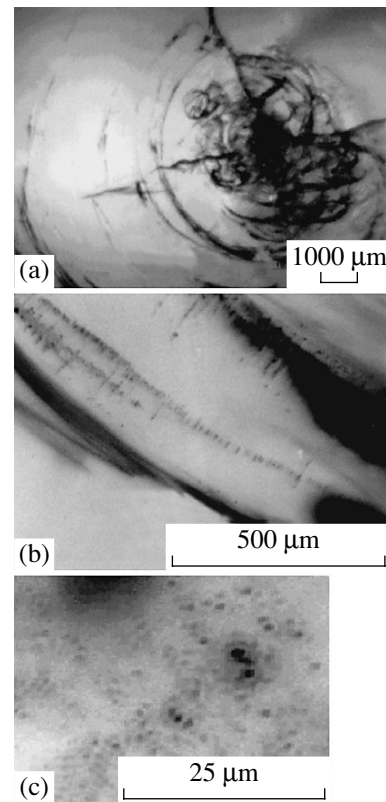
Fig. 2. Fractograms of the fracture region in a K8 glass sample cleaved by submicrosecond impact loading: (a) general pattern; (b, c) fragments of the cleavage crack surface (0.19 mm below the free surface).

probably traces of air bubbles frequently present in the glass.

Note that the fractograms display no microcracking in the form of "rosettes," which are usually observed for a multisite mechanism of cleavage nucleation in organic glasses and alkali-halide crystals [5–7]. This fact is either evidence of the absence of damage accumulation during the dynamic fracture of brittle materials (such as the inorganic glass studied) or indicates that the spatial scale of microdamage accumulation is smaller than the optical microscopy resolution level (≤0.1 μm). Thus, the results of our investigation reliably indicate that the onset of fracture in the K8 glass under submicrosecond loading proceeds by the cleavage mechanism at a critical cleavage stress of 0.45 ± 0.03 GPa.

The obtained experimental data do not allow us to unambiguously determine the character of the brittle fracture development process proceeding by the cleavage mechanism in inorganic glasses: at present, we cannot judge between a multistage process with damage accumulation and a catastrophic event. It is also necessary to explain the rather low value of the critical cleavage stress. The obtained estimate (0.45 GPa), while being five times greater than the ultimate strength of the K8 glass (0.09 GPa) [2], is still about one-third of the value reported in [3] and only one-tenth of the estimates obtained in [4]. This fact is not perfectly consis-tent with the existing notions concerning the character of the dynamic branch in the kinetic strength model.

REFERENCES

1. V. P. Pukh, in *Glass Strength and Fracture* (Leningrad, 1973), p. 155.

2. A. V. Ivanov, in *Strength of Optical Materials* (Leningrad, 1989), p. 144.

3. G. V. Stepanov, in *Elastic and Plastic Deformation and Fracture of Materials under Pulsed Loading* (Kiev, 1991), p. 288.

4. G. I. Kanel', S. V. Razorenov, A. V. Utkin, and V. E. Fortov, in *Impact–Wave Phenomena in Condensed Media* (Yanus-K, Moscow, 1996), p. 407.

5. Yu. V. Sud'enkov and É. V. Ivanov, in *Strength and Fracture of Materials and Constructions* (St. Petersburg State Univ., St. Petersburg, 1999), Vol. 18, pp. 220–227.

6. N. A. Zlatin, G. S. Pugachev, É. N. Belendir, *et al.*, Zh. Tekh. Fiz. **55** (9), 1780 (1985) [Sov. Phys. Tech. Phys. **30**, 1041 (1985)].

7. V. I. Blinov, G. I. Gering, and N. A. Eliseev, Zh. Tekh. Fiz. **56** (11), 2228 (1986) [Sov. Phys. Tech. Phys. **31**, 1333 (1986)].

Translated by P. Pozdeev

Stationary Regimes of the Turbulent Plasma Acceleration in a High-Current Magnetoplasmadynamic Thruster

K. P. Kirdyashev* and V. I. Brukhty

*Fryazino Branch, Institute of Radio Engineering and Electronics, Russian Academy of Sciences,
Fryazino, Moscow oblast, Russia*
* e-mail: kpk114@ire216.msk.su
Received December 25, 2000

Abstract—A reliable relationship is established between the electric propulsion parameters of a high-current magnetoplasmadynamic thruster and the intensity of both microwave radiation and low-frequency oscillations in the system. It is shown that realization of the stationary regimes of the turbulent plasma acceleration is limited by the excitation of a large-scale ion-sound turbulence in the plasma flow. © 2001 MAIK "Nauka/Interperiodica".

The prospects of using magnetoplasmadynamic (MPD) thrusters in space vehicles depend on solving the tasks of creating high-speed plasma sources and attaining the limiting plasma acceleration regimes. It was established [1–3] that operation in the limiting regimes is complicated by the development of instabilities leading to the excitation of various oscillations in the region of plasma acceleration and in the exhaust plasma flow. These oscillatory processes are accompanied by the turbulent heating of the anodic plasma and its acceleration as a result of the electron-ion friction during the excitation of microwave oscillations [4].

Under stationary operation conditions in an MPD thruster with external magnetic field, the effect of plasma acceleration by the turbulent mechanism is restricted to an anomalous heat evolution on the anode and is most pronounced in the limiting regimes of the thruster operation. The turbulent effects occurring in pulsed plasma thrusters allow the formation of an accelerating current layer of the plasma to be considered as the "electrothermal explosion" featuring a significant increase in the electron (T_e) and ion temperature (T_i) accompanying the current instability development in the plasma [5–6]. We have studied the conditions limiting the plasma acceleration by the turbulent mechanism in stationary regimes of a high-current MPD thruster and established a relationship between the thruster efficiency, the intensity of microwave radiation, and the spectrum of oscillations in the plasma flow.

The experiments were performed using experimental models of a high-current MPD thruster with various anode configurations. The variable thruster operation parameters included discharge voltage and current and the working substance (lithium) consumption. The experimental setup was tested under operation in a stationary discharge regime for the following parameters: discharge voltage, 25–60 V; discharge current 2000–4500 A; working substance consumption, 0.05–0.1 g/s. Under these conditions, the electron density in the cen-

tral region of the exhaust plasma flow measured with special probes was $(1–5) \times 10^{12}$ cm^{-3} at an electron temperature within 2–5 eV. The limiting operation regimes were realized in a high-voltage region of the current–voltage characteristics of the discharge, with a significant level of current carried outside the anode edge of the thruster. In these regimes, the electric discharge was characterized by the formation of an external accelerating plasma region, in which the electron density varied from 3×10^{11} to 10^{12} cm^{-3}.

In the limiting operation regimes, a significant part of the applied voltage drops across the external discharge region, where the beam instability development gives rise to the Langmuir oscillations detected by the electromagnetic radiation emitted from plasma in a 1–10 GHz frequency range. Using data on the electron temperature measured by the probe technique, we have determined intensity of the thermal radiation component. By experimentally detecting the intensity of microwave fields exceeding the thermal level, we determined the regions of the Langmuir oscillations in various parts of the discharge current–voltage characteristics. Oscillations in the frequency range from 20 to 500 kHz related to instability of the ion dynamics in the exhaust plasma flow were detected by the electric probes placed both at various angles in the plasma flow cross section near the anode and at various distances along the anode. Using these probes, it was possible to measure the spectra and determine the spatial structure of oscillations corresponding to various regions of the discharge current–voltage characteristics. Simultaneously with monitoring the electromagnetic radiation, we have performed direct measurements of the engine thrust and, using data on the working substance consumption, determined values of the truster efficiency and the lithium ion velocity in the plasma flow as described in [4].

The results of these investigations showed that discharge current–voltage characteristics can be separated into regions featuring different behavior of the electric
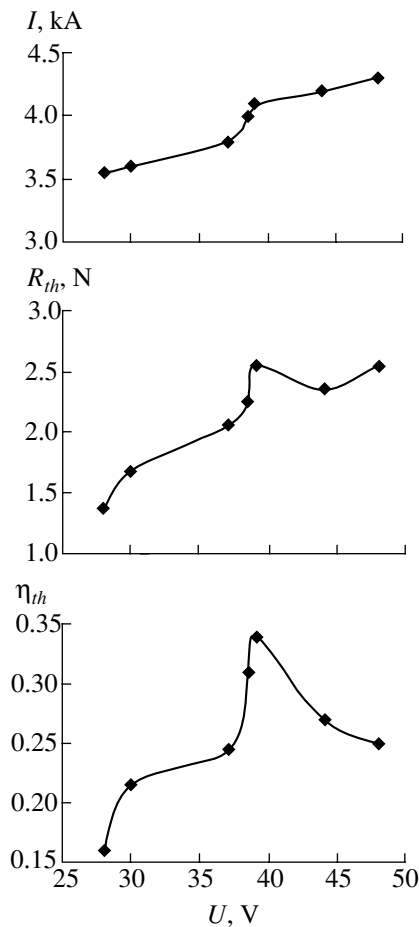
Fig. 1. The plots of electroreactive parameters versus discharge voltage illustrating the MPD thruster operation in various regions of the current–voltage characteristic.

propulsion parameters (discharge current, plasma flow thrust, and thruster efficiency) as functions of the applied voltage (Fig. 1). These regions correspond to the following intervals of the discharge voltage: 25–35 V (I), 35–40 V (II), and 40–60 V (III). Region I corresponds to the regime of weakly turbulent plasma flow generating a spectrum of low-frequency oscillations monotonically decreasing in intensity in the frequency range up to 300–400 kHz (Figs. 2a and 2b). The character of the thrust R_{th} variation agrees with the known relationship between this parameter and the discharge current I_0: $R_{th}(I_0) = k_{th}I_0^2$, where $k_{th} = (3.5–4) \times 10^{-3}$ N/A^2 is the thrust coefficient. The average ion velocity in the plasma flow is ~10^4 m/s at a thruster efficiency of $\eta_{th} = 0.2–0.25$. In the low-voltage region of the characteristic, the microwave radiation intensity J is maximum at a frequency of 3 GHz and varies from 10^{-9} to 10^{-8} W/(m^2 MHz) (Fig. 2c). These values are only slightly above the equilibrium level of the emission intensity estimated at 6×10^{-10}–10^{-9} W/(m^2 MHz) for a 3–5 eV electron temperature in the exhaust plasma flow. The degree of the Langmuir turbulence in the dis-

charge, determined by the volume density of microwave energy $W_{Pe}/(n_e T_e)$ with an allowance for the possible values of the energy conversion from plasma to electromagnetic waves, varies from 10^{-4} to 10^{-3}.

An increase in the discharge voltage to 35–40 V (region II in the current–voltage characteristic) leads to transition to a regime of intensive microwave emission, which corresponds to the Langmuir turbulence in the accelerating plasma region and which is accompanied by a significant increase in the thruster efficiency (up to $\eta_{th} = 0.35–0.4$). The accompanying increase in the discharge current is explained by the double ionization of lithium atoms.This is reflected by a change in the spectrum of optical emission from the plasma flow, showing a spectral line at 548.47 nm corresponding to the $2s^3S$–$2p^3P^0$ transition in excited lithium ion (with the upper and lower energy levels at 61.28 and 59.02 eV, respectively). The accompanying intense microwave emission suggests that the optical emission spectrum of the high-current discharge contains components related to the electron-impact excitation of lithium ions accelerated in microwave fields during the Langmuir turbulence development in the plasma [1].

An increase in the thruster efficiency correlated with the intensity of microwave oscillations is a manifestation of the turbulent plasma acceleration mechanism known in MPD thrusters with external magnetic field [4]. However, in a high-current thruster under consideration, this mechanism is operative only in a limited interval of the discharge voltage variation. As the applied voltage exceeds 45 V (region III in the current–voltage characteristic, showing limitation of the discharge current growth), the thruster efficiency exhibits a significant drop and does not exceed $\eta_{th} = 0.25$, despite a considerable growth in intensity of the microwave oscillations.

The results of measurements of the potential variation in the exhaust plasma flow (Fig. 2d) showed that it is the generation of low-frequency electromagnetic oscillations which is responsible for the drop in the thruster efficiency. It is important to note that this effect is related to the excitation of discrete modes in the oscillation spectra, corresponding to harmonics of the 120–140 kHz frequency component. The discrete components excited in the high-voltage discharge regimes correspond to large-scale perturbations of the plasma potential in the discharge volume. This is confirmed by the experimental facts such as considerable anode voltage jumps (above the voltage of the power supply unit) and correlated potential variations for the probes arranged in the cross section and in length of the exhaust flow. These conditions favor manifestations of a nonstationary discharge with characteristic breakdowns of the acceleration regimes and density pulsations of the exhaust plasma flow, which account for a decrease in the thruster efficiency.
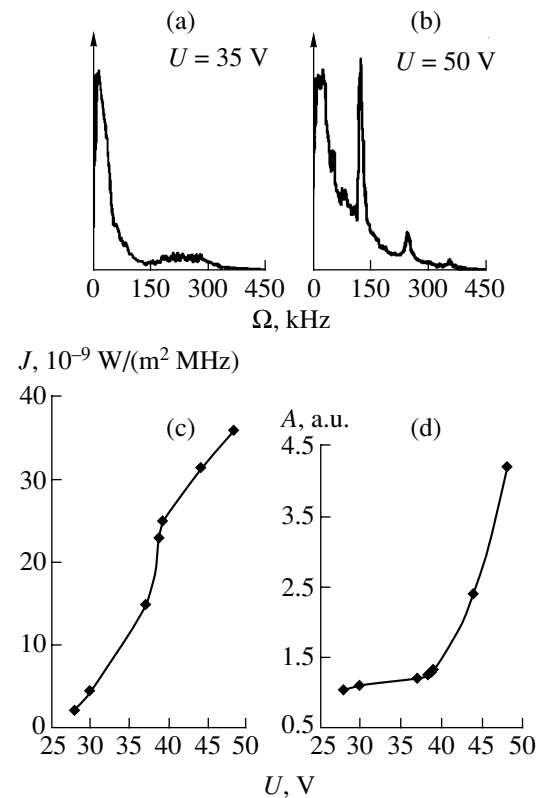
Let us consider the possible mechanisms for excitation of the large-scale components of the low-frequency oscillations restricting the thruster efficiency in the lim-

iting operation regimes. The first is the current instability of a plasma in the discharge region, which leads to excitation of the ion-sound oscillations if the electron and ion temperatures in the plasma are such that $T_e \gg T_i$. The low-frequency oscillation spectrum is consistent with the frequency representation in the form of $\Omega = k_m v_S$ for the discrete oscillation modes with $k_m = m/L$, where $v_S = (T_e/m_i)^{1/2}$ is the ion sound velocity and L is the size of the inner discharge region. Indeed, the ion velocity for the given experimental plasma parameters is $v_S = (3–5) \times 10^3$ m/s; for $L \sim 0.1$ m, the discrete oscillation modes of the discharge plasma potential correspond to the frequency harmonics observed in experiment. Note that the influence of large-scale oscillation modes on the efficiency of acceleration regimes is most pronounced for the high-current thrusters characterized by a greater size of the discharge region as compared to that in the engines of other types. This is suggested by the spectral function of the ion-sound turbulence in a plasma with the electron current [7], which can be represented in the form of $S(k) \sim \sqrt{\ln(1/kr_D)}/k^3$ when the energy of oscillations is concentrated in n the region of low frequencies near the lower boundary of stability.

Another possible reason for a discharge to switch into the regime of developed low-frequency turbulence is the fast ion beam instability in the accelerating region of the plasma flow. For the fast ion concentration $n_{i1} \ll n_{i0}$, where n_{i0} is the concentration of slow ions formed due to the ionization collisions, the instability increment $\gamma_i \sim \omega_{Pi}(n_{i1}/n_{i0})^{1/3}$ amounts to $\sim 10^5$. This allows excitation of the low-frequency oscillations to be considered within the time intervals corresponding to the ion flight time in the accelerating plasma region.

For the intense microwave oscillations excited in the high-voltage region of the current–voltage characteristic, we have to estimate the efficiency of a nonlinear process related to the decay-type instability of the Langmuir oscillations, whereby the energy is converted into that of the ion-sound waves. A nonlinear decrement of the Langmuir oscillations can be taken in the form of $\gamma_l = (1/2)k_l v_{Te}(\Omega/\omega_{Pe})^{1/2}(e\varphi_k/T_e)$ [7], where the potential oscillation amplitude in the Langmuir wave φ_k can be estimated from a maximum energy density of the microwave field in the plasma, which was measured to be $\sim 10^{-8}$ J/(m³ MHz). Under these conditions, the decrement of the Langmuir oscillations does not exceed $10–10^2$, which is very small as compared to the ion-sound wave frequency and allows the nonlinear process to be ignored.

Thus, the principal mechanisms responsible for the excitation of large-scale low-frequency oscillation modes, limiting realization of the turbulent plasma acceleration regimes in high-current MPD thrusters, include the current instability in the discharge plasma region and the instability of a beam of fast ions formed in the plasma flow. These instabilities are most pro-

nounced in the limiting operation regimes and are unavoidably developed during the stationary plasma acceleration in high-current MPD thrusters.

Fig. 2. Electromagnetic oscillations accompanying the MPD thruster operation: (a, b) the spectra of low-frequency oscillations at various discharge voltages; (c, d) the plots of microwave radiation intensity J and low-frequency oscillation amplitude A versus discharge voltage U.

REFERENCES

1. K. P. Kirdyashev, in *High-Frequency Wave Processes in Plasmadynamic Systems* (Énergoatomizdat, Moscow, 1982), p. 142.
2. N. N. Glotova, K. P. Kirdyashev, E. V. Naumov, *et al.*, Pis'ma Zh. Tekh. Fiz. **1** (10), 474 (1975) [Sov. Tech. Phys. Lett. **1**, 218 (1975)].
3. N. N. Glotova, K. P. Kirdyashev, I. N. Ostretsov, and A. A. Porotnikov, Zh. Tekh. Fiz. **46** (3), 506 (1976) [Sov. Phys. Tech. Phys. **21**, 288 (1976)].
4. V. I. Brukhty and K. P. Kirdyashev, Pis'ma Zh. Tekh. Fiz. **26** (14), 42 (2000) [Tech. Phys. Lett. **26**, 612 (2000)].
5. V. I. Aref'ev, Zh. Tekh. Fiz. **46** (4), 674 (1976) [Sov. Phys. Tech. Phys. **21**, 393 (1976)].
6. A. A. Kalmykov, in *Physics and Application of Plasma Accelerations*, Ed. by A. I. Morozov (Nauka i Tekhnika, Minsk, 1974), pp. 48–77.
7. B. B. Kadomtsev, in *Reviews of Plasma Physics*, Ed. by M. A. Leontovich (Atomizdat, Moscow, 1964; Consultants Bureau, New York, 1968), Vol. 4.

Translated by P. Pozdeev

Surface Resistance of Type II Superconductors: The Surface Barrier Effect

N. V. Zhelezina and G. M. Maksimova*

Nizhni Novgorod State University, Nizhni Novgorod, Russia
* e-mail: maksimova@phys.unn.runnet.ru
Received November 16, 2000

Abstract—The surface impedance of a type II superconductor plate occurring in the mixed state was calculated. In the case when a constant external magnetic field is perpendicular to the plate surface, the real part of the impedance (considered as a function of the magnetic field strength) exhibits a maximum, which is a manifestation of the dimensional effect. Behavior of the maximum was followed depending on the plate thickness and the alternating field frequency. On the passage to a planar geometry, an allowance for the Bean–Livingston barrier explains the formation of vortex-free regions near the plate surface, which leads to a decrease in the surface resistance and suppression of the size effect. © 2001 MAIK "Nauka/Interperiodica".

The surface impedance is one of the most important characteristics of superconductors, which allows the electrodynamic response of materials occurring in the mixed state to be studied. Coffey and Clem [1–3] studied a linear response of the type II superconductor in an alternating magnetic field with an allowance for the nonlocal vortex interaction, pinning, and magnetic flux creep effects. Fisher *et al.* [4] formulated a nonlocal model of the critical state describing the behavior of a hard superconductor with dimensions on the order of the London length λ in an alternating magnetic field. Sonin and Traito [5] showed that the Bean–Livingston barrier controlling the process of vortex entrance (or exit) leads to a considerable decrease in the dissipative losses in the case of samples with smooth edges.

We have studied the behavior of the surface resistance of a superconducting plate of finite thickness exposed to a magnetic field with a weak alternating component and differently oriented (perpendicular or parallel) constant component with an allowance for the Bean–Livingston (BL) surface barrier. In cases when the BL barrier hinders the vortex penetration through the sample surface and the number of vortices in the plate is constant, the surface resistance markedly decreases and the type of its dependence on the constant magnetic field strength changes.

Transverse geometry. Let us consider a superconducting plate of thickness d ($0 \leq x \leq d$) free of bulk pinning occurring in a constant magnetic field H_0 oriented perpendicularly to the sample surface, which creates a vortex lattice with a density of $n_0 = H_0/\Phi_0$, where Φ_0 is the magnetic flux quantum. An alternating magnetic field with a small amplitude and frequency ω is parallel to the plate surface. A system of equations describing the

magnetic field in the sample $\mathbf{h}(x, t) = \mathbf{h}(x)\exp(-i\omega t)$ is as follows:

$$\mathbf{h} - \lambda^2 \frac{\partial^2 \mathbf{h}}{\partial x^2} = H_0 \frac{\partial \mathbf{u}}{\partial x}, \tag{1}$$

$$\eta \frac{\partial \mathbf{u}}{\partial t} = \frac{1}{c}[\mathbf{j}\mathbf{\Phi}_0] + \frac{\Phi_0}{H_0} C_{44}^* \frac{\partial^2 \mathbf{u}}{\partial x^2}, \tag{2}$$

$$\mathbf{j} = \frac{c}{4\pi}\text{rot}\mathbf{h}, \tag{3}$$

where $\mathbf{u}(x, t) = \mathbf{u}(x)\exp(-i\omega t)$ is the vortex line displacement vector; $\eta = \Phi_0 H_{c2}/c^2 \rho_n$ is the viscosity coefficient; c is the speed of light; ρ_n is the resistivity in the normal state; and C_{44}^* is the local bending modulus of the vortex lattice [6],

$$C_{44}^* = \frac{\Phi_0 H_0}{16\pi^2 \lambda^2} \ln \frac{a}{\xi}, \tag{4}$$

a being the vortex spacing and ξ the vortex core radius.

Seeking for the solutions to Eqs. (1)–(3) in the form $u(x, t) \propto h(x, t) \propto \exp(kx - i\omega t)$ leads to a dispersion equation for $k = k(\omega)$. In the frequency range $\omega \ll \omega_c$, the solutions to this equation corresponding to the long-wave (k_1) and shortwave (k_2) modes are given by the formulas

$$k_1^2 = -\frac{i\omega}{\lambda^2(\omega_c + \omega_b)}, \quad k_2^2 = \frac{1}{\lambda^2}\left(1 + \frac{\omega_b}{\omega_c}\right), \tag{5}$$

where

$$\omega_c = \frac{\Phi_0 C_{44}^*}{H_0 \lambda^2 \eta}, \quad \omega_b = \frac{\Phi_0 H_0}{4\pi\lambda^2\eta}. \tag{6}$$

It should be note that a model of the two-mode electrodynamics for a type II superconductor in the mixed state was originally formulated by Sonin *et al.* [6].

Upon solving Eqs. (1)–(3) with an allowance for relationships (4)–(6), we obtain the following expression the surface impedance of the superconducting plate in the transverse magnetic field:

$$Z = \frac{4\pi}{c}\frac{E(0)}{h(0)}, \tag{7}$$

where $E(0)$ is the electric field on the plate surface. If the surface pinning is absent and the vortex ends can move freely over the plate surface, Eq. (7) can be rewritten as

$$Z = \frac{4\pi i\omega}{\lambda^2 c^2}\Bigg(\frac{(1-\lambda^2 k_2^2)}{k_1}\tanh\frac{k_1 d}{2}$$
$$-\frac{(1-\lambda^2 k_1^2)}{k_2}\tanh\frac{k_2 d}{2}\Bigg)(k_2^2 - k_1^2)^{-1}. \tag{8}$$

For sufficiently thick plates ($d \geq k_1^{-1}$), this yields

$$Z = -\frac{4\pi i\omega}{c^2 k_1}\mu\tanh\frac{k_1 d}{2}, \tag{9}$$

where $\mu = \omega_b/(\omega_c + \omega_b)$. According to formula (9), the quantity $\mathrm{Re}Z = \rho_s(H_0, \omega)$ is a nonmonotonic function of H_0, reaching a maximum at $H_0 = H_0^*$ where the characteristic field penetration depth is on the order of the sample thickness $k_1^{-1}(H_0^*) \propto d$. This size effect is analogous to the Fisher–Kao effect in normal metals [7] and is well known in hard superconductors (see, e.g., [4]).

A maximum value of the surface resistance $R = \rho_{s_{max}}/\chi_n$ (where $\chi_n = 2\pi\omega d/c^2$ is the surface reactance in the normal state) depends on the relative plate thickness d/λ and on the field frequency. As d/λ increases, R tends to a constant level independent of the superconductor parameters and the field frequency (Fig. 1). Note that an analogous behavior of R follows from a nonlocal model of the critical state for hard superconductors [4], but the R value predicted by this theory is lower by approximately half than the value obtained above.

Parallel geometry. In the case when a constant magnetic field is oriented parallel to the plate, the interaction of vortices with the sample surface gives rise to the LB barrier preventing the vortices from entering (or leaving) the superconductor. For a certain magnetic field value H_0, the vortices occupy a central region of the plate ($d/2 - a \leq x \leq d/2 + a$), with the width $2a$
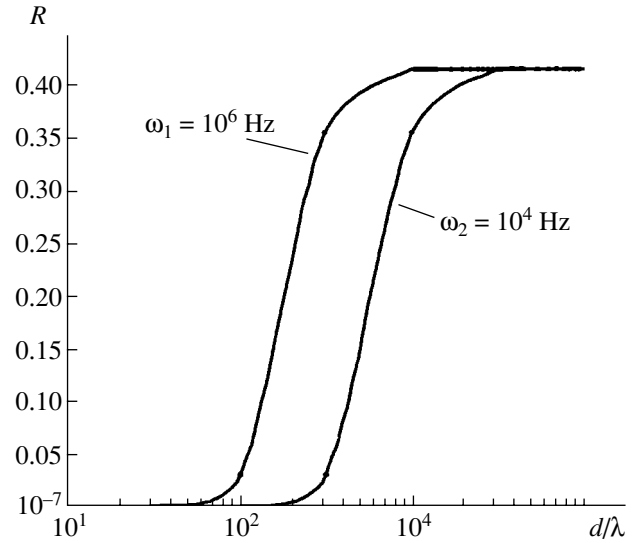
Fig. 1. The plots of maximum surface resistance $R = \rho_{s_{max}}/\chi_n (\chi_n = 2\pi\omega d/c^2)$ versus superconducting plate thickness for two frequencies of the alternating magnetic field.
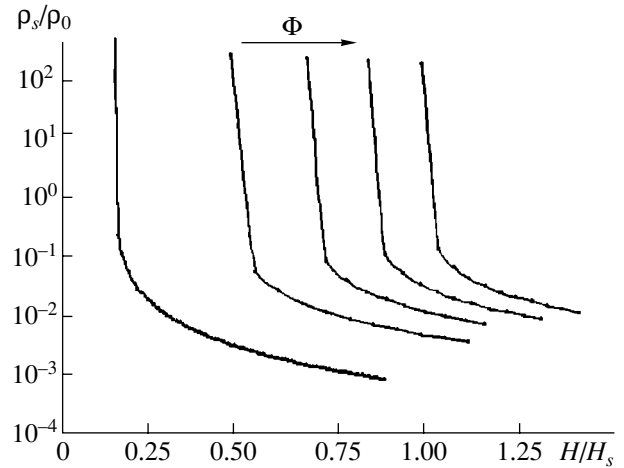
Fig. 2. The plots of surface resistivity of a superconducting plate versus strength of a parallel magnetic field, calculated with an allowance for the Bean–Livingston barrier for various values of the trapped magnetic flux $\Phi(\rho_0 = 4\pi\omega_0\lambda/c^2$, $\omega_0 = 1$ Hz). The arrow indicates the direction of changes corresponding to increase in the magnetic flux.

depending on H_0 and the trapped magnetic flux Φ:

$$\Phi = \frac{2aH_0}{\cosh(d/2 - a)/\lambda}. \tag{10}$$

For a given flux Φ, the magnetic field in formula (10) may vary within $H_{ex} \leq H_0 \leq H_{en}$, where H_{ex} and H_{en} are the field values corresponding to vanishing of the barrier for the vortex exit and entrance, respectively. Thus, vortex-free regions featuring the Meissner currents form at the plate surface. Application of a weak parallel alternating magnetic field leads to oscillations of the

vortex region with the persistent magnetic flux Φ. Upon solving the electrodynamic problem in this case, we obtain the following expression for the surface impedance:

$$Z = -\frac{4\pi i \omega \lambda}{c^2} \frac{\alpha \tanh\frac{a}{\alpha} + \lambda \tanh b}{\lambda + \alpha \tanh\frac{a}{\alpha} \tanh b}, \quad (11)$$

where $b = (d/2 - a)/\lambda$ is the relative width of the vortex-free regions, $\alpha = \lambda(1 + il^2/\lambda^2/\cosh b)^{1/2}$, and $l = (\Phi_0 H_0/4\pi\eta\omega)^{1/2}$. As seen from formula (11), the surface impedance for $b = 0$ (no vortex-free regions) and dense vortex lattice ($\mu \approx 1$) coincides with that predicted by formula (9) for the transverse geometry. This situation probably arises in the case when the plate surface is rough and the BL barrier is suppressed.

In the case when the region occupied by the vortices is spaced from the plate surface ($b \neq 0$), the calculations reveal two important consequences. The first is a significant decrease in the surface resistance: the presence of a narrow vortex-free region ($\lambda/l \ll b < 1$) decreases the viscous losses by a factor of $(bl/\lambda^2)^2$. For a typical high-temperature superconductor with $\lambda \approx 1300$ Å and $H_{c2} = \Phi_0/(2\pi\xi^2) \propto 300$ T, we obtain for $H_0 \propto 0.01 H_{c2}$ and $\omega \propto 10^6$ Hz that $(bl/\lambda^2)^2 \propto 10^3$. The second feature is that the surface resistance $\rho_s(H_0)$ becomes a decreasing function of the constant magnetic field H_0 in the whole interval $H_{ex} \leq H_0 \leq H_{en}$ corresponding to the persistent magnetic flux (Fig. 2). Thus, the presence of the vortex-free regions at the plate surface ($b \neq 0$) leads to the disappearance of the maximum of $\rho_s(H_0)$, that is, to the suppression of the size effect.

REFERENCES

1. M. W. Coffey and J. R. Clem, Phys. Rev. Lett. **67**, 386 (1991).

2. J. R. Clem and M. W. Coffey, Phys. Rev. B **46**, 14 662 (1992).

3. M. W. Coffey and J. R. Clem, Phys. Rev. B **46**, 11 757 (1992).

4. L. M. Fisher *et al.*, Physica C (Amsterdam) **245**, 231 (1995).

5. E. B. Sonin and K. B. Traito, Phys. Rev. B **50**, 13 547 (1994).

6. E. B. Sonin, A. K. Tagantsev, and K. B. Traito, Phys. Rev. B **46**, 5830 (1992).

7. H. Fischer and Y.-H. Kao, Solid State Commun. **7**, 275 (1969).

Translated by P. Pozdeev

Stochastic Synchronization and the Growth in Regularity of the Noise-Induced Oscillations

D. É. Postnov, D. V. Setsinskiĭ, and O. V. Sosnovtseva*

Saratov State University, Saratov, Russia
* e-mail: olga@chaos.ssu.runnet.ru
Received December 14, 2000

Abstract—The results of electronic experiments show for the first time that synchronization of the excitable stochastic systems enhances the coherent resonance effect, which is manifested by the regularization of a collective response of the system. © *2001 MAIK "Nauka/Interperiodica"*.

Recent investigations convincingly demonstrated that the noise in nonlinear systems may play a constructive role, increasing the degree of order. The most illustrative examples are offered by the results of the investigations in the field of stochastic resonance reported in hundreds of papers (see [1] and references therein). As is known, a noise acting upon a nonlinear system may induce oscillations in this system [2, 3].

A new wave of interest in such problems was inspired by the discovery of the coherent resonance effect, which is manifested by the existence of an optimum interval of the noise intensity in which the noise-induced oscillations exhibit a maximum regularity; that is, they are most close to the periodic oscillations [4, 5]. Two mechanisms were suggested to explain this effect. According to the first model, the noise "reveals" an oscillatory dynamics inherent in a deterministic system; this approach is close to that used in the problem of noise precursors of bifurcations [6, 7]. Another mechanism is based on the balance of two characteristic times, one of which (activation tome) is controlled by the noise intensity and the other (relaxation time) is determined by the system parameters [8]. As was theoretically predicted in [8] and experimentally confirmed in [9, 10], this mechanism predicts the coherent resonance effect even in systems not possessing oscillating solutions in the deterministic case. This fact demonstrates the principal difference (despite an apparent similarity) between the stochastic oscillations under the coherent resonance conditions and the deterministic self-sustained oscillations in the presence of noise, making the study of the former process independently important.

Previously, we demonstrated that the noise-induced oscillations in two coupled excitable systems may exhibit a lock-in effect with respect to both the middle frequency locking and the overall effective synchronization (time-restricted phase locking [13]). These results stimulated extensive investigations into the coherent properties of excitable media [11, 12]. One of

the central questions in this problem is connected to regularity of the collective response of an ensemble of excitable systems.

Below, we report on the results of electronic experiments revealing a relationship between the effect of stochastic synchronization of two coupled excitable systems and the possibility of attaining a maximum regularity in the noise-induced oscillations.

The excitable system studied represented a threshold electronic device (monovibrator) producing an output pulse of certain duration in response to the input signal exceeding a definite threshold level (Fig. 1a). For an input noise signal with the intensity D, the average time of activation (i.e., of reaching the excitation threshold) is proportional to $e^{\lambda/D}$ (where λ is the parameter determined by the barrier height and the system properties) according to the Arrhenius law [14], whereas the generated pulse duration is determined by parameters of the electronic scheme and weakly depends on the noise intensity (provided that the threshold voltage is small as compared to the pulse amplitude). The experimental radiophysical method consisted in varying the level of external noise entering the system (representing either single or coupled monovibrators) and processing the output signal to determine the its power spectrum and other characteristics.

As was demonstrated previously [9], the adopted radiophysical model of the excitable system exhibits the coherent resonance effect. This is confirmed by a difference in the power spectra of oscillations served for various D values (Fig. 1b). In order to quantitatively characterize this effect, various researchers described the inhomogeneity of the spectrum by different methods, including calculation of the signal-to-noise ratio [4, 6] or the autocorrelation function [8]. We selected a more universal method for characterization of the regularity of oscillations using their spectrum. Our approach is based on the formula for entropy $E =$

(a)
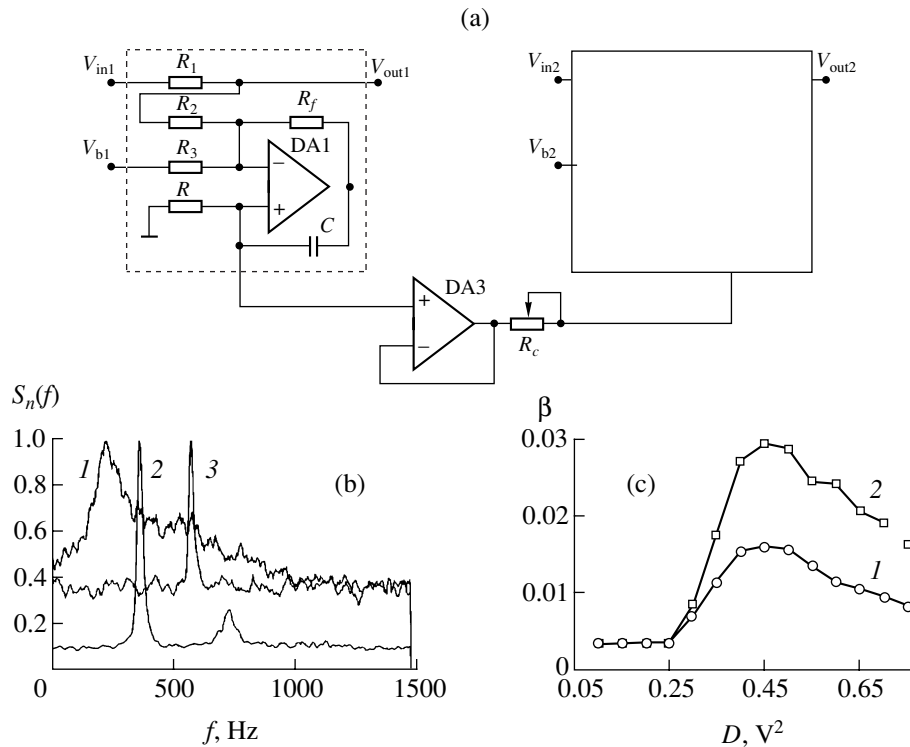
Fig. 1. (a) A schematic electronic circuit diagram of the monovibrator and a scheme of two coupled subsystems (the experimental setup employed the following system parameters: $R_1 = 2.2$ kΩ, $R_2 = R_3 = R = 10.0$ kΩ, $R_f = 100.0$ kΩ, $C = 33$ nF, $V_b = 2.6$ V, $E = \pm 15$ V); (b) power spectrum of the noise-induced oscillations for small ($D = 0.3$ V^2, curve *1*), optimum ($D = 0.45$ V^2, curve *2*), and large ($D = 1.5$ V^2, curve *3*) noise signal intensity; (c) the plots of regularity parameter for the first (curve *1*) and second (curve *2*) subsystems versus noise intensity D.

$-\sum_{i=1}^{i=n} s_n(\omega_i) \ln(s_n(\omega_i))$, where $s_n(\omega_i)$ is the normalized power spectrum containing n components. The regularity parameter is calculated as $\beta = 1 - E/E_{max}$, where E_{max} is the entropy of the homogeneous spectrum (white noise). Defined in this way, the β value reflects essentially the unevenness of the spectrum, varying from unity for the purely harmonic oscillations to zero for the white noise.

Calculations of the regularity parameter for a single monovibrator show the presence of a pronounced maximum in the plot of β versus the nose intensity D (Fig. 1c). At this point, the noise-induced oscillations are closest to being periodic.

The coherent properties of stochastic oscillations in a system of two unidirectionally coupled monovibrators were studied under the conditions of initially different properties of the subsystems: the maximum regularity of oscillations in the second subsystem was significantly greater than that in the first subsystem. According to the results of analysis for the single monovibrator, the noise intensity can be considered as a parameter controlling the frequency of induced oscillations. Thus, a change in D_2 at a fixed D_1 is equivalent to the variation of the frequency detuning of the two stochastic oscillators. It was found that the presence of

coupling between the two subsystems leads to a coincidence of their middle frequencies in a broad range of D_2 (Fig. 2a). This effect is analogous to the synchronization of deterministic oscillations as a result of the frequency locking. The calculations of β showed that the collective response of both systems exhibits a greater regularity as compared to that observed in the autonomous regime (cf. curves *2* and *3* in Fig. 2b).

Figures 2c and 2d present the results of measurements of the ratio of frequencies of the noise-induced oscillations in comparison to the regularity values plotted versus the coupling parameter $g = R/R_c$. As is seen, the values of β in the first subsystem remain on the same level because the system regime is independent of g (curve *1*). The scatter of these points characterizes the real accuracy of measurements attained for the given parameters of data digitizing and averaging used in calculations of the signal characteristics. As is seen, the measurement errors are significantly smaller than the changes in the β values for the second subsystem, which exhibit a sharp increase on attaining the synchronization region (curve *2*). The attained level of regularity ($\beta \approx 0.045$) exceeds the optimum value observed for the same subsystem studied in the regime of a single excitable monovibrator by approximately 50% (curve *3*).
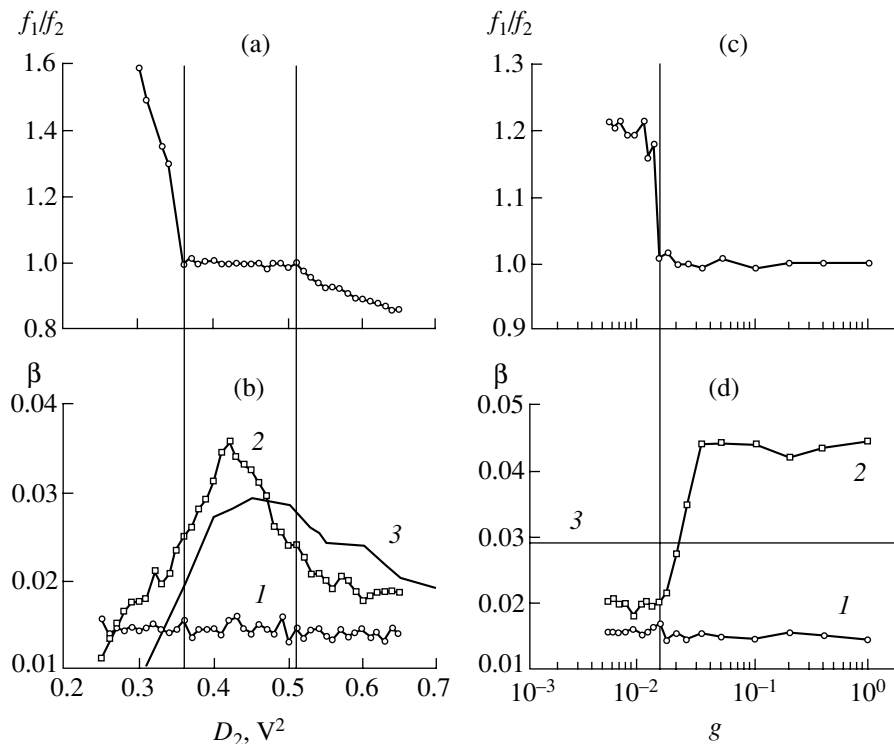
Fig. 2. The coherent resonance and stochastic synchronization effects in a system of two unidirectionally coupled monovibrators with $D_1 = 0.45$ V^2 illustrated by plots of (a, c) the interval of frequency locking of the stochastic oscillations and (b, d) the corresponding regularity parameter versus (a, b) noise intensity D_2 (for $g = 0.02$) and (c, d) coupling parameter g (for $D_2 = 0.36$ V^2). Curves *1* show regularity variations in the first subsystem for unidirectional coupling (independent of D_2 and g); curves *2* show a significant growth in regularity of the second subsystem on reaching the region of synchronization; curves *3* show (b) the regularity level for the second subsystem in the absence of coupling and (d) a maximum regularity level for the second subsystem operating in the autonomous regime.

On a qualitative level, the above results can be explained as follows. In the case of the unidirectional coupling, the second subsystem can be considered as a single monovibrator under the action of a complex noise signal representing a superposition of the Gaussian white nose (with the intensity D_2) and the output signal of the first subsystem (with the intensity gU, where U is the rms signal intensity at the first subsystem output and g is the coupling coefficient). Assuming that the character of response of an excitable system is determined primarily by the total intensity of the acting noise signal ($D_s = D_2 + gU$), we may conclude that the variation of the parameter g shifts the working point of the second subsystem relative to the optimum value D_2 (corresponding to the maximum regularity). Here, the initial regime of the second subsystem becomes an important factor. Should D_2 be set behind the optimum point, an increase in g moves the second subsystem away from the maximum regularity level. If the D_2 value is below optimum, an increase in g increases the synchronization effect and shifts the working point of the second subsystem toward optimum. When the two factors—the stochastic synchronization regime and the optimum noise intensity $D_s =$ $D_2 + gU$—combine, it is possible to obtain the output signal of a still higher degree of regularity.

Thus, the results of the model radiophysical experiment showed that, under certain conditions, the degree of regularity of the synchronous response of coupled excitable systems to the external noise action may significantly exceed the maximum value attainable for a single system. A similar result was obtained in the case of mutually coupled systems. These experimental results, as well as the hypothesis explaining this behavior, may be useful in the study of stochastic dynamics in an ensemble of excitable systems.

REFERENCES

1. V. S. Anishchenko, A. B. Neĭman, F. Moss, and L. Schimansky-Geier, Usp. Fiz. Nauk **169** (1), 7 (1999).
2. W. Horsthemke and R. Lefever, *Noise Induced Transitions: Theory and Applications in Physics, Chemistry and Biology* (Springer-Verlag, Heidelberg, 1984; Mir, Moscow, 1987).

3. P. S. Landa and A. A. Zaikin, Zh. Éksp. Teor. Fiz. **111**, 358 (1997) [JETP **84**, 197 (1997)].

4. H. Treutlein and K. Schulten, Ber. Bunsenges. Phys. Chem. **89**, 710 (1985).

5. W.-J. Rappel and S. H. Strogatz, Phys. Rev. E **50**, 3249 (1994).

6. A. Neiman, P. Saparin, and L. Stone, Phys. Rev. E **56**, 270 (1997).

7. S.-G. Lee, A. Neiman, and S. Kim, Phys. Rev. E **57**, 3292 (1998).

8. A. Pikovsky and J. Kurths, Phys. Rev. Lett. **78**, 775 (1997).

9. D. E. Postnov, S. K. Han, T. G. Yim, and O. V. Sosnovtseva, Phys. Rev. E **59**, R3791 (1999).

10. S. K. Han, T. G. Yim, D. E. Postnov, and O. V. Sosnovtseva, Phys. Rev. Lett. **83**, 1771 (1999).

11. A. Neiman, L. Schimansky-Geier, A. Cornell-Bell, and F. Moss, Phys. Rev. Lett. **83**, 4896 (1999).

12. B. Hu and C. Zhou, Phys. Rev. E **61**, R1001 (2000).

13. A. N. Malakhov, *Fluctuations in Auto-Oscillation Systems* (Nauka, Moscow, 1968).

14. H. A. Kramers, Physica (Amsterdam) **7**, 284 (1940).

Translated by P. Pozdeev

Specific Properties
of the PZT-Based Thin-Film Capacitor Structures
with Excess Lead Oxide

V. P. Afanas'ev, G. N. Mosina, A. A. Petrov, I. P. Pronin*,
L. M. Sorokin, and E. A. Tarakanov

Ioffe Physicotechnical Institute, Russian Academy of Sciences, St. Petersburg, 194021 Russia;
St. Petersburg State Electrotechnical University, St. Petersburg, Russia
* e-mail: pronin@inprof.ioffe.rssi.ru
Received February 1, 2001

Abstract—The effect of excess lead oxide on the microstructure and ferroelectric properties of lead zirconate titanate (PZT) films was studied in PZT-based thin-film capacitor structures. It is shown that excess lead in the form of lead oxide is localized at the grain boundaries and film–platinum electrode interfaces, which can result in the appearance of internal electric fields and the self-polarization of PZT films. It is suggested that the self-polarization effect is related to the formation of a built-in electric charge with different densities at the bottom and top metal electrode–ferroelectric film interfaces. © *2001 MAIK "Nauka/Interperiodica".*

Thin ferroelectric films of lead-containing oxides with a perovskite structure serve as base elements in modern micromechanical, pyroelectric, and some other transducers [1]. An important task in the fabrication of such films, related to a high volatility of lead oxide (PbO), consists in obtaining a single-phase perovskite structure (free of an amorphous and/or pyrochlore phase with a crystallization temperature below that of the perovskite phase) [2–4]. When the films are manufactured by the method of RF magnetron sputtering, the most widely employed means of obtaining single-phase deposits is to use ceramic or composite targets containing excess PbO [5–6]. By the same token, when the films are manufactured by chemical methods (sol–gel, CVD, MOD, etc.), a component containing excess lead is introduced into the initial solutions. However, the task of monitoring the concentration and distribution of excess lead oxide still remains important. On the other hand, the character of the influence of excess PbO on the ferroelectric properties of thin films has not been studied in sufficient detail [7, 8].

In connection with this, the purpose of our study was to determine the effect of excess lead on the microstructure and properties of thin ferroelectric films of lead zirconate titanate $PbZr_xTi_{1-x}O_3$ (PZT).

We have studied PZT films with a thickness of up to 1 μm prepared by the RF magnetron sputtering of ceramic targets as described in [9]. The targets corresponded to the PZT compositions with $x = 0.54$ or 0.40 containing excess (10 mol %) PbO; we also studied the stoichiometric compositions with $x = 0.54$. The films were deposited onto silicon substrates with a bottom platinum electrode and an adhesive titanium sublayer;

the substrate temperature during deposition was 130°C. The amorphous deposits were converted into a perovskite phase by thermal treatment for 1 h in air at 550°C.

The crystal structure of the films was determined by X-ray diffraction (DRON-2 diffractometer, Russia) and transmission electron microscopy (JEM-7A electron microscope, Japan). The elemental depth–composition profiles were studied by Auger electron spectroscopy (EKO-3 spectrometer, Russia). A relationship between the target composition and the physical properties of PZT films was studied by measuring the dielectric hysteresis loops and capacitance–voltage (C–V) characteristics of the thin-film capacitor structures with platinum electrodes. The depth–polarization profiles were determined by measuring the frequency-dependent pyroelectric current using the laser intensity modulation method (LIMM) [10].

The PZT films deposited at a relatively low substrate temperature had compositions close to that of a sputtered target [9]. Taking into account that the subsequent thermal treatment was also effected at a relatively low temperature (550°C), it was expected that the final film composition must coincide with that of the initial targets. The X-ray diffraction measurements on the PZT films studied showed that all samples had a polycrystalline perovskite structure without pyrochlore phase admixtures, with the grains oriented predominantly in the [111] direction.

Figure 1 shows typical electron micrographs of the PZT films and the corresponding electron microdiffraction patterns. A film obtained by the sputtering of a stoichiometric target with $x = 0.54$ (Fig. 1a) possesses (after the thermal treatment) a grain size of 50–80 nm
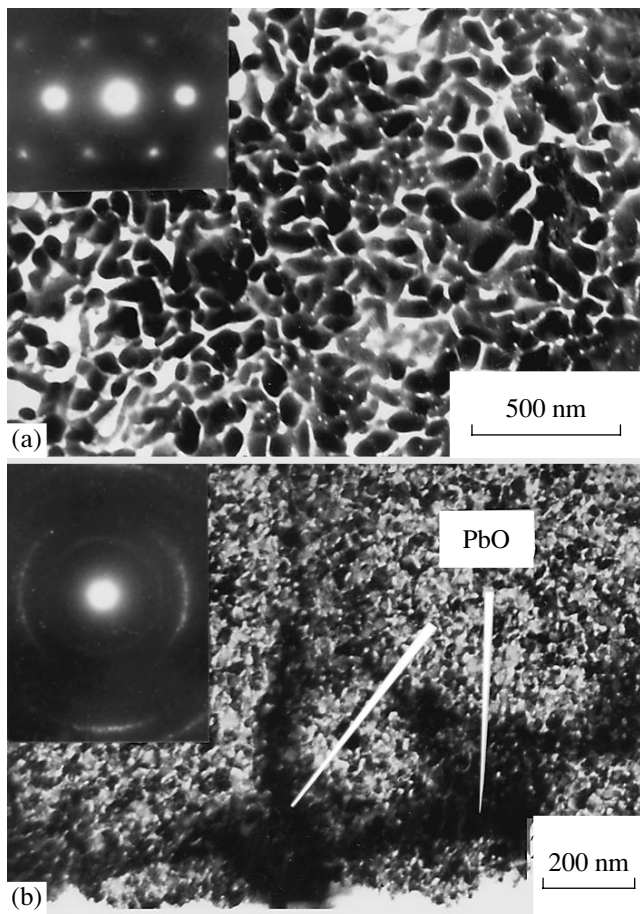
Fig. 1. Transmission electron micrographs of PZT films deposited onto substrates by sputtering targets with (a) stoichiometric ($PbZr_{0.54}Ti_{0.46}O_3$) and (b) nonstoichiometric ($PbZr_{0.4}Ti_{0.6}O_3$ + 10 mol % PbO) compositions. The insets show the corresponding electron diffraction patterns.
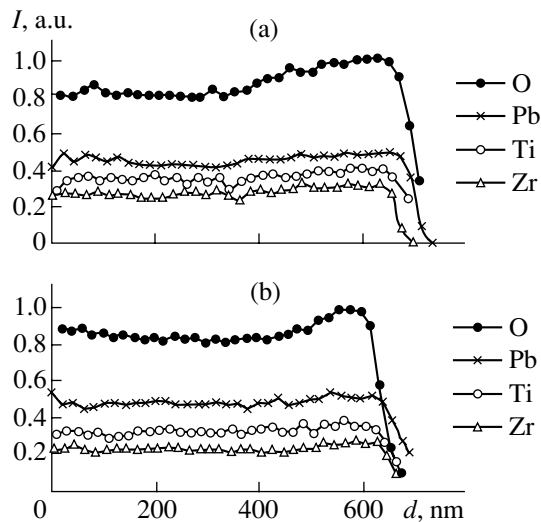
Fig. 2. Elemental depth–composition profiles of PZT films obtained by sputtering targets with (a) stoichiometric ($PbZr_{0.54}Ti_{0.46}O_3$) and (b) PbO-rich ($PbZr_{0.54}Ti_{0.46}O_3$ + 10 mol % PbO) compositions.

in the film plane and exhibits an electron diffraction pattern characteristic of the monoblock [111]-oriented single-crystal films. The electron diffraction patterns of the samples obtained using PbO-rich targets exhibit a combination of arcs and separate spots, which is evidence of a textured polycrystalline film. A comparison of the results of our X-ray diffraction and electron microdiffraction measurements to the published data [11] suggests that all the films studied possess a columnar crystallite structure extending over the entire film thickness.

The films obtained by sputtering targets with excess lead exhibit a smaller grain size (Fig. 1b) as compared to that in the stoichiometric films. The micrographs reveal equiaxial inclusions present at the grain boundaries and in the subsurface film regions, which we attribute to the PbO phase precipitation; for example, a film obtained by sputtering a target with $x = 0.40 +$ 10 mol % PbO is characterized by a grain size of 20–30 nm in the film plane. The patterns of electron diffraction from some areas of such films represented diffuse rings (halos) corresponding to an amorphous or ultradisperse PbO phase. This is additional evidence of an inhomogeneous structure of the PZT films formed upon the thermal treatment of amorphous deposits possessing nonstoichiometric compositions.

We may suggest that the formation of a perovskite phase as a result of the thermal treatment at 550°C is accompanied by segregation of the excess lead not only at the grain boundaries and the film surface but at the film–bottom electrode interface as well. This is confirmed by the elemental depth–composition profiles of the PZT films (Fig. 2) studied by the Auger electron spectroscopy. As is seen from Fig. 2a, the films obtained by sputtering of a stoichiometric target ($x = 0.54$) are characterized by a homogeneous lead concentration profile, which falls to zero at the bottom interface, in agreement with the drop in Zr and Ti concentrations. At the same time, the films obtained by sputtering PbO-rich targets (e.g., with $x = 0.54 +$ 10 mol % PbO) exhibit an increase in the relative lead content on both the free film surface and at the film–bottom electrode interface (Fig. 2b).

Thus, the films containing excess lead are characterized by the formation of PbO-rich intermediate layers at the interfaces with bottom and top electrodes. The presence of these layers must be taking into account in interpreting some distinctions in behavior of the PZT-based thin-film capacitor structures obtained using stoichiometric and nonstoichiometric targets. These features are manifested in the dielectric hysteresis loops (Fig. 3) and C–V characteristics of the films [12].

A characteristic feature of the dielectric hysteresis loops and C–V curves of the capacitor structures based on PbO-rich PZT films is the pronounced asymmetry with respect to the sign of the applied electric field, which is related to the formation of a built-in charge at the film–electrode interfaces. Indeed, the dielectric

Polarization, μC/cm²

Electric field, kV/cm
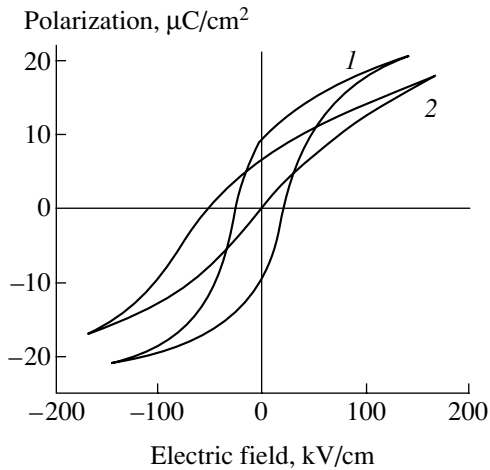
Fig. 3. Dielectric hysteresis loops of PZT films obtained by sputtering targets with (*1*) stoichiometric (PbZr$_{0.54}$Ti$_{0.46}$O$_3$) and (*2*) PbO-rich (PbZr$_{0.54}$Ti$_{0.46}$O$_3$ + 10 mol % PbO) compositions.

$P(x/d)$, a.u.
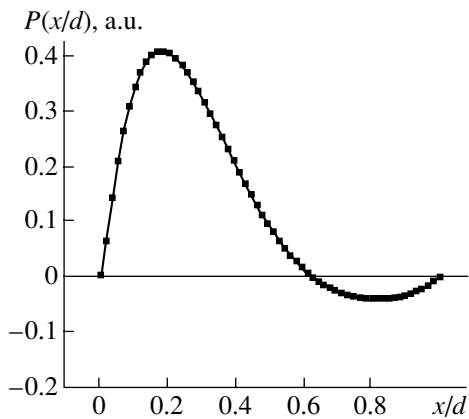
Fig. 4. Depth–polarization profiles $P(x/d)$ of a PZT film obtained by sputtering a PbO-rich (PbZr$_{0.54}$Ti$_{0.46}$O$_3$ + 10 mol % PbO) target.

hysteresis loop of a PZT film obtained by sputtering a stoichiometric target is symmetric (see Fig. 3, curve *1*), whereas the loop of film obtained from a PbO-rich target is evidently asymmetric (Fig. 3, curve *2*). This is explained by the appearance of a built-in field in the film, which is generated by a predominant negative surface charge formed at the film–bottom electrode interface, probably due to the oxygen vacancies in PZT and PbO segregated at this interface. In turn, the presence of PbO inclusions may be one of the factors determining the appearance of oxygen vacancies. The magnitude of a built-in electric field in PZT films of a micron thickness may exceed 30–40 kV/cm, as estimated from the shift of the dielectric hysteresis loops and *C–V* curves.

As noted above (see Figs. 1 and 2b), the PbO phase may be present at the film interfaces with both (bottom and top) electrodes. However, conditions for the formation of these interfaces are significantly different for the

bottom and upper electrodes. Indeed, the thermal treatment leading to crystallization of the perovskite phase in PZT films is carried out when only the bottom electrode is present. Therefore, we may naturally expect that the bottom electrode–film interface is characterized by a greater density of charged surface states than the upper interface.

The built-in charges may lead to the self-polarization of a PZT film and even to the formation of near-electrode regions polarized in the opposite directions, as is seen in the depth-polarization profiles (Fig. 4). A comparative analysis of the whole body of data for the films obtained by sputtering stoichiometric and nonstoichiometric (PbO-rich) targets suggests that the excess lead oxide plays a key role in the built-in electric field formation.

Thus, we have established that excess lead present in thin-film PZT-based capacitor structures tends to segregate in the form of lead oxide at the grain boundaries and interfaces with bottom and top electrodes. It is suggested that the presence of lead oxide results in the formation of oxygen vacancies responsible for charging of the near-electrode PZT regions. This may lead to the self-polarization of the films and even to the formation of near-electrode regions polarized in the opposite directions.

REFERENCES

1. D. L. Polla, Microelectron. Eng. **29**, 51 (1995).
2. Zhan-jie Wang, Ryutaro Maeda, and Kaoru Kikuchi, Jpn. J. Appl. Phys., Part 1 **38** (9B), 5342 (1999).
3. M. Klee, A. de Veirman, D. J. Taylor, *et al.*, Integr. Ferroelectr. **4**, 197 (1994).
4. C. K. Kwok, S. B. Desu, and D. P. Vijay, Ferroelectr. Lett. Sect. **16**, 143 (1993).
5. S. B. Krupanidhi, Integr. Ferroelectr. **1**, 161 (1992).
6. K. Sreenivas and M. Sayer, J. Appl. Phys. **64**, 1484 (1988).
7. Zh. Song, W. Ren, L. Zhang, and Ch. Lin, Thin Solid Films **353**, 25 (1999).
8. K. Yamakawa, O. Arisumi, K. Okuwada, *et al.*, in *Proceedings of the 11th IEEE International Symposium on Applications of Ferroelectrics, Montreux, Switzerland, 1998*, p. 159.
9. V. P. Afanas'ev, S. V. Bogachev, N. V. Zaĭtseva, *et al.*, Zh. Tekh. Fiz. **66** (6), 160 (1996) [Tech. Phys. **41**, 607 (1996)].
10. S. B. Lang, Ferroelectrics **106**, 1105 (1990).
11. R. E. Jones, Solid State Technol., No. 10, 201 (1997).
12. V. P. Afanasjev, A. A. Petrov, I. P. Pronin, *et al.*, J. Phys.: Condens. Matter (2001) (in press).

Translated by P. Pozdeev

Generation of High-Intensity Second Harmonics by Femtosecond Pulses

T. M. Lysak and V. A. Trofimov

Moscow State University, Moscow, 119899 Russia
Received January 29, 2001

Abstract—It is demonstrated that high-intensity second harmonic generation by femtosecond pulses is possible under conditions of the wave self-action during propagation in an optical fiber. © *2001 MAIK "Nauka/Interperiodica".*

The second harmonic generation (SHG) by femtosecond pulses is a fundamental problem in the nonlinear optics [1]. To the present, this SHG process could not be performed with a high efficiency. Moreover, the time of attaining a conversion level of 90% markedly increases when the light pulse duration decreases to a few picoseconds [1], thus deviating from a linear relationship valid for the input pulses with a length exceeding several picoseconds. Apparently, this circumstance is related to the manifestation of a cubic nonlinearity (wave self-action), which is most pronounced for the femtosecond pulses [2–4].

The results of the computer simulation [5] and subsequent analysis of the interaction waves within the framework of the long-pulse approximation [6, 7] showed that the SHG efficiency for femtosecond pulses is determined by the ratio of dimensionless parameters characterizing the quadratic and cubic nonlinearities and the input wave intensity. An important result was obtained in [7], where we demonstrated the possibility of two stable SHG regimes with different efficiencies in the presence of phase detuning of the interacting waves. It should be noted that physical experiments are conducted under the initial conditions corresponding to the SHG regime of low ($\theta < 20\%$) efficiency. Below, we will demonstrate that a high-efficiency SHG process can be realized as well [8].

Assuming that the diffraction length is considerably greater than the characteristic length of a nonlinear medium (e.g., for the waves in optical fibers), a system of equations in dimensionless variables describing the process of SHG by a femtosecond pulse with an allowance of the light wave self-action is as follows [2]:

$$\frac{\partial A_1}{\partial z} + iD_1\frac{\partial^2 A_1}{\partial \eta^2} + i\gamma A_1^* A_2 e^{-i\Delta kz} + i\alpha_1 A_1(|A_1|^2 + 2|A_2|^2) = 0, \quad 0 < z \le L_z,$$

$$\frac{\partial A_2}{\partial z} + \nu\frac{\partial A_2}{\partial \eta} + iD_2\frac{\partial^2 A_2}{\partial \eta^2} + i\gamma A_1^2 e^{i\Delta kz} + i\alpha_2 A_2(2|A_1|^2 + |A_2|^2) = 0, \quad \alpha_2 = 2\alpha_1 = 2\alpha.$$

$$(1)$$

Here, η is the dimensionless time in the frame of reference moving with the main-frequency wave pulse; z is the normalized longitudinal coordinate; $D_j \sim -0.5\dfrac{\partial^2 \bar{k}_j}{\partial \bar{\omega}_j^2}$ are the coefficients characterizing the second-order dispersion of the jth wave; $\bar{k}_j$ and $\bar{\omega}_j$ are the dimensional wavenumber and frequency of the jth wave, respectively; γ is the nonlinear coupling coefficient of the interacting waves; $\Delta k = k_2 - 2k_1$ is the dimensionless detuning of the wavenumbers; α_j are the wave self-action coefficients; A_j are the complex amplitudes of the harmonics ($j = 1, 2$) normalized to the maximum amplitude of the first harmonic in the initial cross section of the medium ($z = 0$); ν is a parameter proportional to the difference of the reciprocal group velocities of the second- and first-harmonic waves; and L_z is the length of the nonlinear medium.

In the input cross section, the initial pulse of the main frequency is described by the Gaussian or hyper-Gaussian distribution

$$A_1(z = 0, \eta) = A_1^0(\eta) = \exp(-(\eta/\tau)^m/2),$$
$$m = 2, 4\ldots, \quad 0 \le \eta \le L_t,$$

$$(2)$$

where L_t is the dimensionless time interval during which the process is analyzed. The second-harmonic wave amplitude in the initial cross section is zero: $A_2(z = 0, \eta) = 0$.

The SHG process under the wave self-action conditions is characterized by several invariants. Using these, we may integrate Eq. (1) within the framework of the long pulse approximation [7]. Figure 1 shows the domains corresponding to qualitatively different SHG regimes in the plane of parameters ($q = \gamma^2/\alpha^2$, $p = \Delta k/2\alpha$). Note that the parameter q characterizes the dominating nonlinearity (quadratic or cubic) during the SHG process. The quantity p characterizes the dominating phase shift of the interacting waves, indicating whether the wave self-action or the absence of phase locking is the main factor determining phase detuning of the second- and first-harmonic pulses. It should be emphasized that region 4 (Fig. 1), which is closest to the conditions of physical experiments with femtosecond pulses, features a bistable dependence of the SHG efficiency on the medium length. Taking this into account, we select the following SHG process parameters: $\alpha = 16$, $\gamma = 4$, $\Delta k = -2$, $D_1 = D_2 = 0.1$, and $\nu = 0$ (group synchronism). The initial pulse duration is set at $\tau = 1$.

The results obtained by solving the system of Eq. (2) are illustrated in Fig. 2, which shows intensity distributions of the main-frequency wave $J_1(z, 0) = |A_1(z, 0)|^2$ (solid curves) and the second-harmonic wave $J_2(z, 0) = |A_2(z, 0)|^2$ (dotted curves) at the pulse center. A sharp growth in intensity of the main wave (first peak) as a result of the self-focusing leads to a synchronous increase in the second-harmonic wave intensity. As the waves propagate in the medium, the intensity at the center of both harmonics exhibits a synchronous increase for both Gaussian ($m = 2$, Fig. 2a) and hyper-Gaussian ($m = 6$, Fig. 2b) pulses until reaching a certain cross section determined by the initial pulse shape, after which the two wave intensities vary in counter phase. This is followed by a new period of synchronous variation and so on.

In our opinion, this evolution of the wave intensities is explained by self-focusing in the central part of the pulse of either main-frequency of second-harmonic wave. By virtue of this, a sharp increase in intensity of either wave leads to the generation of another one. As a result, after traveling a certain distance in the medium, the intensity of the stronger wave becomes insufficient for self-focusing in the vicinity of the pulse center and the wave amplitude drops because of the pulse dispersion. Note that the dispersive blurring of the pulse center sharply increases since the compression involves only this part rather than the whole pulse. A decrease in the wave intensity leads to a drop in the new wave generation, the dispersion of waves simultaneously decreasing their intensities.

Figure 2b exhibits another interesting feature, whereby the intensity drops almost to zero at the main-frequency pulse center. This phenomenon is related to the effective SHG in this part of the pulse, since the wave self-action within this propagation interval is insignificant because of a nearly homogeneous shape of the initial pulse. As a result, the presence of a phase detuning in the vicinity of the $z = 0.25$ cross section
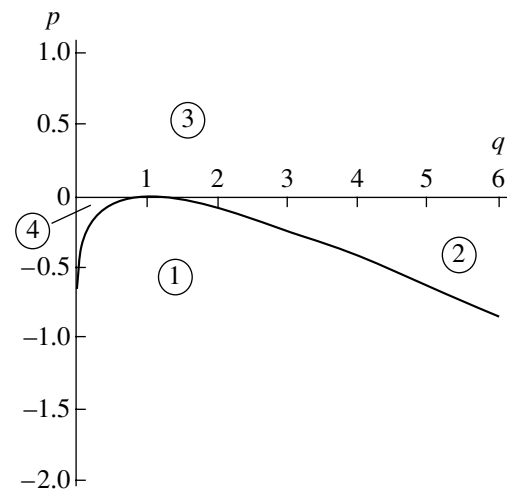
Fig. 1. Domains corresponding to the existence of qualitatively different SHG regimes in the plane of parameters ($q = \gamma^2/\alpha^2$, $p = \Delta k/2\alpha$). Regions 1–3 maintain a single stable generation regime. Regions 2 and 3 are featuring similar SHG regimes separated by the phase locking line. The laws governing the attainment of a minimum main-frequency pulse intensity in region 1 are different from those in regions 2 and 3. Region 4 features a bistable dependence of the SHG efficiency on the medium length: both stable states are realized.
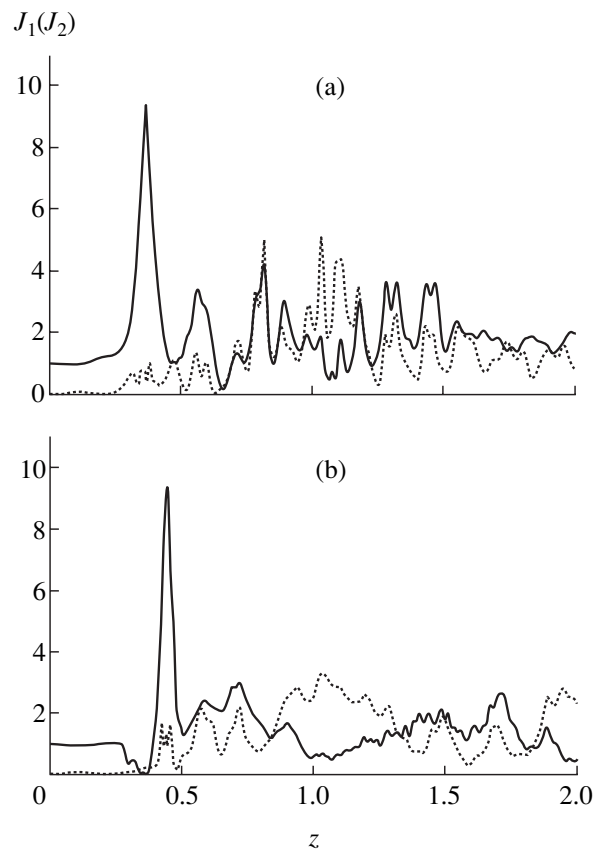
Fig. 2. Evolution of the main-frequency wave intensity J_1 (solid curves) and the second-harmonic wave J_2 (dotted curves) at the center of (a) Gaussian and (b) hyper-Gaussian pulses.
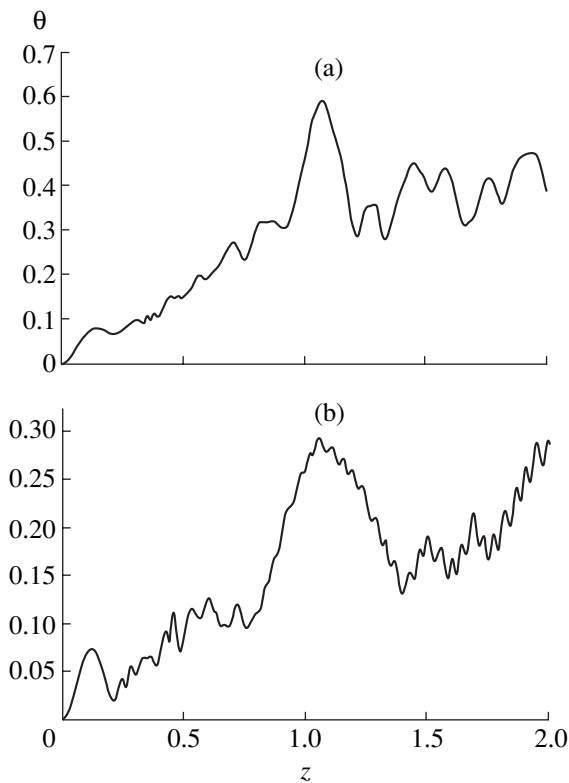
Fig. 3. Evolution of the SHG efficiency θ for (a) Gaussian and (b) hyper-Gaussian pulses.

provides conditions for the effective SHG at the pulse center. Since the pulse shape acquires a "dip" in intensity at the center (in fact, there are two subpulses of the main-frequency wave), this is followed by a growth in intensity (as is known, the tubular pulses transform into Gaussian ones) sufficient for the onset of compression in this part of the pulse. This results in a sharp growth of the peak intensity (manifested by the first peak in Fig. 2b).

To confirm that the wave self-action is the main factor responsible for the behavior described above, let us consider the evolution of the SHG efficiency for the Gaussian and hyper-Gaussian pulses. Apparently, the self-focusing effects will be less pronounced in the latter case because of a more homogeneous shape of the hyper-Gaussian pulse. As an example, Figure 3 shows the SHG efficiency described by a function θ of the longitudinal coordinate

$$\theta(z) = \int_0^{L_t} J_2(z, \eta)d\eta \Big/ \int_0^{L_t} J_1(0, \eta)d\eta,$$

$$J_1(0, \eta) = \left|A_1^0(\eta)\right|^2, \quad J_2(z, \eta) = \left|A_2(z, \eta)\right|^2.$$

In a comparison of the curves for the Gaussian and hyper-Gaussian pulses, the efficiency of energy conversion from first to second harmonic for the latter pulse is on average half that for the former one. All other conditions being the same, the reason for this evolution consists in the decreasing influence of the wave self-action.

The SHG efficiency increases on the whole with a length of the distance traveled in the medium. However, there are oscillations on this background which are related to a periodic breakage of the optimum phase relationship between the interacting waves caused by their self-action and the pulse dispersion. During the wave self-action and simultaneous (with respect to the coordinate z) growth in the intensity of both waves, each wave acquires a certain phase gain upon traveling a short distance. This phase gain is twice as large for the second-harmonic wave than for the main-frequency wave (because of the different dimensionless coefficients). Therefore, the phase relationship changes at a certain distance and the effective generation process starts again, this cycle being multiply repeated. Note that the phase relationship varies for different parts of the pulse on the passage from one cross section to another. It should be emphasized that this is accompanied by switching between low- and high-efficiency branches. This circumstance accounts for the total increase in the conversion efficiency.

In this study, we did not touch on the problem of modulation instability of the light waves. This factor may partly modify the pattern outlined above. In our opinion, the modulation instability may (i) increase the medium pathlength on which the effective SHG regime is attained and (ii) distort the pulse shape. More rigorous predictions would require an additional analysis that also resents an independent interest.

Translated by P. Pozdeev

REFERENCES

1. G. Steinmeyer, P. H. Sutter, L. Gallmann, *et al.*, Science **286**, 1507 (1999).

2. T. B. Razumikhina, L. S. Telegin, A. I. Kholodnykh, and A. S. Chirkin, Kvantovaya Élektron. (Moscow) **11** (10), 2026 (1984).

3. P. P. Ho, Q. Z. Wang, and R. R. Alfano, Opt. Lett. **16**, 970 (1991).

4. T. Ditmire, A. M. Rubenchik, D. Eimerl, and M. D. Perry, J. Opt. Soc. Am. B **13**, 649 (1996).

5. S. A. Krikunov, S. A. Magnitskii, and V. A. Trofimov, in *Abstract of the European Conference on Laser Interaction with Matter, ECLIM'98, Formia, 1998*, Th/P/9.

6. I. S. Ivanova, S. A. Magnitskiĭ, and V. A. Trofimov, Vestn. Mosk. Univ., Ser. Vychisl. Mat. Kibern., No. 1, 21 (2000).

7. T. M. Lysak and V. A. Trofimov, Zh. Vychisl. Mat. Mat. Fiz. (2001) (in press).

8. V. A. Trofimov and T. M. Lysak, in *Technical Program of International Conference "Laser Optics'2000," St. Petersburg, 2000*, p. 40.

Dynamics of the Transverse Oscillations of an Electron Beam in a Stellarator

V. V. Dolgopolov and Yu. V. Kirichenko

Kharkov Physicotechnical Institute, National Scientific Center, Kharkov, Ukraine
Received January 10, 2001

Abstract—The transverse oscillations of a thin electron beam in a stellarator or in a modified betatron were theoretically studied. The analysis is based on the relativistic Lorentz equation for intrinsic fields of the electron beam calculated by the method of retarded potential. Conditions for an instability development caused by the stellarator field inhomogeneity are determined. It is shown that a stellarator may also feature other instabilities of the transverse oscillations which are not related to the stellarator field inhomogeneity. © *2001 MAIK "Nauka/Interperiodica"*.

The instabilities caused by interactions of the transverse oscillations of electron beams and the intrinsic oscillations of a waveguide formed by the metal sheath and magnetic field in a stellarator were studied in [1, 2]. Within the framework of a hydrodynamic description, the transverse beam oscillations in a stellarator were described in [3]. We have studied the possibility of an instability development not related to the intrinsic waveguide oscillations.

Below, we will use an (x, y, θ) coordinate system, where x and y are the Cartesian coordinates in the plane perpendicular to the magnetic axis of the torus and θ is the angle measured in the magnetic axis direction (for detail, see [4]). Let us denote by $\tilde{f}$ a small deviation (perturbation) of a quantity f from the equilibrium value $\bar{f}$:

$$f = \bar{f} + \tilde{f}, \quad |\tilde{f}| \ll |\bar{f}|, \quad \frac{\partial \bar{f}}{\partial t} = 0, \quad \frac{\partial \bar{f}}{\partial \theta} = 0. \quad (1)$$

The electron velocity **u** can be presented in the form $\mathbf{u} = \bar{u}\,\mathbf{l}_\theta + \tilde{\mathbf{u}}$. Dependence of all perturbations on the time t and angle θ will be described by a factor $\exp[i(\mu\theta - \omega t)]$, where μ is an integer and ω is the frequency. In the case of transverse oscillations (of interest in the system studied), we may neglect perturbations in u_θ (the projection of **u** on the $\mathbf{e}_\theta$ direction) and N (the linear number density of electrons). Then, the initial differential equations represent two projections of the relativistic Lorentz equation onto the transverse coordinate axes x and y [4]. Entering into these equations are the fields of beam perturbation (**E**, **H**) and the external magnetic field $\mathbf{B} = \mathbf{B}_\theta + \mathbf{B}_{st} + \mathbf{B}_\beta$, where $\mathbf{B}_\theta$, $\mathbf{B}_{st}$, and $\mathbf{B}_\beta$ are the toroidal, two-thread stellarator, and betatron magnetic fields, respectively, determined by the formulas

$$\mathbf{B}_\theta = B_0 \frac{R_0}{R} \mathbf{e}_\theta, \quad \mathbf{B}_\beta = B_0 \beta \mathbf{e}_y,$$

$$\mathbf{B}_{st} = B_0 \frac{sm}{R_0} \quad (2)$$

$$\times [\mathbf{e}_x(x\sin m\theta + y\cos m\theta) + \mathbf{e}_y(x\cos m\theta - y\sin m\theta)],$$

where R_0 is the radius of magnetic axis of the torus, $R = R_0 - x$, and the other parameters obey the conditions $-\frac{1}{2} < s < 0$, $|\beta| \ll 1$, $B_0 > 0$. Previously [4], we calculated the fields **E**, **H** for a thin circular ring in the zero- and first-order approximations with respect to perturbations. Unfortunately, in that article the authors admitted a misprint in the formulas for $\tilde{E}_\theta$, $\tilde{H}_y$, which must read in the general case as follows:

$$\tilde{E}_\theta$$
$$= \frac{2e}{\bar{R}} \Lambda \left\{ \frac{\partial \tilde{N}}{\partial \theta} - \frac{\bar{N}}{2\bar{R}} \frac{\partial \tilde{x}}{\partial \theta} + \frac{\bar{u}}{c^2}\left(\hat{\tilde{N}}\bar{R} - \frac{1}{2}\bar{N}\hat{\tilde{x}} \right) + \frac{\bar{N}\bar{R}}{c^2} \hat{\tilde{u}}_\theta \right\}; \quad (3)$$

$$\tilde{H}_y = -\frac{e\bar{N}}{c\bar{R}} \Lambda \left\{ \tilde{u}_\theta + \bar{u}\left(\frac{\tilde{N}}{\bar{N}} + \frac{\tilde{X}}{\bar{R}} \right) + 2\frac{\partial \tilde{u}_x}{\partial \theta} - \frac{\bar{u}}{\bar{R}}\hat{\tilde{x}} \right\}, \quad (4)$$

where $\Lambda = \ln(\theta_m/\theta_\varepsilon)$, $\hat{f} = \partial^2 f/\partial\theta^2 - (\bar{R}^2/c^2)\partial^2 f/\partial t^2$, $-e < 0$ is the charge of electron, and the upper dot denotes derivatives with respect to time t.

In the zero-order approximation with respect to the perturbation, the equilibrium state of the electron beam is described by the following relationships:

$$\bar{x} = \bar{y} = 0, \quad u = \frac{\omega_0 \beta R_0}{2(1+\eta)} \pm \sqrt{\frac{\omega_0^2 \beta^2 R_0^2}{4(1+\eta)^2} - \frac{\eta c^2}{1+\eta}}, (5)$$

where $\omega_0 = eB_0/m_e c$, $m_e = m_{e_0}\gamma$, $\gamma = (1 - u^2/c^2)^{-1/2}$, $\eta = e^2 N\Lambda/m_e c^2$, and m_{e_0} is the electron mass. In Eq. (5) and below, the sign of the tilda is omitted for simplicity and

$\bar{u}$, $\bar{N}$ are written as u, N. Using the condition of positiveness in Eq. (5), we obtain conditions for the equilibrium velocity u corresponding to an equilibrium orbit.

Let us replace the coordinates $\tilde{x}$, $\tilde{y}$ by the variables $z_{\pm} = \tilde{x} \pm i\tilde{y}$. Using the Lorentz equation [4] in the first-order approximation with respect to the perturbation, we obtain for the new variables

$$L_{+}z_{+} = \frac{\omega_0 u}{R_0}\left(mse^{-im\theta} - \frac{\beta}{2}\right)z_{-};$$

$$L_{-}z_{-} = \frac{\omega_0 u}{R_0}\left(mse^{im\theta} - \frac{\beta}{2}\right)z_{+}, \tag{6}$$

where L_{+} and L_{-} are the operators defined by the formulas

$$L_{\pm} = (1 + 2\eta)\left(\frac{\partial}{\partial t} + \frac{u}{R_0}\frac{\partial}{\partial\theta}\right)^2 \mp i\omega_0\left(\frac{\partial}{\partial t} + \frac{u}{R_0}\frac{\partial}{\partial\theta}\right)$$
$$+ \frac{\eta c^2}{R_0^2\gamma^2}\left(\frac{\partial^2}{\partial\theta^2} - \frac{R_0^2}{c^2}\frac{\partial^2}{\partial t^2}\right) + \frac{\omega_0\beta u}{2R_0}. \tag{7}$$

The parameters of magnetic field in a stellarator always obey the condition $|ms| \gg |\beta|/2$ [5, 6], which implies that we may neglect the second term in the right-hand part of Eqs. (6). Then, the set of Eqs. (6) reduces to independent equations

$$L_{\mp}(e^{\pm im\theta}L_{\pm}z_{\pm}) = (\omega_0\omega_m s)^2 e^{\pm im\theta}z_{\pm}, \tag{8}$$

where $\omega_m = mu/R_0$. Taking into account the dependence on t, θ adopted in this study and using Eq. (8), we obtain the following fourth-order dispersion equation for $\omega_{\mu} = \omega - \mu u/R_0$:

$$\sum_{n=0}^{4} D_n\omega_{\mu}^{n} = 0, \tag{9}$$

where

$$D_0 = \left\{(1 + 2\eta)\omega_m^2 + \omega_0\omega_m\left(1 - \frac{\beta}{2m}\right)\right.$$
$$\left. + \frac{\eta c^2}{\gamma^2 R_0^2}\left[m(m \pm 2\mu) + \frac{\mu^2}{\gamma^2}\right]\right\}$$
$$\times \left\{\frac{\mu^2 c^2\eta}{\gamma^4 R_0^2} - \omega_0\omega_m\frac{\beta}{2m}\right\} - (\omega_0\omega_m s)^2;$$

$$D_1 = -\left\{\frac{2\mu u\eta}{\gamma^2 R_0} \pm 2(1 + 2\eta)\omega_m \pm \omega_0\right\}$$
$$\times \left\{\frac{\mu^2 c^2\eta}{\gamma^4 R_0^2} - \omega_0\omega_m\frac{\beta}{2m}\right\} - \left\{(1 + 2\eta)\omega_m^2 + \omega_0\omega_m\left(1 - \frac{\beta}{2m}\right)\right.$$
$$\left. + \frac{\eta c^2}{\gamma^2 R_0^2}\left[m(m \pm 2\mu) + \frac{\mu^2}{\gamma^2}\right]\right\}\left\{\frac{2\mu u\eta}{\gamma^2 R_0} \mp \omega_0\right\};$$

$$D_2 = \left(1 + 2\eta - \frac{\eta}{\gamma^2}\right)\left\{(1 + 2\eta)\omega_m^2 + \omega_0\omega_m\left(1 - \frac{\beta}{m}\right)\right.$$
$$\left. + \frac{\eta c^2}{\gamma^2 R_0^2}\left[m(m \pm 2\mu) + \frac{2\mu^2}{\gamma^2}\right]\right\}$$
$$+ \left\{\frac{2\mu u\eta}{\gamma^2 R_0} \pm 2(1 + 2\eta)\omega_m \pm \omega_0\right\}\left\{\frac{2\mu u\eta}{\gamma^2 R_0} \mp \omega_0\right\}; \tag{10}$$

$$D_3 = -2\left(1 + 2\eta - \frac{\eta}{\gamma^2}\right)\frac{u}{R_0}\left\{\frac{2\mu\eta}{\gamma^2} \pm (1 + 2\eta)m\right\};$$

$$D_4 = \left(1 + 2\eta - \frac{\eta}{\gamma^2}\right)^2.$$

The relativistic electron beams with currents amounting to a few tenths of a kA and the voltage of several meV obey the following relationships

$$\gamma^2 \gg 1, \quad \eta \ll 1/2, \quad |\omega_m/\omega_0| \ll 1, \quad 2\sqrt{\eta} \leq |\beta m|. \tag{11}$$

In what follows, we will also take into account that $s^2 + \beta/2m < 1/4$ [1, 2, 4]. An analysis of the roots of the dispersion equation (9) was performed in the range of $|m| \ll |\mu| \ll \frac{|m|\gamma^2}{2\eta}$ which (as demonstrated below) contains all the solutions of interest. Simplifying coefficients D_n with a allowance for the above assumptions and considering the conditions for real roots of Eq. (8), we obtain the following results. For the μ values satisfying the condition $|\mu| \geq \mu_{thr} = \gamma\sqrt{\omega_0/4\nu}$ ($\nu = eN\Lambda c/(R_0^2 B_0\gamma^2)$), the electron beam in a stellarator is unstable with respect to transverse oscillations independently of the magnetic field parameters (1). For $m\beta > 0$ and $|\mu| < \mu_{pore}$, the beam is stable with respect to the transverse oscillations under consideration. For

$m\beta < 0$; however, the transverse oscillations are unstable in the range

$$\frac{|mu|\,R_0\omega_0\gamma^4}{c^2\eta}\left[\frac{1}{2} - \sqrt{s^2 + \frac{\beta}{2m}}\right]$$

$$\leq \mu^2 \leq \frac{|mu|\,R_0\omega_0\gamma^4}{c^2\eta}\left[\frac{1}{2} + \sqrt{s^2 + \frac{\beta}{2m}}\right]. \qquad (12)$$

The center of this range is determined by the formula $\mu_0 = \gamma\sqrt{|\omega_m|/2\nu}$ ($\mu_0 < \mu_{\mathrm{thr}}$). Note that, in contrast to the results obtained in [1], the relative width of the range (12) is not small ($\Delta\mu/\mu_0 \sim 1$).

To study the transverse beam oscillations in a modified betatron, we have to put $s = 0$ in Eqs. (6). In this case, a dispersion equation s derived similarly to Eq. (9). An analysis of the equation for a modified betatron carried out under the same conditions as for the stellarator, showed that the transverse oscillations in this betatron are unstable only for $|\mu| \geq \mu_{\mathrm{thr}}$. This result, together with the fact that a width of the range (12) tends to zero as $s \longrightarrow 0$, indicates that the transverse instability of an electron beam in the stellarator for $m\beta < 0$ in the range (12) is due to longitudinal inhomogeneities of a magnetic field in the stellarator.

From the standpoint of the electron beam stability with respect to transverse oscillations in the stellarator, a magnetic system with $m\beta > 0$ should be preferred. However, these conditions would unavoidably lead to instability with respect to longwave oscillations [4], which is related to the negative mass instability. The transverse instability for $|\mu| \geq \mu_{\mathrm{thr}}$ is not related to the $\mathbf{B}_{st}$ field component. At large frequencies ω ($|\omega_\mu| \ll |\mu|c/(R_0\gamma^2)$) and $\mu \longrightarrow \infty$, the dispersion relationships (9) for stellarator and modified betatron coincide in the following form:

$$\left(\omega_\mu^2 + \frac{\mu^2 c^2 \eta}{R_0^2 \gamma^4}\right)^2 = 0. \qquad (13)$$

A solution to Eq. (13) yields a complex frequency of the transverse oscillations, which corresponds to the high-frequency instability arising at large $|\mu|$ values:

$$\omega = \mu c/R_0 \pm i\mu c\sqrt{\eta}/(R_0\gamma^2). \qquad (14)$$

It was also of interest to study the possibility of separating the circular beam oscillations into longitudinal and transverse components. Previously [4], we considered the general case of coupled transverse and longitudinal oscillations. Ignoring the transverse oscillations and considering large $|\omega|$ and $|\mu|$ values, we obtain the case when no longitudinal oscillations can exist in the circular beam. This is a consequence of the toroidal configuration, since a solution to the problem for the linear beam indicates that the independent longitudinal oscillations may exist at large $|\omega|$ and $|\mu|$. However, the coupling of high-frequency transverse and longitudinal oscillations with large $|\mu|$ in a circular beam vanishes as $\sqrt{\eta}/\gamma^2 \longrightarrow 0$. Under real conditions, the parameter $\sqrt{\eta}/\gamma^2$ has a very small value. This is an additional ground for ignoring the longitudinal perturbations in $\tilde{N}$, $\tilde{u}_\theta$ during the study of transverse oscillations of the electron beam in a stellarator.

In concluding, it should be noted that Eq. (13), as well as the dispersion equation describing oscillations of both transverse and longitudinal oscillations (as derived in [4]) for large $|\omega|$ and $|\mu|$ do not contain the parameters of an external magnetic field. Therefore, conclusions concerning the coupling of transverse and longitudinal oscillations in a circular electron beam are of a general character.

REFERENCES

1. T. P. Hughes and B. B. Godfrey, Phys. Fluids **29** (5), 1698 (1986).
2. Kang T. Tsang, Phys. Fluids B **2** (11), 2779 (1990).
3. N. D. Naumov, Zh. Tekh. Fiz. **67** (7), 103 (1997) [Tech. Phys. **42**, 814 (1997)].
4. V. V. Dolgopolov and Yu. V. Kirichenko, Zh. Tekh. Fiz. **70** (2), 87 (2000) [Tech. Phys. **45**, 228 (2000)].
5. H. Ishizuka, Phys. Fluids B **2** (12), 3149 (1990).
6. C. A. Hapetanakos, L. K. Len, T. Smith, *et al.*, Phys. Fluids B **5** (7), 2295 (1993).

Translated by P. Pozdeev

The Volume of Information as a Measure of the Chaos Synchronization

A. V. Shabunin, V. V. Demidov, V. V. Astakhov, and V. S. Anishchenko

Saratov State University, Saratov, Russia
e-mail: valya@chaos.ssu.runnet.ru
Received December 4, 2000

Abstract—A characteristic is suggested for the evaluation of the degree of synchronization of the chaotic oscillations in a system of two coupled oscillators. The proposed value is tested by application to the case of two unidirectionally coupled logistic maps. It is shown that this characteristic is stable with respect to a low noise and a nonlinear distortion of the signal. © *2001 MAIK "Nauka/Interperiodica".*

The term "synchronization of chaos" refers to a number of physical phenomena such as the suppression of chaotic oscillations under the action of external periodic factors [1], the transition to completely identical oscillations in coupled oscillators (totally synchronized chaos) [2, 3] or to the oscillations identical to within a delay time in the subsystems (lag-synchronization) [4], the base frequency locking in the spectrum of chaotic oscillations [5], the instantaneous phase locking [6], and a deterministic relationship (including the case of delay-time $x_1(t) = f[x_2(t - \tau)]$ between oscillations in the subsystems (generalized synchronization) [7]. The somewhat ambiguous terminology reflects the variety of manifestations of the phenomenon of oscillation matching due to the interaction of oscillators.

For better understanding the interplay between various types of the chaos synchronization, it would be helpful to introduce a characteristic capable of measuring the degree of matching in the behavior of oscillators and quantitatively describing the degree of chaos synchronization in the system studied. It must be noted that a system can escape from the regime of chaos synchronization as a result of some change in the system parameters, this process proceeding gradually via a sequence of intermediate stages. For example, the breakage of a totally synchronized chaos may be accompanied by intermittent behavior, whereby the coupled oscillators exhibit synchronized oscillations for some time and chaotic oscillations otherwise [8, 9]. In this case, the task of quantitatively describing the escape from the synchronized chaos regime is also encountered.

We believe that the necessary requirements to a quantity measuring the degree of chaos synchronization are as follows: (i) a clear physical meaning facilitating the interpretation of the results; (ii) universality, making the measure applicable to various types of consistent behavior of the interacting subsystems; (iii) independence of a particular type of the dynamic system, making it possible to determine the degree of synchronization using the time patterns of oscillations in the subsystems; (iv) robustness, implying that small perturbations (changes in the oscillation regime, noise, distortions) would not significantly alter the value of the degree of synchronization.

With an allowance for these requirements, we suggest that such a measure of the consistent behavior can be represented by the amount of information provided by knowledge of the state of one oscillator for determining the state of another oscillator. If the state of one oscillator uniquely determines that of another, we may speak of the total synchronization (the degree of synchronization is unity). In the contrary, if the state of one oscillator does not influence the state of another, we may speak of the absence of synchronization (zero degree of synchronization). Using the language of mathematics, a quantitative measure of such information is offered by a difference between the total and conditional entropies calculated for all realizations of the oscillators [10]:

$$I = S_x - S_{x|y}. \tag{1}$$

The as-defined information is zero when the conditional entropy is equal to the total (unconditional) entropy, that is, when the state of the second oscillator (y) does not affect the variable (x) distribution of the first oscillator; the information is maximum (S_x) if the state of the second oscillator uniquely determines that of the first oscillator ($S_{x|y} = 0$). By normalizing the information to the unconditional entropy, we obtain a function acquiring a zero value in the case of completely independent behavior of oscillators and increasing to unity for the fully consistent behavior of the subsystems.

Thus, an expression for calculation of the degree of synchronization can be written as

$$\sigma = \frac{S_x - S_{x|y}}{S_x},$$

where $S_x = -\int p(x)\ln p(x)dx$, $p(x)$ is the probability density calculated for the realization $x(t)$, $S_{x|y} = -\int p(x|y)\ln p(x|y)dx$, and $p(x|y)$ is the probability density calculated for the realization $x(t)$ when the second oscillators occurs in the state y.

The proposed measure of the degree of chaos synchronization was used to study the escape from the state of totally synchronized chaos in a system of two unidirectionally coupled logistic maps:

$$x_{n+1} = \lambda x_n(1 - x_n), \tag{2}$$

$$y_{n+1} = \lambda[y_n + \gamma(x_n - y_n)](1 - [y_n + \gamma(x_n - y_n)]), \tag{3}$$

where x_n, y_n are the dynamic variables and γ is the coupling parameter. Equations (2) and (3) describe the active and responsive subsystems, respectively. The coupling is established by including the active system variable into the corresponding variable of the responsive system.

Each map is a system exhibiting a transition to chaos via the period-doubling bifurcations with an increasing parameter λ. The coupled maps are characterized by a more complicated dynamic behavior. The phase space of such a systems may contain several attractors, which corresponds to the phenomenon of multistable behavior. In a certain interval of the coupling parameter, the system exhibits a synchronized behavior, which is manifested by identical oscillations in the two subsystems: $x_n = y_n$. In the region of chaos, for each value of the parameter λ there is a certain critical value of the coupling parameter below which the synchronization of chaotic oscillations is broken.

Stability of a synchronized regime is determined by the transversal Liapunov index. For the system of maps (2) and (3), this index is

$$\Lambda_\perp = \Lambda_\| + \ln|1 - \gamma|, \tag{4}$$

where $\Lambda_\|$ is the Liapunov index for the direction tangential to the symmetric subspace $x = y$. The synchronous oscillations are transversally stable (unstable) if the transversal Liapunov index is negative (positive). As is seen from expression (4), the transversal Liapunov index for $0 < \gamma < 1$ is always smaller than the tangential index. Since the Liapunov index is negative for the regular regimes, the synchronous periodic oscillations may exist for any value of the coupling parameter. In the case of chaotic oscillations, the tangential Liapunov index is positive and formula (4) gives a critical value of the coupling parameter determining a boundary of the synchronization region. Crossing this boundary is accompanied by the "blowout" bifur-
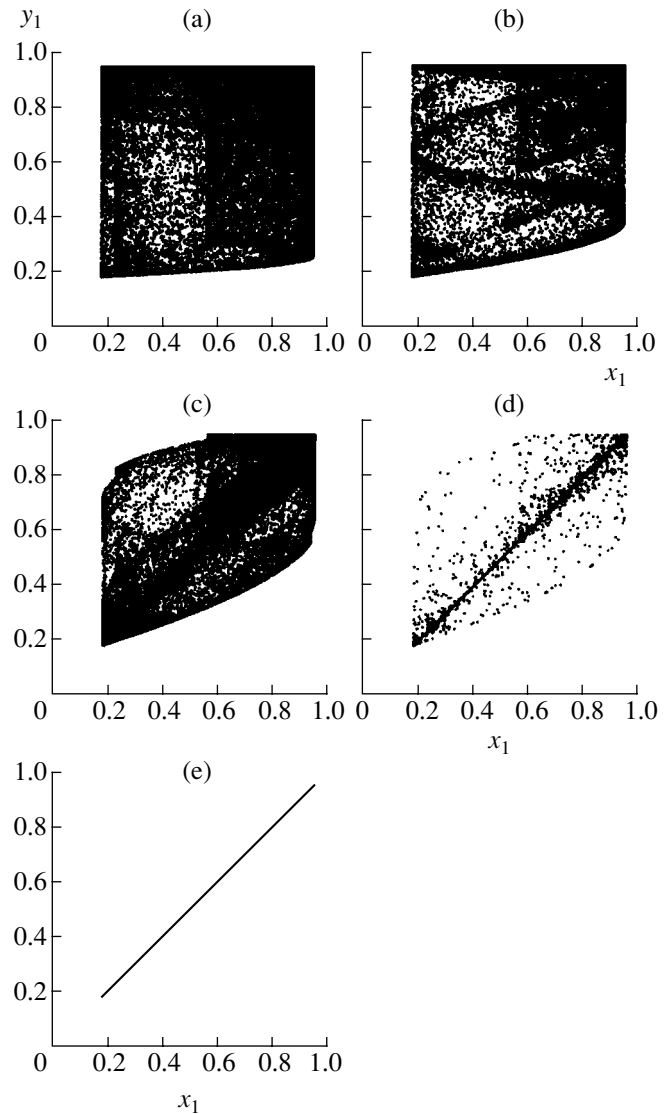
Fig. 1. The projections of phase portraits of the system of two unidirectionally coupled logistic maps for various values of the coupling parameter $\gamma = 0.05$ (a), 0.14 (b), 0.33 (c), and 0.36 (d, with ~0.00001 noise; e, without noise).

cation [11], after which the synchronous chaotic oscillations are changed by asynchronous, However, a negative value of the transversal Liapunov index does not provide for the robustness of the synchronization regime (i.e., it does not ensure that the existing regime will be preserved in the presence of a small external noise or a small nonidentity of the subsystems). If a chaotic attractor contains limiting trajectories for which the transversal Liapunov index is positive, the system exhibits the phenomenon of "bubbling," whereby adding an arbitrarily small noise leads to an intermittency between the synchronous and asynchronous behavior [8, 9, 11].

The events described above are observed in the system under consideration. We have studied behavior of the system described by Eqs. (2) and (3) depending on

σ, Λ_n
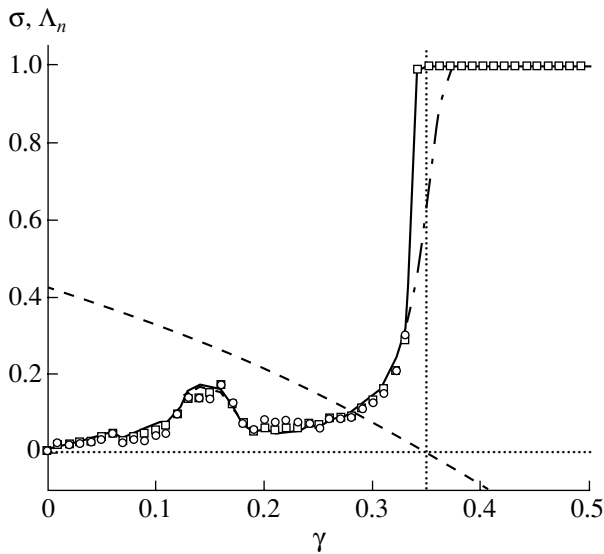
Fig. 2. Plots of the degree of synchronization versus coupling parameter (see the text for explanations).

the coupling parameter γ, while the partial system parameter was fixed at $\lambda = 3.8$. This value of λ corresponds to a developed chaos imaged by a schlicht chaotic attractor. In the region of $0.38 < \gamma < 1$, we observe a robust regime of totally synchronized chaos. As the coupling parameter decreases to $0.35 < \gamma < 0.38$, the regime of synchronized chaos is no longer robust. Here, the synchronous oscillations are observed after a long transient process only in a system without noise. Introducing an arbitrary small noise into this system leads to intermittency, whereby the time realization x–y represents a prolonged "laminar" stage featuring a synchronous behavior with random "turbulent" spikes of the trajectory away from the symmetric subspace. This behavior is referred to as the on–off intermittency, which corresponds to the so-called "bubbling" attractor. This behavior is illustrated in Figs. 1d and 1e showing an attractor in the presence of a small-amplitude noise (~0.00001) and in the absence of noise, respectively. If the coupling parameter is decreasing further, the transversal Liapunov index changes sign from negative to positive in the vicinity of $\gamma = 0.35$, which corresponds to a blowout bifurcation after which the synchronized chaos is no longer observed in the system. The corresponding phase portraits are presented in Figs. 1a–1c. As the coupling parameter keeps decreasing, the attractor is "swelling"; at $\gamma < 0.05$, the phase portrait represents a nearly square region (Fig. 1a).

The above-described evolution of the system dynamics is well predicted based on the information function S. The corresponding plots are constructed in Fig. 2 as the degree of synchronization versus the coupling parameter in a system without noise (solid curve) and with a small noise (dash–dot curve). In the noiseless system, the decay begins immediately at the point where the transversal Liapunov index changes sign. For

illustration, also plotted in Fig. 2 are the plot of the transversal Liapunov index versus the coupling parameter (dotted curve) and two dashed lines (horizontal and vertical) indicating the point where this index passes through a zero value. The degree of synchronization sharply drops from unity at $\gamma = 0.35$ to $\simeq 0.15$ at $\gamma = 0.3$. As the coupling parameter is reduced further, the degree of synchronization slowly decreases to $\simeq 0.05$ at $\gamma = 0.2$, then exhibits a local increase to reach a characteristic maximum ($S \simeq 0.17$) at $\gamma = 0.14$, and then monotonically decreases to zero at a zero coupling parameter. The local increase in the degree of synchronization at $\gamma = 0.14$ is related to a change in the structure of the attractor. As is seen in Fig. 1b, the attractor observed for this value of γ includes a region apparently corresponding to an unstable quasiperiodic motion (in which the trajectory occurs for a considerable time), rather than represents uniformly distributed phase points.

When a small noise (~0.00001) is introduced into the system, a rapid decrease in the degree of synchronization begins significantly earlier (with respect to the coupling parameter) as reflected by the dash–dot curve in Fig. 2, which is indicative of the bubbling phenomenon. A significant difference in the degree of synchronization for the system with and without noise is observed only in this region of $\gamma \simeq 0.34$. In other regions of the coupling parameter, the values of σ in both cases are virtually the same (Fig. 2). Thus, a significant influence of noise on the degree of synchronization is related only to a nonrobust character of the chaos synchronization, rather than to instability of the proposed characteristic σ.

The proposed synchronization characteristic is stable not only to a small noise but to a small nonlinear distortion of the signals as well. To illustrate this statement, we will modify the time realization, used to calculate the degree of synchronization, by adding a nonlinear term

$$x \longrightarrow x + \delta x^2,$$

where δ is the parameter of nonlinearity. The results of calculations for the modified realizations with $\delta = 0.05$ and 0.2 are presented in Fig. 2 by open squares and circles, respectively. As is seen, the points obtained for the signal with nonlinear distortions fit to the initial (undistorted) curve. The invariance with respect to nonlinear distortions makes the proposed characteristic applicable to the study of generalized synchronization cases of the type $x_n = f(y_n)$ with a deterministic character of the function f.

Conclusion. We have proposed a characteristic providing for a quantitative description of the degree of synchronization in the oscillations of two coupled oscillators. This characteristic was tested by application to two unidirectionally coupled logistic maps capable of featuring both totally synchronized chaos and a bubbling behavior upon the synchronization breakage.

It was demonstrated that the proposed quantity is stable with respect to small noise and nonlinear distortions of the signal studied. In the following, we are planning to study applicability of the proposed quantity to description of the other types of synchronization (phase locking) and compare this characteristic to that based on the coherency function [12].

REFERENCES

1. E. N. Dudnik, Yu. I. Kuznetsov, I. I. Minakova, and Yu. M. Romanovskiǐ, Vestn. Mosk. Univ., Ser. 3: Fiz., Astron. **24** (4), 84 (1983).

2. H. Fujisaka and T. Yamada, Prog. Theor. Phys. **69** (1), 32 (1983).

3. V. S. Afraǐmovich, N. N. Verichev, and M. I. Rabinovich, Izv. Vyssh. Uchebn. Zaved., Radiofiz. **29** (9), 1050 (1986).

4. M. G. Rosenblyum, A. S. Pikovsky, and J. Kurths, Phys. Rev. Lett. **78**, 4193 (1997).

5. V. S. Anishchenko, T. E. Vadivasova, D. É. Postnov, and M. A. Safonova, Radiotekh. Élektron. (Moscow) **36** (2), 338 (1991).

6. M. G. Rosenblum, A. S. Pikovsky, and J. Kurths, Phys. Rev. Lett. **76** (11), 1804 (1996).

7. H. D. I. Abarbanel, N. F. Rulkov, and M. M. Sushchik, Phys. Rev. E **53**, 4528 (1996).

8. V. Astakhov, A. Shabunin, T. Kapitaniak, and V. Anishchenko, Phys. Rev. Lett. **79** (6), 1014 (1997).

9. V. Astakhov, M. Hasler, T. Kapitaniak, *et al.*, Phys. Rev. E **58** (5), 5620 (1998).

10. Yu. L. Klimontovich, *Statistical Physics* (Nauka, Moscow, 1982; Harwood, Chur, 1986).

11. P. Ashvin, J. Beuescu, and I. Stewart, Phys. Lett. A **193**, 126 (1994).

12. V. S. Anishchenko, V. V. Astakhov, V. V. Nikolaev, and A. V. Shabunin, Radiotekh. Élektron. (Moscow) **45** (2), 196 (2000).

Translated by P. Pozdeev

Stability of the Interphase Boundary
during the Crystallization of Eutectics

A. P. Gus'kov

Institute of Solid State Physics, Russian Academy of Sciences, Chernogolovka, Moscow oblast, Russia
Received January 9, 2001

Abstract—Stability of the interphase boundary during the oriented crystallization of a binary melt was studied with an allowance of the external temperature gradient. It is demonstrated that the interphase boundary is unstable if the system composition is close to eutectic. The instability development leads to a rodlike (or platelike) periodic distribution of components in the bulk of the solid phase. Dependence of the period of this structure on the phase boundary velocity is determined. © *2001 MAIK "Nauka/Interperiodica".*

The phenomenon of periodic structure formation during the solidification of eutectic melts is still unexplained [1]. The most popular theory capable of describing the crystallization of eutectic melts with the formation of periodic structures is the theory of Jackson and Hunt [2]. However, this model does not indicate any reasons for this process and provides no satisfactory explanation of the characteristic experimental hyperbolic dependence of the period of the structure formed on the velocity of propagation of the interphase boundary.

As was recently demonstrated [6, 7], the periodic structure formation during crystallization of a binary alloy near the eutectic point is well explained by instability of the interphase. However, a stationary solution of the model equation becomes physically senseless at a sufficiently small velocity of the interphase boundary (interface) propagation [8]. However, such small velocities can be encountered in experiments on the crystal growth. In order to eliminate this drawback, the proposed model introduces an external temperature field (gradient). This situation is physically equivalent to heating a thin plate from an external heat source by means of heat transfer via an ambient medium.

Let T denote the temperature normalized to the phase transition temperature T_{e0} corresponding to the initial component concentration C_0; C, the component concentration normalized to the initial value; $y = \alpha y_r$, $z = \alpha z_r$, and $\tau = \alpha^2 \chi_0 \tau_r$, the dimensionless coordinates and time; $D = D_r / \chi_0$, the dimensionless diffusion coefficient in the liquid phase; $\chi = \chi_r / \chi_0$, the thermal conductivity coefficient; ε, the phase transition heat ε_r normalized to the specific heat capacity and the phase transition temperature; and φ_r, the heat transfer coefficient normalized to the specific heat capacity ($y_r, z_r, \tau_r, D_r, \chi_r$, and ε_r are the corresponding dimensional quantities; $\chi_0 = 10^{-5}$ m²/s; $\alpha = 10^2$ m⁻¹).

The proposed model takes into account the thermal conductivity in the liquid and solid phases and the component diffusion in the liquid phase. To simplify the calculations, we omit the coordinate x in the equations. Primed quantities refer to the solid phase. The external temperature field is represented by the function of internal sources $T_{ext}(z)$ described by an exponential function

$$T_{ext} = \begin{cases} T'_{ext}(\infty) + (T_{ext}(\infty) + T_x - T'_{ext}(\infty)) \\ \times \exp\left(\dfrac{\phi_0}{(T_{ext}(\infty) + T_x - T'_{ext}(\infty))}z\right); \\ T_{ext}(\infty) + T_x \exp\left(\dfrac{\phi_0}{T_x}z\right) \end{cases} \quad (1)$$

with the parameters satisfying the following conditions: at infinity, the temperature acquires the preset values $T'_{ext}(-\infty)$ and $T_{ext}(\infty)$; the function branches are matched at $z = 0$, where $T'_{ext}(0) = T_{ext}(0)$ and the temperature gradient has a preset value ϕ_0. The constant T_x is determined from the boundary conditions.

A significant circumstance is that the problem formulated without an allowance for the external temperature field is subject to a restriction concerning the temperature gradient at the interphase boundary. Let us set the following thermal parameters corresponding to solidification of the Al₂O₃ + Zr₂O₃ melt: $\chi_r = 5 \times 10^6$ m²/s, $\varepsilon_r = 10^6$ J/kg, and $D_r = 10^{-8}$ m²/s; the heat transfer coefficient is taken equal to $\varphi_r = 10^6$ s⁻¹. The experimental parameters correspond to the crystal growth conditions: $V_S = 10^{-5}$ m/s; $T'_{ext}(-\infty) = 1900$ K; $T_{ext}(\infty) = 2100$ K; $T_{e0} = 2000$ K. These values will determine the temperature gradient ϕ_{0r} in the problem with an external temperature field. It is assumed that a solution to the problem with the temperature gradient ϕ_{0r} is

equivalent to the solution of the problem without an external field, with the temperature gradient at the interphase boundary in the solid phase equal to that in the problem taking this external field into account.

Let us consider dependence of the stationary temperature in the vicinity of the interphase boundary for two values of the external field gradient (Fig. 1); note that $T_x = -2.83$ K for $\phi_{0r} = 10^3$ K/m and $T_x = -3.56$ K for $\phi_{0r} = 2 \times 10^3$ K/m. In the crystal growth experiments, the temperature gradient of the external field in the vicinity of the interphase boundary usually falls within 10^3–10^4 K/m. As seen, this is exactly the interval where a solution to the stationary problem without external temperature field loses physical sense (the temperature in the liquid phase monotonically decreases with increasing distance from the interphase boundary). This behavior is formally understood: the solution contains a single exponent, which can describe only monotonic variation.

In the experiments [3], the growth of an eutectic structure is frequently accompanied by a dendrite growth. In theoretical descriptions, the time instant when the temperature gradient in front of the interphase boundary (crystallization front) reaches a certain critical value is related to the onset of dendrite growth [8]. The results of our calculations explain the simultaneous growth of dendrites and an eutectic structure: if the external temperature field gradient in the liquid phase in front of the interphase boundary is sufficiently small, the crystal phase features conditions for the dendrite growth.

Let us introduce the external temperature field (1) into the model developed in [6]. In the curvilinear coordinates connected to the interface [6], the boundary problem for small perturbations has the following form:

$$\chi' \frac{\partial^2 T'_m}{\partial z^2} + V_S \frac{\partial T'_m}{\partial z} + (\chi' K^2 - \omega - \varphi) T'_m$$

$$= \frac{(\chi' K^2 - \omega)}{\omega} V_m \frac{\partial T'_S}{\partial z}; \quad -\infty < z \leq 0; \tag{2}$$

$$\chi \frac{\partial^2 T_m}{\partial z^2} + V_S \frac{\partial T_m}{\partial z} + (\chi K^2 - \omega - \phi) T_m$$

$$= \frac{(\chi K^2 - \omega)}{\omega} V_m \frac{\partial T'_S}{\partial z}; \quad 0 \leq z < \infty; \tag{3}$$

$$D \frac{\partial^2 C_m}{\partial z^2} + V_S \frac{\partial C_m}{\partial z} + (D K^2 - \omega) C_m$$

$$= \frac{(D K^2 - \omega)}{\omega} V_m \frac{\partial C_S}{\partial z}; \quad 0 \leq z < \infty; \tag{4}$$

$$\chi' \frac{\partial T'_m}{\partial z} \bigg|_{z = 0 - 0} - \chi \frac{\partial T_m}{\partial z} \bigg|_{z = 0 + 0} = \varepsilon V_m T'_m \big|_{z = 0 - 0} \tag{5}$$

$$= T_m \big|_{z = 0 + 0} \quad T_m \big|_{z \to \infty} = 0;$$

$$D \frac{\partial C_m}{\partial z} \bigg|_{z = 0 + 0} = (1 - k)(V_S C_m + C_S V_m) C_m \big|_{z \to \infty} = 0; \tag{6}$$

$$V_m = \theta T_{m0} + \gamma C_{m0}; \quad \theta = \frac{\partial V}{\partial T} \bigg|_{T = T_S(0)};$$

$$\gamma = \frac{\partial V}{\partial C} \bigg|_{C = C_S(0)}, \tag{7}$$

where $k = C_S(\infty)/C_S(0)$ and $C_S(z)$ is a solution to the stationary problem. The coefficient k enters into the boundary conditions (6) and (7).

As is known from the theory of equilibrium phase transitions, the thermodynamics strictly relates the interval of k values to the slope of the phase transition temperature as a function of the component concentration (this dependence is expressed by condition (7)). This relationship is broken upon the phase separation in the melt [7]. This circumstance explains a mechanism of the interphase boundary instability. Indeed, if the melt composition is close to eutectic, the system (by definition) possesses a minimum (within the framework of this model, close to minimum) phase transition temperature. When the melt exhibits phase separation in some region near the interphase boundary, the phase transition temperature in this region increases and the melt becomes more supercooled. This leads to a further phase separation, and this process may proceed up to the complete phase separation in the system.
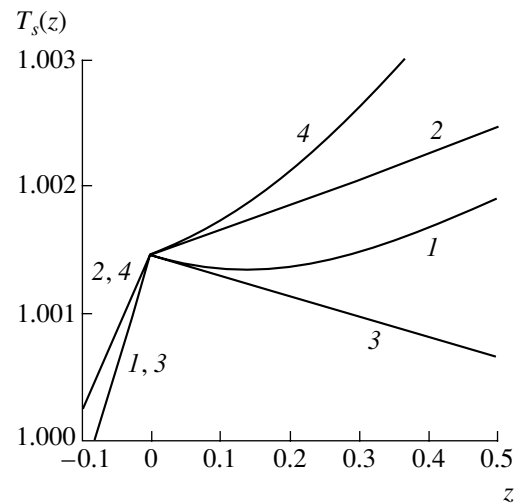
Fig. 1. The plot of stationary temperature $T_s(z)$ versus spatial coordinate z for the problem of crystallization (1, 2) with and (3, 4) without an allowance for the external temperature field for $\phi_0 = 10^3$ (1, 3) and 2×10^3 K/m (2, 4).
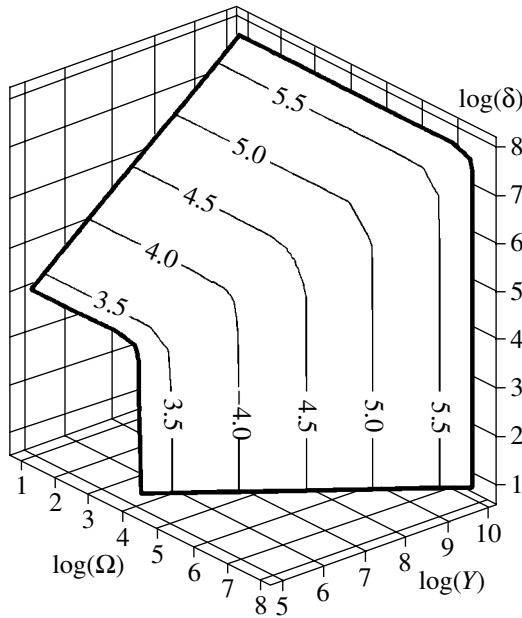
Fig. 2. Trajectories $\theta = \text{const}$ on the $\delta(\Omega, Y)$ surface.

The above qualitative considerations are well illustrated by the experimental data reported in [1], where an almost complete phase separation was observed. Since the special features of the eutectic phase diagram do not enter into the boundary conditions, the results of calculations are valid for the melts with different dependences of the phase transition temperature on the component concentration. We may suggest that the structure with a given periodicity is formed by a phase possessing a higher melting temperature. However, this question requires special investigation.

It is suggested that solutions to the above problem has the following form [5]:

$$T' = T'_S(z) + T'_m(z)\exp(\omega\tau + Ky);$$

$$T = T_S(z) + T_m(z)\exp(\omega\tau + Ky);$$

$$C = C_S(z) + C_m(z)\exp(\omega\tau + Ky);$$

$$\omega = \omega_1 + i\omega_2; \quad K = K_1 + iK_2;$$

$$T'_m(z) \ll T'_S(z); \; T_m(z) \ll T_S(z); \; C_m(z) \ll C_S(z),$$

where $T'_S(z)$, $T_S(z)$, $C_S(z)$ are solutions to the stationary problem.

In order to obtain a dispersion equation for the system studied, we must first obtain a solution to the problem (2)–(7). At the interphase boundary, this solution yields a linear system of equations with respect to the coefficients $T_{m0} = T_m(0)$ and $C_{m0} = C_m(0)$

$$(S'_T - S_T)T_{m0} - \eta V_{m0} = 0, \tag{8}$$

$$[S + 2(1 - k)]C_{m0} - (k - 1)\xi V_{m0} = 0, \tag{9}$$

where Eq. (8) is a solution to the equation of thermal conductivity and Eq. (9) is a solution to the diffusion equation. Note that all characteristics of the external temperature field (1) enter into the parameter η. Here, S'_T, S_T, and S are the roots of the characteristic equations for Eqs. (2)–(4); the η and ξ values depend on the system parameters ($\xi \neq 0$ for $k = 1$). Substituting expansion (7) into Eqs. (8) and (9), we obtain the dispersion equation

$$[(S'_T - S_T) - \eta\theta][S + 2(1 - k) + (1 - k)\xi\gamma]$$
$$+ (1 - k)\xi\eta\gamma\theta = 0. \tag{10}$$

The scheme of derivation of the dispersion equation is presented in more detail elsewhere [9]. For the component concentrations close to eutectic, k is close to unity. For a sufficiently small difference $1 - k$, Eq. (10) can be written in the flowing form:

$$[(S'_T - S_T) - \eta\theta]S = 0. \tag{11}$$

This equation separates into a system of two real equations corresponding to the real and imaginary parts of Eq. (11)

$$\begin{cases} \text{Re}((S'_T - S_T) - \eta\theta)\text{Re}S \\ - \text{Im}[(S'_T - S_T) - \eta\theta]\text{Im}S = 0 \\ \text{Re}((S'_T - S_T) - \eta\theta)\text{Im}S \\ - \text{Im}[(S'_T - S_T) - \eta\theta]\text{Re}S = 0, \end{cases} \tag{12}$$

where the imaginary part of S is as follows:

$$\text{Im}(S)$$
$$= -0.5\sqrt{2\sqrt{(1 + Y + \delta)^2 + \Omega^2} - 2(1 + Y + \delta)}. \tag{13}$$

For further simplification, we will use the results of numerical calculations. For this purpose, we select the values of the distribution coefficient $k = 1.03$, the liquidus slope $m = -0.05$ (i.e., the same as in [6], where k corresponded to phase separation in the melt at the interphase boundary), and the external temperature gradient $\phi_{0r} = 10^4$ K/m. The numerical calculation was performed (as in [5]) using the model of growth by screw dislocations. The kinetic parameter θ is considered as the control parameter determined from a comparison of the results of calculation to experiment. The solution is represented as a surface $\delta(\Omega, Y)$ (see Fig. 2), where

$$\delta = \frac{4D\omega_1}{V_S^2}, \quad \Omega = \frac{4D\omega_2}{V_S^2}, \quad Y = \frac{4D^2K_2^2}{V_S^2}$$

are the growth increment, the frequency of time pulsations, and the frequency of spatial distortions, respectively. In Fig. 2, the trajectories $\theta = \text{const}$ (with the logarithm of the absolute θ value indicated on the curves) are constructed on this surface. In order to select a par-

ticular θ value, we take the results of the experiments used in the calculations performed in [6] (for a given interface velocity, the rodlike structure period is 1 μm). For the values selected, the interphase boundary has a spatial mode with the frequency $\log(Y) \approx 8.5$, which corresponds to $\log(|\theta|) \approx 5$. According to the selection hypothesis, the interphase boundary will exhibit no time pulsations because the corresponding trajectory monotonically increases as $\Omega \longrightarrow 0$. Therefore, the point of maximum growth increment corresponds to $\Omega = 0$ and expression (13) acquires the following form:

$$\text{Im}(S)$$
$$= -0.5\sqrt{2\sqrt{(1 + Y + \delta)^2} - 2(1 + Y + \delta)} \equiv 0.$$

By the same token, we may readily show that the expressions for $\text{Im} S'_T$ and $\text{Im} S_T$ also turn zero. Therefore, the set of Eqs. (12) at the point of maximum growth increment reduces to a single equation from which we obtain

$$\text{Re}(S'_T) - \text{Re}(S_T) - \theta\text{Re}(\eta) = 0. \qquad (14)$$

Let us consider the expression for $\text{Re}(S_T)$:

$$\text{Re}(S_T) = -1 + 0.5$$

$$\times \sqrt{2\sqrt{\left(1 + \frac{4\chi\phi}{V_S^2} + \frac{\chi^2 Y}{D^2} + \frac{\chi\delta}{D}\right)^2} + 2\left(1 + \frac{4\chi\phi}{V_S^2} + \frac{\chi^2 Y}{D^2} + \frac{\chi\delta}{D}\right)}.$$

Upon substituting the numerical data, we obtain the relationships

$$1 \ll \frac{4\chi\phi}{V_S^2} \ll \frac{\chi\delta}{D} \ll \frac{\chi^2 Y}{D^2}.$$

Analogous relationships are obtained for $\text{Re}(S'_T)$. The expression for $\text{Re}(\eta)$ can be written as

$$\text{Re}(\eta) = \frac{2\varepsilon}{V_S}(1 + \beta).$$

Figure 3 shows variation of the parameter β along the trajectory $\delta(\Omega, Y)$. The calculations showed that $\beta \ll 1$. Ignoring small terms in $\text{Re}(S_T)$, $\text{Re}(S'_T)$, and $\text{Re}(\eta)$ and substituting these values into Eq. (14), we arrive at the equation

$$|\chi_1 \pm \chi| \sqrt{Y} - \frac{2\varepsilon D\theta}{V_S} = 0. \qquad (15)$$

As is seen, neglecting parameter β excluded all parameters of the external temperature field. Using Eq. (15), we obtain an expression for the period of spatial distortions λ,

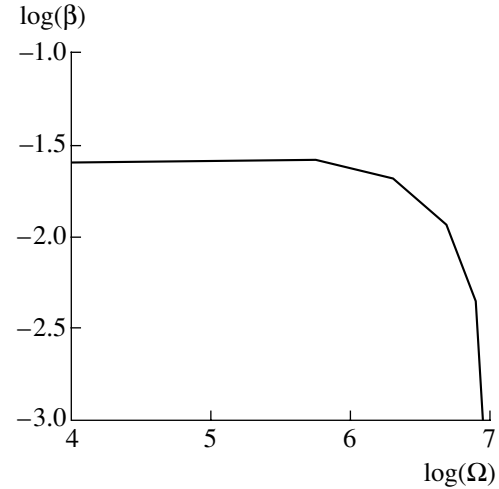$$\lambda = \frac{2\pi|\chi_1 \pm \chi|}{\varepsilon|\theta|},$$

Fig. 3. The plot of $\beta(\Omega)$.

which coincides with a solution to the eutectic problem not taking into account the external temperature field. For the model of growth by screw dislocations, this expression yields a relationship $\lambda(V_S)$ coinciding with the experimental curves [7]. With an allowance of the external temperature field in the crystallization model, we also explained another nontrivial experimental fact, whereby the temperature field does not affect the eutectic structure period for the values of parameters close to those used in the crystal growth experiments.

REFERENCES

1. V. A. Borodin, M. Yu. Starostin, and T. N. Yalovets, J. Cryst. Growth **104**, 143 (1990).

2. K. A. Jackson and J. D. Hunt, Trans. Metall. Soc. AIME **236**, 1129 (1966).

3. R. Elliott, *Eutectic Solidification Processing: Crystalline and Glassy Alloys* (Butterworths, London, 1983; Metallurgiya, Moscow, 1987).

4. M. Plapp and A. Karma, Phys. Rev. E **60**, 6865 (1999).

5. J. D. Hunt and S.-Z. Lu, in *Handbook of Crystal Growth* (North-Holland, Amsterdam, 1994), Vol. 2, Part B, Chap. 17.

6. A. P. Gus'kov, Dokl. Akad. Nauk **366**, 486 (1999) [Dokl. Phys. **44**, 330 (1999)].

7. A. Gus'kov, Comput. Mater. Sci. **17**, 555 (2000).

8. N. A. Avdonin, in *Crystal Growth* (Yerevan, 1975), Vol. XI.

9. A. P. Gus'kov, Dokl. Akad. Nauk **349**, 468 (1996) [Phys. Dokl. **41**, 339 (1996)].

Translated by P. Pozdeev

Effect of Nitrogen Oxides on the Sulfur Dioxide Removal from Flue Gases Under the Action of Pulsed Electron Beams

G. V. Denisov, D. L. Kuznetsov, Yu. N. Novoselov, and R. M. Tkachenko

Institute of Electrophysics, Ural Division, Russian Academy of Sciences, Yekaterinburg, Russia
e-mail: nov@iep.uran.ru
Received December 19, 2000

Abstract—The process of sulfur dioxide (SO_2) oxidation under the action of a microsecond-pulsed electron beam was experimentally studied in model gas mixtures with various initial concentrations of nitrogen dioxide (NO_2). It is shown that the presence of NO_2 significantly affects the process of SO_2 oxidation. © *2001 MAIK "Nauka/Interperiodica".*

One of the methods used to purify the flue gases of thermal power plants from sulfur and nitrogen oxides is based on gas ionization by pulsed electron beams. Previously [1], we reported on the results of investigations of the process of sulfur dioxide (SO_2) removal from a model gas mixture under the action of pulsed electron beams. It was demonstrated that use of a beam with the optimum parameters provides for the SO_2 elimination by means of a plasma-chemical chain oxidation mechanism at a relatively small energy consumption (~1 eV per SO_2 molecule). However, the experiments described in [1] were carried out with model flue gas mixtures differing from real flue gases by the absence of NO_x components. Below we present the results of experiments aimed at determining the laws of SO_2 removal by microsecond-pulsed electron beams from gas mixtures modeling real flue gases (i.e., containing NO_x as well).

The experiments were performed using an electron accelerator analogous to that described in [2]. The electron beam produced by the accelerator had a 10 × 100 cm cross section, an energy of 200 keV, a pulse width at half maximum of 5 μs, and a beam current density of 12.5×10^{-3} A/cm². The irradiated gas volume was 12 dm³. The model gas mixture contained N_2 (~88.5%), O_2 (10%), SO_2 (0.5% or 5000 ppm), NO_2 (up to 0.1% or 1000 ppm), and H_2O (1%). The SO_2 concentration was measured by gas chromatography with an experimental error not exceeding 3%. The analytical procedure employed did not allow us to determine simultaneously the content of both sulfur and nitrogen oxides. For this reason, we determined the initial mixture composition and then monitored the concentration of only one type of impurity (in this study, sulfur dioxide).

During the experiment, we determined the amount of sulfur dioxide removed by a series of pulses, the degree of purification η, and the specific energy consumption ε per SO_2 molecule removed. The η and ε values were calculated by the formulas

$$\eta = \Delta[SO_2]/[SO_2]_0,$$

$$\varepsilon = WN/e\Delta[SO_2] \text{ (eV/molecule)},$$

where $\Delta[SO_2]$ is a change in the concentration of sulfur dioxide during a series of electron pulses (in cm⁻³); $[SO_2]_0$ is the initial sulfur dioxide concentration in the model mixture (cm⁻³); W is the beam energy absorbed in the gas per pulse (J/cm³); N is the number of pulses in the series; and e is the electron charge (in Coulombs). The value of the electron beam energy W absorbed in the gas was determined by a standard procedure using thin-film dose meters.

Figure 1 shows typical plots illustrating a decrease in the sulfur dioxide concentration $[SO_2]$ with increasing number of irradiation pulses (beam shots) N for the
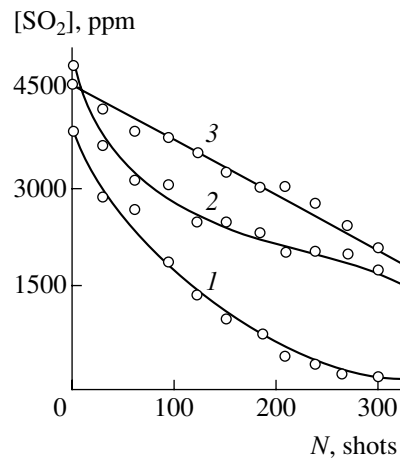
**Fig. 1.** Variation of the sulfur dioxide concentration with increasing number N of electron beam shots in a model gas mixture (*1*) free of NO_2 and (*2, 3*) initially containing 1000 and 500 ppm NO_2, respectively.

model gas mixtures with various initial NO_2 content. As can be seen, the kinetics of decrease in the sulfur dioxide concentration depends on the nitric oxide content in the initial mixture. In the absence of NO_2 (curve *1*), the efficiency of SO_2 removal is maximal and the degree of purification reaches $\eta \sim 98\%$. The presence of NO_2 (1000 or 500 ppm) decreases the efficiency of SO_2 elimination (curves *2* and *3*), so that the degree of purification drops down to 63 and 60%, respectively.

An energy characteristic of the process of sulfur dioxide removal from the model gas mixture is offered by the specific energy consumption ε per SO_2 molecule. Figure 2 shows the plots of ε (curve *1*) and the degree of purification η (curve *2*) versus the initial NO_2 concentration in the mixture. The number of pulses in all cases was the same ($N = 300$). As is seen, an increase in the initial NO_2 concentration leads to a decrease in the degree of the mixture purification from sulfur dioxide and to an increase in the energy consumption for the removal of every SO_2 molecule.

An evident reason for this behavior is that the presence of NO_2 in the gas mixture leads to a change in the plasma-chemical reaction pathways involved in the SO_2 removal. However, the mechanism of this influence is not quite clear. According to [1, 3], the main role in the process of SO_2 elimination belongs to negative oxygen ions O_2^- initiating the chain oxidation reactions. Under the experimental conditions studied, these ions are most intensively formed by the three-body attachment process [4]

$$e + O_2 + O_2 \Rightarrow O_2 + O_2^-. \qquad (1)$$
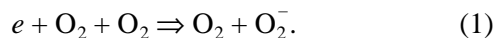
The reaction chain also involves SO_2^- ions formed as a result of the charge exchange

$$O_2^- + SO_2 \Rightarrow O_2^* + SO_2^-, \qquad (2)$$

where O_2^* denotes vibrationally excited oxygen molecules. The presence of NO_2 in the gas mixture may initiate certain competitive processes leading to a decrease in the concentration of negative oxygen O_2^- and/or molecular SO_2^- ions. A possible process of this type is the attachment of thermalized electrons from the beam to electronegative NO_2 molecules possessing an electron affinity of 2.42 eV:

$$e + NO_2 \Rightarrow NO_2^-. \qquad (3)$$

However, estimates obtained for the experimental conditions studied showed that the formation of negative ions via reaction (1) proceeds at a rate 40 times higher than the analogous process via reaction (3). Thus, the loss of electrons via the attachment in reaction (3) can-
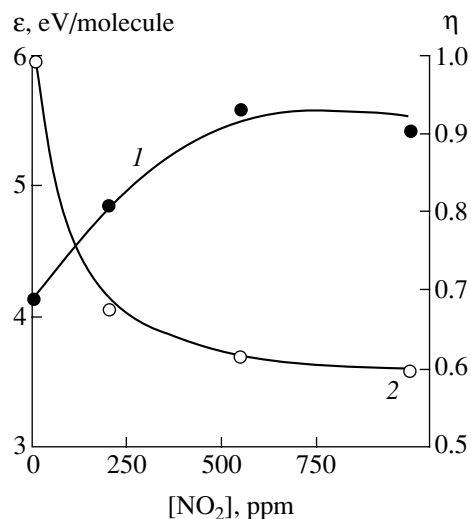

Fig. 2. Plots of (*1*) the specific energy consumption ε per SO_2 molecule and (*2*) the degree of purification η from SO_2 versus the initial NO_2 concentration in the gas mixture ($N = 300$).

not significantly affect the initiation of the SO_2 chain oxidation process.

Nitrogen dioxide noticeably influences the concentration of SO_2^- ions. In the ionized gas mixture, an intensive process that competes with the exchange reaction (2) is the recharge reaction

$$O_2^- + NO_2 \Rightarrow O_2^* + NO_2^-, \qquad (4)$$

the rate constant of which ($k_4 \sim 12 \times 10^{-10}$ cm^3/s [5]) is considerably higher than that of reaction (2) ($k_2 \sim 4.5 \times 10^{-10}$ cm^3/s). However, the most significant factor decreasing the efficiency of SO_2 removal in the presence of nitrogen oxides is the recharge of negative ions

$$SO_2^- + NO_2 \Rightarrow SO_2 + NO_2^-, \qquad (5)$$
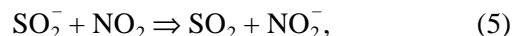
which is also a sufficiently intensive process with a reaction rate constant of $k_5 \sim 4.3 \times 10^{-10}$ cm^3/s [5]. The results of simple calculations for the experimental conditions studied show that adding 500–1000 ppm NO_2 to an initial mixture containing $[SO_2]_0 \sim 4500$ ppm decreases the concentration of SO_2^- ions approximately by two orders of magnitude. Accordingly, the probability of the SO_2 chain oxidation process drops, the degree of purification decreases, and the energy consumption for the removal of SO_2 molecules increases (Fig. 2).

The reactions considered above, albeit without describing all the possible pathways, allow the general regularities to be established. However, the quantitative effect of NO_2 is still unclear. As is seen from Fig. 2, the specific energy consumption ε increases when the nitrogen concentration rises up to ~500 ppm and

decreases when the nitrogen content grows further. The same pattern follows from curves *2* and *3* in Fig. 1. Elucidation of the mutual influence of sulfur and nitrogen oxides removed from flue gases under the action of pulsed electron beams requires additional investigation.

REFERENCES

1. Yu. N. Novoselov, G. A. Mesyats, and D. L. Kuznetsov, J. Phys. D: Appl. Phys. **34** (8), 1248 (2001).

2. K. A. Garusov, D. L. Kuznetsov, Yu. N. Novoselov, and V. V. Uvarin, Prib. Tekh. Éksp., No. 3, 180 (1992).

3. E. I. Baranchikov, G. S. Belen'kiĭ, V. P. Denisenko, *et al.*, Dokl. Akad. Nauk SSSR **315** (1), 120 (1990).

4. H. S. W. Massey, *Negative Ions* (Cambridge Univ. Press, Cambridge, 1976; Mir, Moscow, 1979).

5. L. I. Virin, R. V. Dzhagatspanyan, G. V. Karachevtsev, *et al.*, *Ion-Molecule Reaction in Gases* (Nauka, Moscow, 1979).

Translated by P. Pozdeev

Experimental Investigation of the Interaction of Two Acoustic Shock Waves

A. L. Surkaev, V. G. Kul'kov, and G. N. Talyzov

Volzhskiĭ Polytechnical Institute, Volgograd State Technical University, Volzhskiĭ, Russia
e-mail: vfaculty@volpi.ru
Received January 29, 2001

Abstract—The hydrodynamic pulse pressure in a wave formed by the electric explosion of metallic conductors was experimentally studied. The pattern of interaction of two such waves propagating in opposite directions in a medium filling a bounded volume of cylindrical geometry is indicative of the nonlinear character of the processes in the system. © *2001 MAIK "Nauka/Interperiodica".*

Our aim was to experimentally determine the hydrodynamic pulse pressure of an acoustic shock wave and to study the interaction of two such waves generated by the electric explosion of metallic conductors within a bounded volume of cylindrical geometry. The experiments were carried out in a specially designed setup (Fig. 1). A metal cylinder *1* with sufficiently thick walls modeled an explosion chamber with an absolutely hard boundary. The exploding metal conductors *2* connected to the rod electrodes *3* were coaxially mounted in the explosion chamber with the aid of adjustable insulator insets *4*. The explosion chamber was filled with a condensed medium *5* (in this case, technical-purity water). At the edges, the chamber was hydroinsulated with elastic rubber plugs *6* maintaining the central electrode arrangement.

The hydrodynamic pulse pressure was monitored with the aid of a piezoceramic waveguide transducer *7* [1]. The transducer was mounted on the chamber wall using a screw joint [2]; the hole in the chamber wall was matched to the stepped concentrator profile. The length of a small-diameter part of the stepped waveguide was equal to the wall thickness in the hole profile. Thus, the concentrator edge occurred in the plane of the hard wall; this positioning decreased manifestations of the wave diffraction. The small cross-sectional area of the transducer edge allowed the local parameters of the high-power waves with complicated configurations to be measured. The piezotransducer was arranged outside the region of strong electromagnetic waves and pulsed hydrodynamic perturbations; this arrangement eliminated electric interferences and prevented the transducer from mechanical damage.

It is usually assumed that an electric explosion gives rise to a cylindrical acoustic shock wave in the space surrounding the conductor [3]. However, the wave surface formed under real conditions possesses a more complicated configuration [4]. To the first approximation, this configuration is described as an expanding ellipsoid of revolution. Using preliminary experiments with a single exploding conductor, we established the distribution of the pressure amplitude in the field of a shock wave incident onto a hard chamber wall. The results of these experiments showed evidence of a hydrodynamic perturbation existing in the region outside that determined by the linear dimensions of the exploding conductor. This fact indicates that a reflected wave propagating in both radial and axial directions is formed in addition to the compression wave.

It is evident that the axial component of the pressure wave formed in a bounded volume is influenced by the wave reflected from the hard wall. It must be taken into account that the reflected wave propagates in the axial direction within a perturbed region and, hence, at a greater velocity. With time, the reflected radial component will overtake the axial one [5] and their interaction will result in the formation of an acoustic shock wave propagating along the axis of the explosion chamber.

In the experiments with two serially connected exploding conductors, two identical compression waves of high-pressure were generated in the chamber. The axial components of these waves propagate in the opposite directions. The physical parameters of the pressure wave formed as a result of the interaction of two waves propagating in opposite directions from two
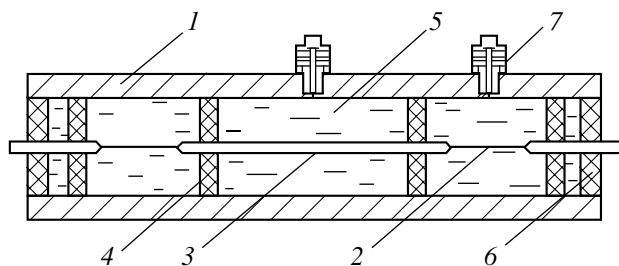
Fig. 1. A schematic diagram of the experimental setup (see the text for explanations).

$p \times 10^8$ Pa
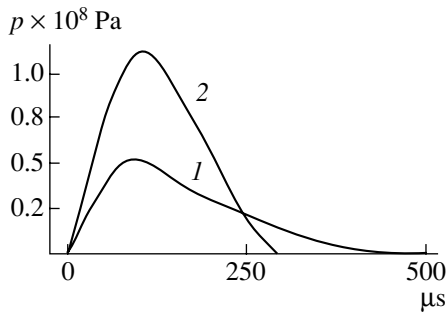
Fig. 2. Time variation of the pressure *p* measured in the cross sections corresponding to the middle of (*1*) an exploding conductor and (*2*) the central electrode.

identical sources were studied in an experimental scheme analogous to that used with a single exploding conductor. The fronts of the two waves propagating in this geometry transform into planes [5]. In a region equidistant from the two sources, the plane waves superimpose to excite a new acoustic shock wave of compression.

In the course of these experiments, a piezotransducer was mounted on the explosion chamber wall in the cross section corresponding either to the middle of an exploding conductor or to the middle of the central electrode. The experimental profile showing time variation of the hydrodynamic pressure in an acoustic shock wave measured in the first case (Fig. 2, curve *1*) exhibits a steep front and exponential decay. This profile agrees with that reported in [3, 6]. The time variation of the pressure of the interacting waves is depicted by curve *2*. In both cases, the waves were generated by the electric explosion of identical conductors under the same initial conditions. The results of our experiments

show a more than twofold increase in the resulting wave amplitude as compared to the initial amplitudes. This observation is consistent with the theory [7] and indicative of the nonlinear character of hydrodynamic processes induced by the electric explosion in the system studied. A technical implementation of the results of this study is described in [8].

REFERENCES

1. N. M. Beskaravaǐnyǐ and V. A. Pozdneev, *Theoretical Foundations of Pulsed Pressure Measurements in Fluid Media* (Naukova Dumka, Kiev, 1981).
2. A. L. Surkaev, V. G. Kul'kov, and G. N. Talyzov, in *Proceedings of the International Scientific and Technical Conference "Advanced Methods of Production and Processing of Constructional Materials and Coatings Increasing Machine Element Durability," Volgograd, 1996*, p. 84.
3. E. V. Krivitskiǐ, *Dynamics of Electric Explosion in Fluids* (Naukova Dumka, Kiev, 1986).
4. V. V. Kucherenko and V. V. Shamko, in *Energy Conversion Processes during Electric Explosion: Collection of Scientific Works* (Naukova Dumka, Kiev, 1988), pp. 90–94.
5. V. V. Selivanov, V. S. Solov'ev, and N. N. Sysoev, *Shock and Detonation Waves. Methods of Research* (Mosk. Gos. Univ., Moscow, 1990).
6. V. M. Demina and A. A. Shkatov, in *Physical Principles of Electrical Explosion: Collection of Scientific Works* (Naukova Dumka, Kiev, 1983), pp. 79–87.
7. M. A. Isakovich, *General Acoustics* (Nauka, Moscow, 1973).
8. G. I. Bryzgalin, A. L. Surkaev, A. E. Godenko, *et al.*, USSR Inventor's Certificate No. 1760677 A1 (1990).

Translated by P. Pozdeev

In vivo Investigation of the Immersion-Liquid-Induced Human Skin Clearing Dynamics

V. V. Tuchin, A. N. Bashkatov, É. A. Genina, Yu. P. Sinichkin, and N. A. Lakodina

Saratov State University, Saratov, Russia
e-mail: tuchin@ns.ssu.runnet.ru
Received January 9, 2001

Abstract—The results of an *in vivo* investigation of human skin clearing caused by the immersion-liquid-induced matching of the refractive indices are reported for the first time. It was established that subcutaneous injections of a glucose solution produce a significant long-term suppression of the light scattering in the skin dermis, which is an important factor ensuring an increase in efficacy of the optical tomography, photodynamic therapy, and photodestruction of deep objects. © *2001 MAIK "Nauka/Interperiodica".*

The possibility of controlling the optical properties of biological tissues is an important factor for the development of optical tomography, photodynamic therapy, and photodestruction methods [1–13]. An effective means of changing the optical properties of biological tissues is based on using osmotically active liquids such as glucose, glycerol, propylene glycol. Below we report for the first time on the results of an *in vivo* investigation of the human skin clearing effect, whereby a long-term suppression of the light scattering in the skin dermis is caused by subcutaneous injections of a glucose solution.

The optical characteristics of the human skin are mostly determined by the properties of the dermis, which accounts for ~95% of the total skin thickness and has a refractive index comparable to that of the epidermis [8, 9]. In the optical transparency interval of the skin (600–1400 nm), the absorption coefficients of both dermis and epidermis amount to less than one-tenth of the corresponding light scattering coefficients.

The results of the previous *in vitro* investigations revealed a number of features in the interaction of osmotically active liquids with biological tissues [1–13]. Introduced into a biological tissue (usually by diffusion through the sample surface), an immersion liquid with a refractive index greater than that of the interstitial and intercellular substances would decrease the difference in refractive indices between the scatterers (collagenic and elastin fibrils, melanin granules, cell membranes, etc. [9, 14]) and their environment. This matching is manifested by optical clearing of the tissue. The matching of refractive indices is also favored by the osmotic migration of water (shrinkage), which increases the concentration of organic substances in the interstitial space and, hence, the refractive index of the interstitial substance. Although the above interactions also affect the tissue layer thickness and the scatterer size and concentration, the immersion-liquid-induced matching

effect dominates and leads to a significant optical clearing of the tissues: the transmission coefficient increases from several times (for the human skin) to several tens of times (for the human sclera) [4–6, 9, 11–13]. For the sclera, the clearing effect begins 8–10 min after immersion, while the skin clearing development requires about one hour.

It was expected that, on the whole, the dynamics of skin clearing *in vivo* would follow the pattern established *in vitro*. However, significant quantitative changes were expected in the time response as determined by the method of immersion liquid introduction (subcutaneous injection) and by the living organism's reaction to the treatment.

A 40% glucose solution was introduced into a volunteer in a volume of 0.1 ml by single subcutaneous injection into the inner side of the forearm. The light reflection spectra in the 400–800 nm range were measured with an optical multichannel analyzer of the LESA-6Med type (BioMed, Russia) linked to a fiber transducer. The transducer, comprising a system of optical fibers, can be represented by an effective system of two fibers (source and detector) with an equivalent distance of $r_{sd} = 2.5$ mm and an average probing depth of $0.35 r_{sd} = 0.9$ mm [9].

Figures 1 and 2 show the reflection spectra and the time variation of the human skin reflectance measured at various light wavelengths. As is seen, the reflection spectra show a scattering background determined by the diffuse reflection of the skin with well-pronounced bands due to the blood optical absorption. Within one hour after injection of the glucose solution, the skin reflection coefficient K decreases on average by a factor of 3.8 and then exhibits a slow increase, which indicates that glucose is eliminated from the observation area and the skin reflectance tends to restore itself to the initial level. Based on the results of *in vitro* measurements and the proposed skin clearing model, we may
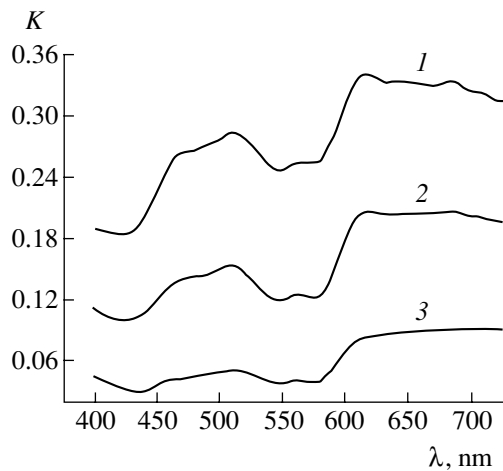
Fig. 1. Optical reflection spectra of human skin measured (*1*) before and (*2, 3*) 23 and 60 min after subcutaneous injection of a 40% glucose solution.
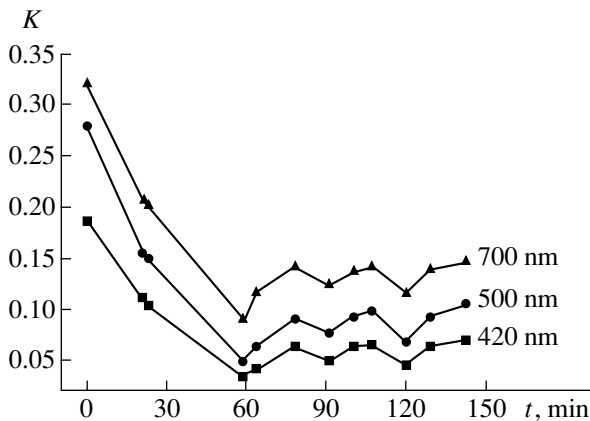
Fig. 2. Time variation of the reflection coefficient K of the human skin measured at various wavelengths after subcutaneous injections of a 40% glucose solution.

suggest that the main contribution to clearing in the first stage (first hour) is due to the refractive index matching between collagenic fibrils of the dermis ($n = 1.46$) and the interfibril space ($n = 1.36$) [9, 14] to which glucose ($n = 1.39$) diffuses. Using a method described in [15], we may estimate the coefficient of glucose diffusion in the human dermis from our experimental data: $D_G = (2.56 \pm 0.13) \times 10^{-6}$ cm^2/s. This value is 3.6 times lower than the coefficient of glucose diffusion in water at 37°C ($D_G \approx 9.2 \times 10^{-6}$ cm^2/s) estimated by extrapolating the data reported in [16]. The difference naturally reflects the character of the skin tissue permeability for glucose.

It should be noted that the skin clearing is retained for several hours, the initial reflectance level restoration being slow and exhibiting oscillations with a period of about 30 min. Using the above glucose diffusion coefficient $D_G = (2.56 \pm 0.13) \times 10^{-6}$ cm^2/s, we may readily estimate the time required for glucose to impregnate a 0.9-mm-thick dermis layer: $\tau = l^2/D_G \approx 53$ min [4, 5].

This is the time of glucose outdiffusion from the region of injection to the epidermis (the time of clearing development). In the stage of the initial reflectance level restoration (clearing removal), the major role belongs to the lateral diffusion in the skin and the downward diffusion. For a significant decrease in the skin clearing, it is necessary that glucose diffuse out of the region sensed by the transducer by a distance of at least $l = (0.5–0.7)r_{sd} = 1.25–1.75$ mm, which requires approximately from 1.7 to 3.3 h in agreement with experiment (Fig. 2).

The oscillatory character of reflectance in the clearing removal stage is related to the complex dynamic character of the process of diffusion in a multicomponent biological tissue. Explaining this behavior would require additional investigation.

REFERENCES

1. M. Hatcher, Opto Laser Eur. Mag. **78**, 37 (2000); http://perl.spie.org/cgi-bin/news.pl?id=1753
2. B. Chance, H. Liu, T. Kitai, and Y. Zhang, Anal. Biochem. **227**, 351 (1995).
3. E. K. Chan, B. Sorg, D. Protsenko, *et al.*, IEEE J. Sel. Top. Quantum Electron. **2** (4), 943 (1996).
4. V. V. Tuchin, I. L. Maksimova, *et al.*, Proc. SPIE **2981**, 120 (1997).
5. V. V. Tuchin, I. L. Maksimova, *et al.*, J. Biomed. Opt. **2** (4), 401 (1997).
6. V. V. Tuchin, Lazernaya Med. **2** (2-3), 5 (1998).
7. V. V. Tuchin, Usp. Fiz. Nauk **167**, 517 (1997) [Phys. Usp. **40**, 495 (1997)].
8. V. V. Tuchin, *Lasers and Fiber Optics in Biomedical Research* (Saratovs. Univ., Saratov, 1998).
9. V. V. Tuchin, *Tissue Optics: Light Scattering Methods and Instruments for Medical Diagnostics* (SPIE Press, Bellingham, 2000), Vol. TT38.
10. G. Vargas, E. K. Chan, *et al.*, Lasers Surg. Med. **24**, 133 (1999).
11. A. N. Bashkatov, V. V. Tuchin, *et al.*, Proc. SPIE **3591**, 311 (1999).
12. A. N. Bashkatov, E. A. Genina, *et al.*, Proc. SPIE **3908**, 266 (2000).
13. A. N. Bashkatov, E. A. Genina, *et al.*, Proc. SPIE **4162**, 182 (2000).
14. J. R. Mourant, T. Fuselier, *et al.*, Appl. Opt. **36** (4), 949 (1997).
15. A. N. Bashkatov, E. A. Genina, *et al.*, Proc. SPIE (2001) (in press).
16. *Physical Quantities. Handbook*, Ed. by I. S. Grigor'ev and E. Z. Meĭlikhov (Énergoizdat, Moscow, 1991).

Translated by P. Pozdeev

Sonoluminescence Generated by the Interaction of Two Ultrasonic Fields with Strongly Different Frequencies

N. V. Dezhkunov

Belarussian State University of Informatics and Radioelectronics, Minsk, Belarus
e-mail: dnv@bsuir.edu.by
Received January 22, 2000

Abstract—The phenomenon of luminescence under the action of ultrasound (sonoluminescence, SL) was studied in a liquid exposed to the field of a high-frequency (HF, 880 kHz) focusing radiator with simultaneous or preliminary action of a low-frequency (LF, 19.9 kHz) ultrasound on the sample. It is shown that a nonadditive increase in the SL intensity takes place for simultaneously operating radiators and is observed for a long time (up to several hours) after switching off the LF source. This is evidence of a long-term aftereffect of the LF ultrasound on the magnitude of SL induced by the HF oscillations. The possible mechanisms of the observed effect are discussed. © 2001 MAIK "Nauka/Interperiodica".

As is known, the efficiency of energy concentration is markedly greater in a single cavitating bubble than in bubbles within a multibubble cavitation region [1–3]. This is manifested, in particular, by higher sonoluminescence (SL) intensities, temperatures, and pressures developed by collapsing bubbles in the former case. For example, the number of photons in every emission event under single-bubble SL conditions reaches 10^5–10^6 [1], whereas the analogous value for a multibubble SL regime does not exceed 10^3 [4, 5]. Estimates of the temperature to which a vapor–gas mixture is heated inside a bubble yield 2000–6000 K for the multibubble SL [2, 3, 5] and up to 30000–50000 K (and even above) for the single-bubble SL [1, 6].

The main reason for this difference is probably the loss of sphericity of the collapsing bubbles, which leads to a decrease in the degree of compression of the vapor–gas mixture and, accordingly, to lower temperatures and pressures developed inside each bubble. Deviations from the spherical bubble shape in a multibubble cavitation region may be caused by the interbubble interactions mediated by shock waves and hydrodynamic forces. These interactions are especially pronounced for the bubbles forming stable structures such as clusters or streamers [7, 8]. The other factors capable of reducing the cavitation activity are the inhomogeneity of the bubble size distribution and effective screening of the inner volume of the cavitation region by peripheral bubbles [9, 10]. As a result, the large (less effective) bubbles absorb and scatter a considerable part of the total acoustic energy, thus decreasing the energy spent for the formation of effective cavitational voids and stored by these voids in the expansion stage.

Below is proposed a new method for increasing the multibubble SL intensity, for which purpose an additional low-frequency (LF) field is superimposed onto

the cavitation region generated by a high-frequency (HF) pulse-modulated sound field.

Figure 1a shows a schematic diagram of the experimental setup. An HF (880 kHz) focusing radiator with a diameter of 40 mm is mounted at the bottom of a cylindrical cell having a diameter of 100 mm and a height of 180 mm. The cell is provided with special windows on a level of the focal spot of the HF radiator, which are used to introduce a light guide connected to a photomultiplier (20 mm in diameter) and a waveguide of an LF radiator. The radiating waveguide edge has a diameter of 15 mm and is located 30 mm aside from the focal spot center of the HF radiator. A hydrophone is mounted 30 mm above the HF radiator focal spot center. The experiments were performed in doubly distilled water at a temperature of $23 \pm 1°C$. An important procedure was the preliminary outgassing of the liquid medium by 15-min ultrasonic treatment, which markedly increased the reproducibility of the results. Upon this treatment, the gas content in the liquid decreased by 20–25% as compared to the saturation level [10, 11] and then changed very slightly in the course of subsequent experiments.

During an experiment, we measured the SL intensity for the cavitation excited by the HF and LF fields separately or jointly and by the HF field upon switching off the LF component. Figure 1b shows a typical hydrophone response H (upper diagram) and photomultiplier response L (lower diagram). In the time interval AB, only the HF radiator is operative and the average multiplier response is $L \approx 17$ mV. Note that, in a slow-sweep record (such as in Fig. 1), a low-intensity SL signal can be masked by background noise pulses; however, these pulses are rather seldom and do not complicate measurements at a high sweep rate. In the time interval BC, both sources are switched off. In the CD

(a)

(b)
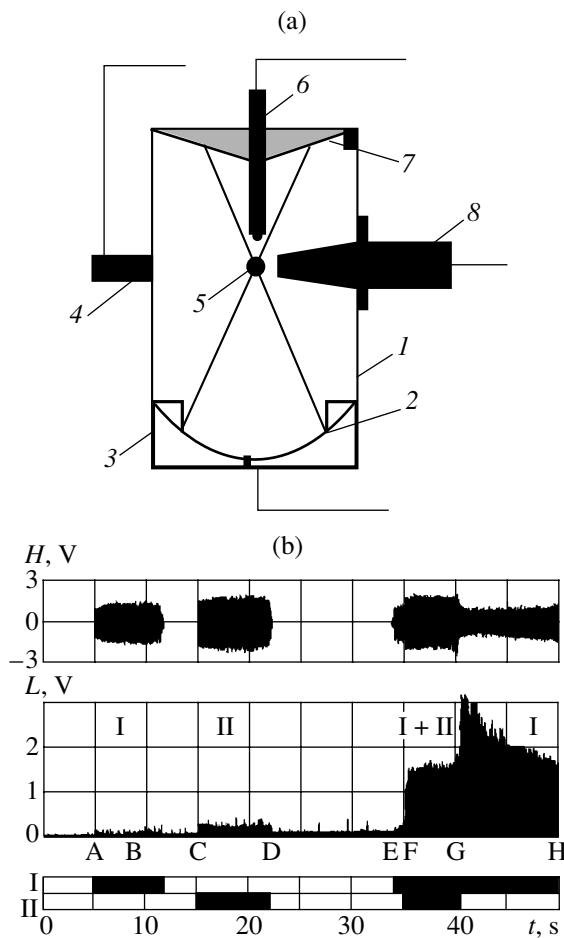
Fig. 1. (a) A schematic diagram of the experimental setup: (*1*) cell case; (*2*) HF (880 kHz) focusing radiator; (*3*) teflon holder; (*4*) photomultiplier tube; (*5*) focal spot of the HF radiator; (*6*) hydrophone; (*7*) sound-absorbing lid; (*8*) LF (19.9 kHz) radiator with a waveguide-concentrator. (b) The results of simultaneous registration of the hydrophone response H (upper diagram) and photomultiplier response L (lower diagram); HF field (I): pulse duration $\tau = 2$ ms, pulse repetition rate $T = 300$ ms; radiator voltage, 135 V; LF field (II): amplitude, 8 μm. Bottom time schedule indicates in black the periods of operation of the HF (I) and LF (II) radiators.

interval, only the LF radiator is operative and the average photomultiplier response is $L = 250{-}270$ mV. In the DE interval, both sources are switched off.

In the EF interval, the HF radiator is set to operate and then the LF source is temporarily switched on (point F) and off (point G) to leave the HF source operating alone again (GH). Therefore, the time interval FG features the SL signal due to the interaction of two ultrasonic fields, and the GH interval reflects SL induced by the HF source after switching off the LF field. The average photomultiplier response in the FG interval is $L \sim 1500$ mV. Thus, the SL induced by the joint action of both radiators is several times greater than a simple sum of the effects of two fields produced separately (nonadditive action). An even more interest-

ing phenomenon is a jump in the SL intensity observed immediately upon switching off the LF field (point G). Here, the SL intensity increases to a much higher level and then gradually decreases in the GH interval to attain a certain limiting value. If the order of switching the field components is reversed (LF followed by HF, which is not depicted in Fig. 1), the second jump is missing and the SL intensity almost instantaneously drops to the initial level (generated by the LF field alone) upon switching off the HF field.

Figure 2 shows the results of the SL intensity measurements in an experiment conducted by a different time schedule. In this case, the LF field was initially switched on for a short period of time and then, with a delay Δt, the HF field was switched on. The LF and HF radiators operated in the same regimes as in the experiment illustrated in Fig. 1b. As is seen in Fig. 2, the memory of a stimulating action of the LF field upon the intensity of cavitation induced by the HF field is retained for a rather long time. When the HF radiator is switched on (with a delay Δt) after the LF pretreatment, the SL intensity increases, passes through a maximum L_{max}, and then slowly decreases (Figs. 2a–2d). As the Δt interval is increased, the L_{max} value decreases due to relaxation of a change in the cavitation properties of the liquid induced by the LF field. The total relaxation time (i.e., the cavitation memory scale) in some cases reached several hours. Within this time interval, the liquid returns into the initial state and the SL intensity induced by the HF field is virtually the same as that observed for the HF field acting before the LF field switching.

An evident mechanism of the SL intensity increase during the operation of both radiators consists in increasing the power dissipated in the liquid and in the interference of the fields, which may give rise to greater pressure jumps as compared to those induced by each field acting separately. This mechanism may lead to an increase in the frequency of cavitation events per unit time and, hence, to the corresponding growth in the SL intensity. Besides, the interference of two fields with the frequencies f_1 and f_2 in a bubbled liquid leads to the appearance of combination frequencies $f_1 + f_2$ and $f_1 - f_2$ and the combination frequencies of harmonics nf_1 and nf_2. Because of this significant broadening of the spectral composition of the resulting field, the cavitation process may involve bubbles with a much greater range of dimensions.

An alternative mechanism is as follows. The LF field can be considered as quasistatic with respect to the HF field. In the halfwave of rarefaction produced by the LF field, the resulting pressure (quasistatic with respect to the HF field) decreases and the size of the cavitation nuclei increases. This leads to an increase in the number of bubbles exhibiting cavitation under the action of the HF field and, eventually, in the SL intensity. In the LF halfwave of compression, an increase in the static pressure favors the more rapid collapse of these bub-
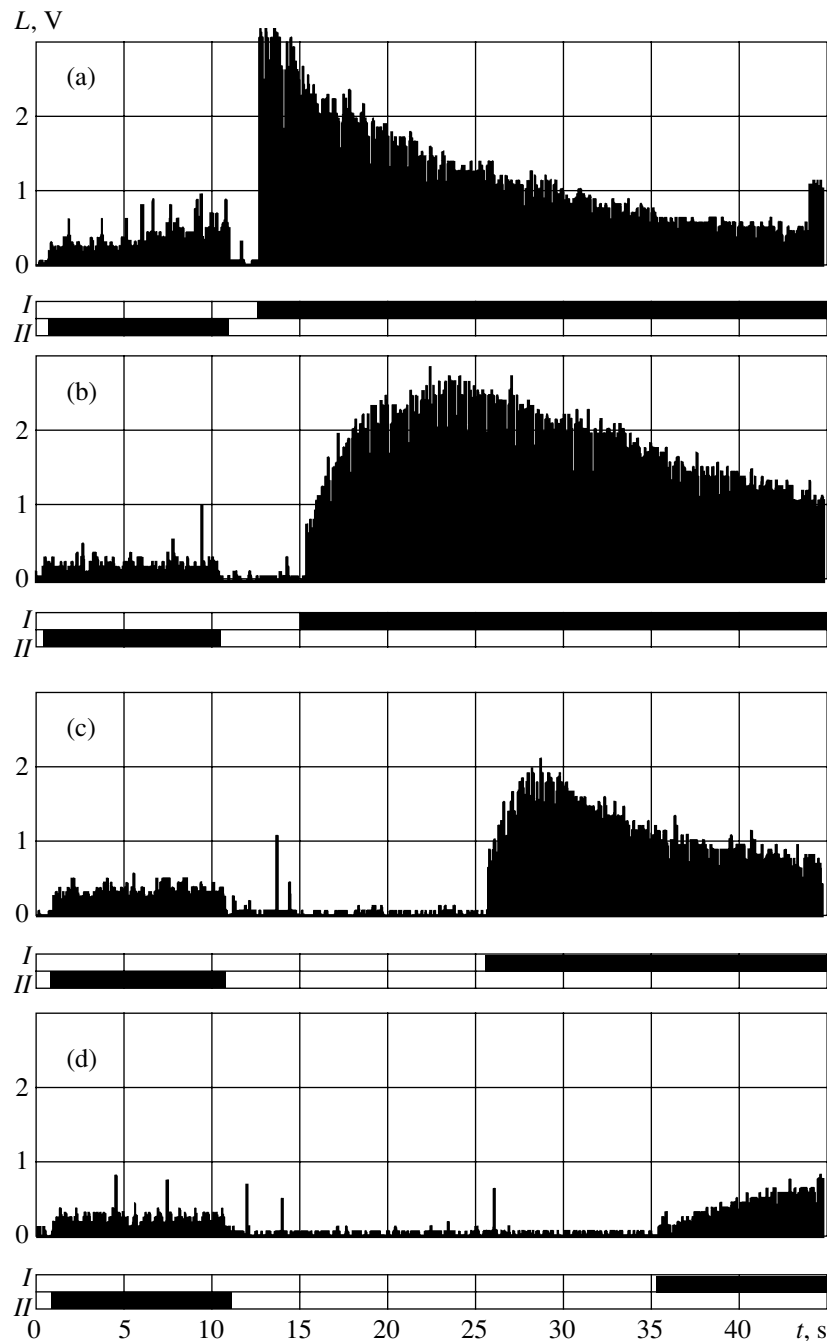
Fig. 2. Diagrams of the photomultiplier response L versus time t for the LF (II) and HF (I) radiators separately switched with delay $\Delta t = 1.5$ (a), 5 (b), 15 (c), 25 s (d). Other parameters as indicated in the caption to Fig. 1.

bles. However, the data presented in Figs. 1 and 2 show that these mechanisms are not dominating. Indeed, their manifestations are possible only provided that both fields are switched on. In the experiment, on the contrary, the SL intensity exhibits additional growth at the moment of switching off the LF field. Moreover, these mechanisms cannot explain the experimentally observed long-term aftereffect of the LF field (Fig. 2).

A possible mechanism of the SL intensity amplification consists in the generation of unstable cavitation nuclei due to collapse of the cavitating bubbles. Indeed, according to [12], a cavitating bubble may decay with the formation of a large number of fine fragments (up to 40) with dimensions much smaller than the initial nucleus size. Therefore, the fragments of bubbles collapsing under the action of an LF field component can serve as critical nuclei for cavitation in the HF field. As a result the number of cavitating bubbles significantly increases and the SL intensity accordingly grows. After switching off the LF field, the nuclei dissolve and

decrease in size, which leads to a decrease in the SL intensity.

Thus, stimulation of the HF-field-induced cavitation by a short- time preliminary LF field application or by a simultaneously operating LF ultrasonic field allows the SL intensity to be significantly increased. Additional experiments are planned in order to elucidate the role of the aforementioned mechanisms in the phenomenon of SL enhancement, to establish the reasons for the SL intensity jump at the instant of the LF field switching off, and to explain the slow relaxation of the cavitation properties of the liquid medium.

REFERENCES

1. R. Hiller, S. J. Putterman, and B. P. Barber, Phys. Rev. Lett. **69** (8), 1182 (1992).
2. T. J. Matula, R. A. Roy, and P. D. Mourad, Phys. Rev. Lett. **75** (13), 2602 (1995).
3. K. S. Suslick, McNamara III, and Y. Didenko, in *Sonochemistry and Sonoluminescence*, Ed. by L. A. Crum *et al.* (Kluwer, Boston, 1998), NATO ASI Ser., Ser. C, Vol. 524.
4. G. J. Gimenez, J. Acoust. Soc. Am. **71** (4), 839 (1982).
5. Yu. T. Didenko, D. N. Nastich, S. P. Pugach, *et al.*, Ultrasonics **32**, 71 (1994).
6. L. S. Bernstein and M. R. Zakin, J. Phys. Chem. **99**, 14 619 (1995).
7. U. Parlitz, S. Luther, R. Mettin, *et al.*, Philos. Trans. R. Soc. London, Ser. A **357**, 313 (1999).
8. A. A. Doinikov and S. T. Zavtrak, J. Acoust. Soc. Am. **99**, 3849 (1996).
9. T. G. Leighton, *The Acoustic Bubble* (Academic, London, 1996).
10. N. V. Dezhkunov, A. Francescutto, P. Ciuti, *et al.*, Ultrason. Sonochem. **7**, 19 (2000).
11. N. V. Dezhkunov, Izv. Akad. Nauk Belarusi, Ser. Fiz.-Tekh. Nauk, No. 1, 109 (1998).
12. M. G. Sirotyuk, in *Powerful Ultrasonic Fields*, Ed. by L. D. Rozenberg (Nauka, Moscow, 1968), pp. 167–220.

Translated by P. Pozdeev

Nitrogen Diffusion in a Subsurface Region of Ion-Implanted Molybdenum

E. Yu. Zamalin and O. B. Bodnar'

State Academy of Instrument Building and Informatics, Moscow, Russia
e-mail: ecofam_036@e-mails.ru
Received December 8, 2000; in final form, February 7, 2001

Abstract—The dynamics of variation of the surface concentration of nitrogen in an ion-doped (100)-oriented single crystal Mo foil was studied by Auger electron spectroscopy and secondary-ion mass spectrometry techniques. The samples were implanted with nitrogen ions at an energy of 50 or 100 keV to a dose of 5×10^{17} cm^{-2} and then annealed at 800–900°C. The diffusion coefficient of nitrogen, estimated by the time of appearance of the maximum nitrogen concentration on the sample surface, is 7–9 orders of magnitude lower than the value for a solid solution of nitrogen in molybdenum. On the other hand, this estimate is 3–5 orders of magnitude higher than the self-diffusion coefficient of molybdenum. It is suggested that a "supersaturated" solid solution of nitrogen is formed in ion-implanted molybdenum, in which the excess (over the solubility limit) nitrogen is deposited at the radiation defects and migrates with these defects in the course of the diffusion annealing. © 2001 MAIK "Nauka/Interperiodica".

Previously [1–4], we developed a method for the investigation of diffusion characteristics in a subsurface region of ion-implanted materials. The approach is based on creating a dome-shaped impurity concentration profile in the sample and monitoring the kinetics of the surface impurity concentration in the course of diffusion annealing. The study of ion-doped silicon by this method revealed several diffusion flows characterized by different diffusion coefficients and allowed the radiation defects of at least one type to be identified [4].

The purpose of this study was to apply the developed method of investigation of the diffusion characteristics to metals, in particular, to molybdenum.

We have studied a single crystal molybdenum foil oriented in the (100) plane, which was annealed at 2000°C and possessed an initial dislocation concentration of 10^6 cm^{-2}. The foil was implanted with N$^+$ ions at an energy of 50 or 100 keV to a dose of 5×10^{17} cm^{-2}. The initial profile of implanted nitrogen was determined by secondary-ion mass spectrometry (SIMS) at a constant sample sputtering rate of 70 Å/min. The ion-doped samples were annealed in the chamber of an electron spectrometer. The surface concentration of nitrogen was measured *in situ* in the course of annealing by the Auger electron spectroscopy (AES); the Auger electron spectra were taken every 5 min.

Figure 1 presents the experimental curves showing time variation of the surface concentration of nitrogen measured in the course of annealing at four different temperatures. The primary Auger electron spectra were processed by interpolation with polynomials using a Machtcad 7 program [5] with an allowance for a 20% instrumental error of the AES measurements.

All the kinetic curves show two peaks of the surface nitrogen concentration (indicated by arrows in Fig. 1). This is probably related to the presence of an additional nitrogen concentration maximum in the initial depth–concentration profile (Fig. 2) [6]. An additional near-surface peak was also observed upon the implantation of nitrogen into iron [7]. The formation of the near-surface nitrogen concentration peaks was explained [6–8] in terms of the radiation-stimulated diffusion under conditions of a significant target heating during the ion bombardment.

The coefficient of nitrogen diffusion in the subsurface region of molybdenum was estimated using the method described in [2]. Parameters of the initial
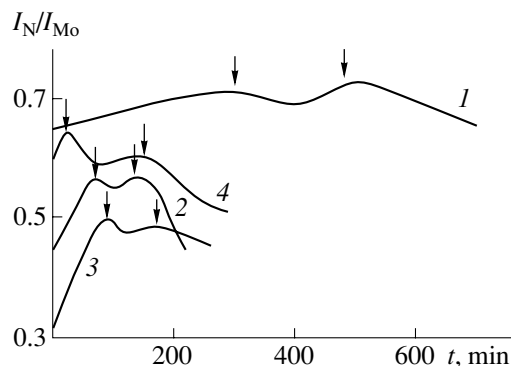
Fig. 1. Time variation of the relative surface concentration of nitrogen in the course of diffusion annealing at various temperatures T = 1073 (*1*), 1123 (*2*), 1148 (*3*), and 1173 K (*4*) for molybdenum samples implanted with nitrogen ions at an energy of E = 50 (*1, 2*) and 100 keV (*3, 4*) to the same dose of 5×10^{17} cm^{-2}.

Implanted nitrogen diffusion in molybdenum targets annealed at various temperatures

T, K	1073	1183	1148	1173	Ref.
D_1, cm/s^2	2.7×10^{-17}	2.1×10^{-16}	7.5×10^{-16}	2.9×10^{-15}	
D_2, cm/s^2	1.1×10^{-16}	8.7×10^{-16}	2.3×10^{-15}	6.2×10^{-15}	
D_N, cm/s^2	2.7×10^{-9}	9.3×10^{-9}	1.1×10^{-8}	1.7×10^{-8}	[12]
	9.5×10^{-8}	1.7×10^{-7}	6.2×10^{-7}		[13]
D_{Mo}, cm/s^2	1.6×10^{-20}	1.1×10^{-19}	3.2×10^{-19}	6.3×10^{-19}	[11]

implant distribution (the average projected range and average range dispersion) for the main and additional (near-surface) peaks were determined using the implantation depth–concentration profiles (Fig. 2). The main peak parameters virtually coincide with the values reported in [9]. Data on the diffusion coefficient of nitrogen (D_1, D_2) calculated for both peaks by the formula derived in [2] are summarized in the table. For comparison, the table presents the diffusion coefficients (D_N) of nitrogen in molybdenum taken from [10] and the molybdenum self-diffusion coefficients (D_{Mo}) determined by interpolating the data from [11] to low temperatures.

A remarkable feature of the diffusion coefficients estimated as described above is their extremely low values, which are 6–9 orders of magnitude lower than the volume diffusion coefficients for a solid solution of nitrogen in molybdenum; on the other hand, the values obtained are 3–5 orders of magnitude higher than the self-diffusion coefficients of molybdenum.
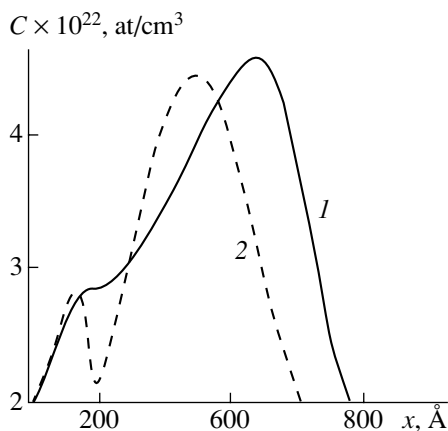
The limiting solubility of nitrogen in molybdenum is very small (less than 0.1 at. % at temperatures below 2000 K) [10]. At the same time, the implanted dose

provides for a maximum nitrogen concentration above 30 at. % corresponding to the initial implant distribution peak, which is sufficient for the Mo_2N nitride formation. We have studied the phase composition of unannealed and annealed implanted molybdenum samples by X-ray diffraction on a DRON-2 diffractometer. The X-ray diffraction patterns exhibited no peaks corresponding to nitride phases. In addition, we measured the Auger electron spectra of the unannealed and annealed (1073 K, 1 h) samples ion-sputtered to a depth of 800 Å. The spectra revealed no chemical shift of the nitrogen peaks, which indicated the absence of chemically bound nitrogen in the samples. The Mo_2N nitride formation in the sample volume, even in the presence of overstoichiometric nitrogen, is apparently hindered by a considerable lattice mismatch between Mo and Mo_2N (the lattice parameters being 3.146 and 4.16 Å, respectively). In addition, according to [10], molybdenum nitrides are thermodynamically unstable and begin to decompose at temperatures above 1023 K.

Thus, we may suggest that the main fraction of implanted nitrogen occurs during annealing in the state of a "supersaturated" solid solution. In the presence of a large concentration of radiation defects (forming pile-ups of interstitial atoms and small dislocation loops [14]) in the molybdenum crystal matrix, implanted nitrogen atoms probably tend to localize on these centers, decreasing the mobility of defects. Therefore, the experimentally measured nitrogen diffusion coefficient essentially characterizes the mobility of radiation defects blocked by the implanted impurity atoms. From this standpoint, the diffusion coefficients obtained, which are significantly lower than those for a solid solution and considerably higher than the molybdenum self-diffusion coefficients, seem to be quite reasonable.

Fig. 2. The initial implantation depth–concentration profiles determined by SIMS for molybdenum samples implanted with nitrogen ions under different conditions: (*1*) ion beam energy $E = 100$ keV, beam current density $J = 20$ μA/cm^2, total ion dose $Q = 5 \times 10^{17}$ cm^{-2}; (*2*) $E = 50$ keV, $J = 10$ μA/cm^2, same $Q = 5 \times 10^{17}$ cm^{-2} (data from [6]).

REFERENCES

1. E. Yu. Zamalin, Poverkhnost, No. 6, 116 (1995).

2. O. B. Bodnar', E. Yu. Zamalin, and A. K. Mambetov, Poverkhnost, Nos. 7-8, 64 (1995).

3. E. Yu. Zamalin, O. B. Bodnar', and T. V. Popova, Poverkhnost, Nos. 7-8, 68 (1995).

4. E. Yu. Zamalin, O. B. Bodnar', and T. V. Popova, Poverkhnost, No. 8, 62 (1999).

5. *Mathcad: User's Guide Mathcad 6.0, Mathcad PLUS 6.0* (MathSoft Inc., Cambridge, 1991–1995; Filin, Moscow, 1996).

6. B. V. Ushakov, N. V. Alov, S. A. Kozikov, *et al.*, Fiz. Khim. Obrab. Mater., No. 5, 38 (1989).

7. J. Zemek and J. Kral, Czech. J. Phys. **37**, 954 (1987).

8. F. Bodart, G. Tericagne, and M. Piette, Mater. Sci. Eng. **90**, 111 (1987).

9. A. F. Burenkov, F. F. Komarov, M. A. Kumakhov, *et al.*, Preprint No. 3592/11, Inst. At. Énerg. (Kurchatov Institute of Atomic Energy, Moscow, 1982).

10. S. S. Kiparisov and Yu. V. Levinskiĭ, *Nitration of Refractory Metals* (Metallurgiya, Moscow, 1972).

11. B. S. Bokshteĭn, *Diffusion in Metals* (Metallurgiya, Moscow, 1978).

12. R. Francfelder, J. Chem. Phys. **48**, 3966 (1968).

13. M. Ying-Liang and Jin-Yihs, Acta Metall. Sin. **7**, 68 (1964).

14. M. W. Thompson, *Defects and Radiation Damage in Metals* (Cambridge Univ. Press, Cambridge, 1969; Mir, Moscow, 1971).

Translated by P. Pozdeev

Laser-Controlled Synthesis
of Nickel–Aluminum Intermetallic Compounds

A. V. Kamashev, A. S. Panin, A. L. Petrov, and I. V. Shishkovskiĭ

Lebedev Physical Institute (Samara Branch), Russian Academy of Sciences, Samara, Russia
Received January 26, 2001

Abstract—Laser-initiated self-propagating high-temperature synthesis (SHS) in a disperse Ni–Al powder composition was studied. The X-ray diffraction measurements reveal the presence of nickel–aluminum intermetallic phases, the relative content of which depends on the regime of laser action. The regimes making possible a laser-controlled SHS of Ni–Al intermetallic compounds are considered. © *2001 MAIK "Nauka/Interperiodica".*

Intermetallic compounds of the Ni–Al system are promising materials for the synthesis of heat- and radiation-resistant coatings. For example, high heat-resistant properties are offered by nickel–aluminum compounds of the NiAl and Ni_3Al types, which can withstand even the action of high-temperature gas flows.

A traditional method of obtaining nickel–aluminum intermetallic compounds consists in self-propagating high-temperature synthesis (SHS). A highly promising method is offered by the selective laser sintering (SLS) process [1], which provides for a waste-free fabrication of three-dimensional articles of preset configurations. This method is highly advantageous from a technological standpoint, because the process can be completely automated, requires no specially prepared molds and attachments, and can proceed directly from a design loaded into computer memory. The SLS technology involves several techniques well known in the conventional powder metallurgy and laser technology processes. At the same time, there are certain specific features related to the selective laser action upon local regions of the initial powder layers [2].

It is well known that the combined SHS–SLS processes are difficult to control [5]. The SHS reaction onset may either outstrip or lag behind the sintering process, which would result in premature or incomplete burning of the initial components. For this reason, the main problem in the laser synthesis of Ni–Al intermetallic compounds is to optimize the regime of laser action to provide for a dynamic equilibrium between SHS and SLS processes.

Previous investigations of the laser-initiated SHS process in the Ni–Al system [3–5], performed on simple article configurations, led to the first successful synthesis of a Ni–Al intermetallic compound and allowed a semiqualitative theoretical model to be developed. The purpose of this study was to obtain the Ni–Al intermetallic compounds by SHS in the SLS regime. The main point was to establish the laser action regimes in

which the SHS would be controlled by the laser irradiation dose.

The metal powder reactivity was reduced by supplying an inert gas (Ar) to the reaction zone. The powder composition was selected taking into account the stoichiometry of the target compounds. The powder consisted of metal particles with dimensions below 63 μm. The experiments were performed with a laser setup of the Kvant-60 type operating in a continuous mode with variable output power P (7–24 W) and laser beam scanning velocity v (12–60 mm/s).

The phase composition of the synthesized monolayers were studied by X-ray diffraction on a DRON-3 diffractometer using $CuK_{\alpha1}$ radiation. The analysis showed that the sample contained mostly the Ni_2Al_3 and Ni_3Al phases in various proportions, depending on the laser action regime. An analysis of the X-ray diffraction patterns showed that the laser-controlled SHS process led to the formation of only the Ni_3Al interme-
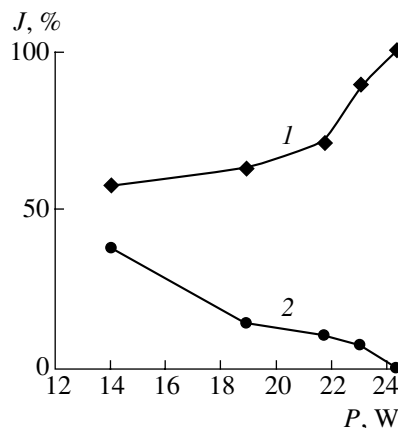
Fig. 1. Plots of the relative intensity J of the diffraction lines of intermetallic phases versus laser power W (for a laser beam scanning velocity of $v = 12$ mm/s): (*1*) Ni_3Al; (*2*) Ni_2Al_3.
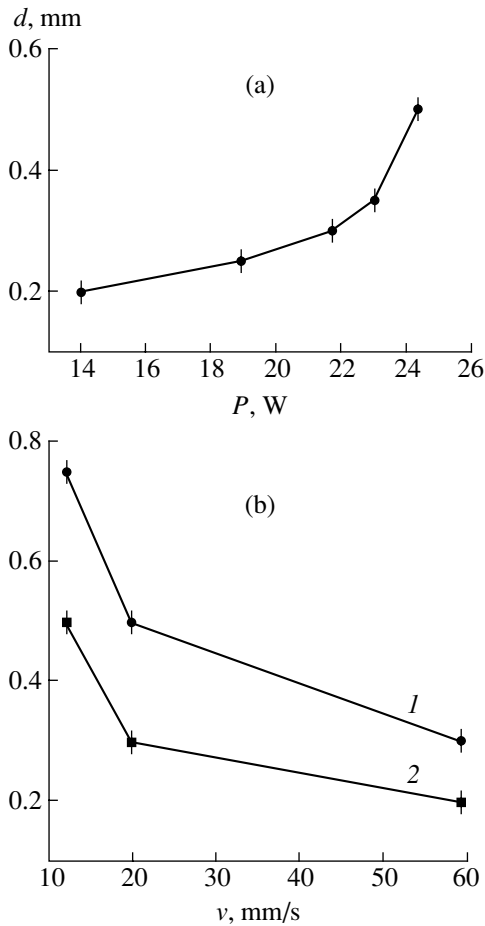
Fig. 2. Plots of the intermetallic phase particle size *d* versus (a) laser power *P* (for $v = 12$ mm/s) and (b) laser beam scanning velocity *v* (for $P = 24$ W) at the (*1*) center and (*2*) periphery of the sample.

results in the SLS process "breakdown" leading to a thermal explosion development. This experimental observation is consistent with theoretical estimates obtained in [5].

The surface morphology of the laser-sintered articles was studied by optical metallography techniques. As seen from the data of Fig. 2, the intermetallic particle size grows in a regular manner with increasing laser power and decreasing laser beam scanning velocity. This behavior is explained by the coagulation of the nucleated particles under conditions of increased intensity or duration of the laser action.

Thus, we have demonstrated the possibility of obtaining intermetallic phases in a Ni–Al powder system processed in the laser-controlled SHS regime, which is confirmed by the X-ray diffraction data. The intermetallic phase particle size exhibits regular growth with increasing laser power and decreasing laser beam scanning velocity. Optimum conditions for the synthesis of the Ni_3Al intermetallic compound using the combined SHS–SLS process are $P = 24$ W, $v = 59$ cm/s and $P = 22$ W, $v = 12$ cm/s. The former regime provides for a shorter process time and ensures the absence of intermediate phases at a sufficiently large thickness of the sintered material; the latter regime ensures a homogeneous surface of the article and a small degree of particle coagulation in the sintered material.

tallic phase, whereas a NiAl phase could not be obtained under the laser action regimes possible in our experiments. This is apparently related to the fact that the SHS synthesis of NiAl in the system studied begins later than the formation of Ni_3Al [3, 4] and is accompanied by the evolution of a large amount of heat, which

REFERENCES

1. D. M. Gureev, A. L. Petrov, and I. V. Shishkovskiĭ, Fiz. Khim. Obrab. Mater., No. 6, 92 (1997).

2. I. V. Shishkovskiĭ, V. I. Shcherbakov, and P. I. Ivanov, Mekh. Kompoz. Mater. Konstr. **5** (2), 29 (1999).

3. O. V. Lapshin and V. E. Ovcharenko, Fiz. Goreniya Vzryva **32** (2), 46 (1996).

4. O. V. Lapshin and V. E. Ovcharenko, Fiz. Goreniya Vzryva **32** (3), 68 (1996).

5. I. V. Shishkovskiĭ, A. G. Makarenko, and A. L. Petrov, Fiz. Goreniya Vzryva **35** (2), 59 (1999).

Translated by P. Pozdeev

The Effect of Annealing on the Photoacoustic and Photothermal Response of Al₂O₃–SiC–TiC Ceramics with Internal Stresses

K. L. Muratikov, A. L. Glazov, V. I. Nikolaev, D. N. Rose, and D. E. Dumar

Ioffe Physicotechnical Institute, Russian Academy of Sciences, St. Petersburg, 194021 Russia

Received February 8, 2001

Abstract—The Vickers indentation zones in Al_2O_3–SiC–TiC ceramics were studied by scanning laser photodeflection and photoacoustic microscopy. The method of photoacoustic microscopy with piezoelectric detector (PAMPD) is sensitive to the internal stress distribution in the material. The effect of annealing on the PAMPD signal of the Al_2O_3–SiC–TiC ceramics was studied. An increase in the annealing time is accompanied by decrease in the PAMPD response from the vertices of radial cracks. © *2001 MAIK "Nauka/Interperiodica".*

In recent years, photoacoustic and photothermal methods have been widely employed for the diagnostics of defects in the bulk and surface layers of various materials. These methods proved to be effective in detecting cracks, delaminated layers, and foreign inclusions [1]. In addition, some researchers studied the possibility of using the photoacoustic method for detecting internal stresses [2–5]. Most of these investigations were performed with ceramics studied under the Vickers indentation conditions. The results showed significant features in the behavior of the photoacoustic response from regions at the vertices of radial cracks, which are known to feature a considerable concentration of internal stresses.

However, the previous investigations of stresses by the photoacoustic method did not pay attention to the character of the photoacoustic response variation in the presence of additional external factors (temperature variation, loading, etc.) acting upon the object studied. The study of such effects may provide direct evidence for the existence of a relationship between photoacoustic response and internal stresses and ensure a deeper understanding of factors determining this relationship. Within the framework of this approach, the main task of this study was to reveal the character of changes in the photoacoustic response from regions with internal stresses in annealed ceramics, in particular, to determine the variation of this response depending on the annealing time.

In order to solve this task experimentally, we employed a complex approach proposed previously [6], which consists in using a combination of photothermal and photoacoustic techniques providing independent information on the thermal and elastic properties of the objects studied. The photothermal techniques were represented by scanning photodeflection microscopy. The elastic properties of samples were studied by photoacoustic microscopy with a piezoelectric detector.

The experiments were performed on samples of Al_2O_3–SiC–TiC ceramics prepared by hot pressing from a mixture of powdered Al_2O_3 (46.1 vol %), powdered TiC (23.0 vol %), and needle-like SiC crystals (30.9 vol %). The hot pressing was carried out in an inert gas atmosphere at a temperature of 1700–1800°C. The final ceramic samples had a density of 3.915 g/cm³, which amounted to 99% of the theoretical limit calculated using the densities of components. The average TiC grain size was about 5 μm, and the average grain size of the Al_2O_3 matrix was 0.3–1.0 μm. The needle-like SiC crystals reinforcing the ceramic composition had an average length of 25 μm and a diameter of about 0.5 μm.

The residual stress fields were generated in the ceramics by the Vickers indentation method under a load of 98 N. Images of the resulting indentation zone were obtained by scanning the sample in two coordinates at a step of 2.5 μm. The temperature waves and acoustic oscillations were excited by radiation of an Ar laser (LGN-503 type) modulated by an acoustooptical modulator (ML-201 type). During the photodeflection and photoreflection measurements, the response readout was performed using a He–Ne laser (Meles Griot 05–LHP-151).

It should be noted that the system employed for the photothermal and photoacoustic microscopy measurements was used for the scanning optical microscopic observations as well, which allowed optical images the sample surface to be simultaneously studied in the scanning optical microscopy regime. These images were obtained by detecting the reflected radiation of the argon laser.

Figure 1 shows an example of the optical image of an Al_2O_3–SiC–TiC ceramic sample surface indented according to Vickers. On the whole, this image has a structure typical of the brittle materials indented in this mode. At the same time, there is a characteristic feature inherent in the images of Al_2O_3–SiC–TiC ceramics obtained by the scanning laser microscopy: a pronounced spot structure is superimposed onto the pattern typical of the Vickers-indented brittle materials. This property of laser images of the Al_2O_3–SiC–TiC ceramics is related to the strongly different optical properties of various grains in the ceramic structure. Indeed, TiC grains strongly absorb the incident radiation, whereas two other components (Al_2O_3 and SiC) are almost transparent in the visible range.

Figure 2 presents a typical image obtained by photodeflection microscopy (PDM) of the Al_2O_3–SiC–TiC sample surface area near the indentation zone. As is seen, the image (formed by measuring the normal component of the photodeflection response signal) reproduces the structure of the subsurface lateral and radial cracks well. At the same time the image exhibits a structure resembling that of the PDM images obtained in our previous study of the silicon nitride ceramics [6, 7]. In the range of the excitation modulation frequencies employed, the lengths of the temperature waves in the Al_2O_3–SiC–TiC ceramics studied markedly exceeded the grain dimensions. For this reason, the spot structure characteristic of the optical images is virtually absent in the PDM images. It should be also noted that PDM images exhibit no features in the vicinity of vertices of the radial cracks, where strong internal stresses are concentrated. Thus, the results obtained by PDM for the Al_2O_3–SiC–TiC ceramics generally coincide with the data for silicon nitride ceramics in which the internal stresses do not affect the behavior of the photodeflection signal [6, 7].

In the experiments with Al_2O_3–SiC–TiC ceramics, this conclusion was additionally confirmed by the results of investigation of the effect of annealing on the photodeflection response. For this purpose, we have measured the PDM images of indentation sites after annealing the samples at 800°C for 8, 16, and 24 h. These experiments did not reveal any significant influence of annealing on the PDM images of the sample surface near the Vickers indentation.

Figure 3 shows an image of the sample surface near the same indentation zone as in Figs. 1 and 2, which was obtained by photoacoustic microscopy with a piezoelectric detector (PAMPD). The most characteristic feature of this image is the presence of bright spots at the vertices of radial cracks, which are indicative of a strong increase in intensity of the photoacoustic signal. Previously, analogous features were reported for the images of Vickers indentations obtained by the method of electron-acoustic microscopy [2]. We also observed this phenomenon in the photoacoustic study of silicon nitride ceramics [6–11] and established that
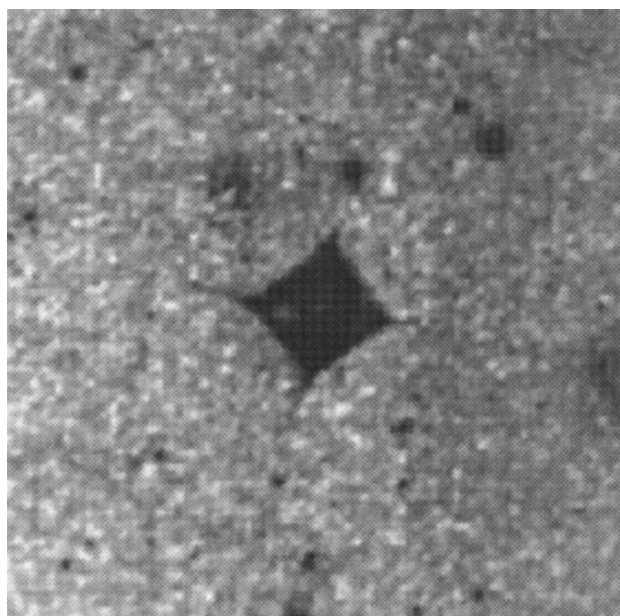
Fig. 1. A scanning optical microscopy image of the surface of Al_2O_3–SiC–TiC ceramics indented according to Vickers (imaged area size, 400×400 μm^2).

Fig. 2. A scanning photodeflection microscopy image (normal component amplitude) of the same surface region of Al_2O_3–SiC– TiC ceramics as in Fig. 1 (the exciting laser radiation modulated at a frequency of 1.4 kHz).

the bright regions at the radial crack vertices correspond to the regions of residual stress accumulation. The absence of analogous features in the PDM images (Fig. 2) allows us to conclude that (i) the internal stresses in Al_2O_3–SiC–TiC ceramics do not affect the
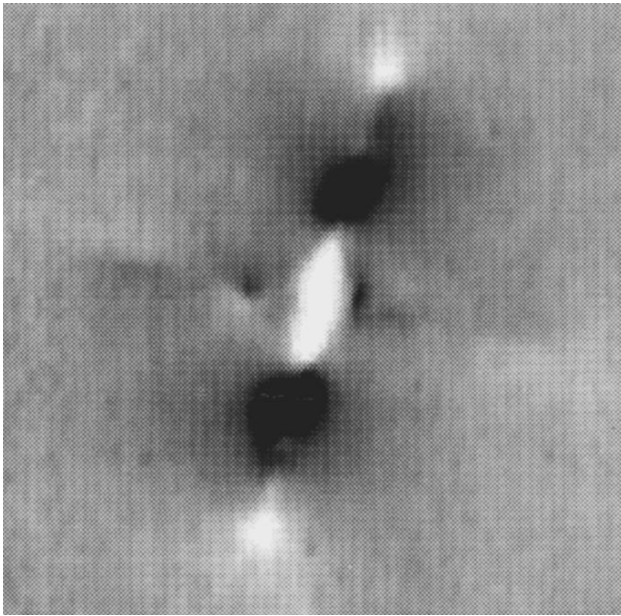
Fig. 3. A photoacoustic microscopy image of the same surface region of Al_2O_3–SiC–TiC ceramics as in Figs. 1 and 2 (the exciting radiation modulated at a frequency of 142 kHz).
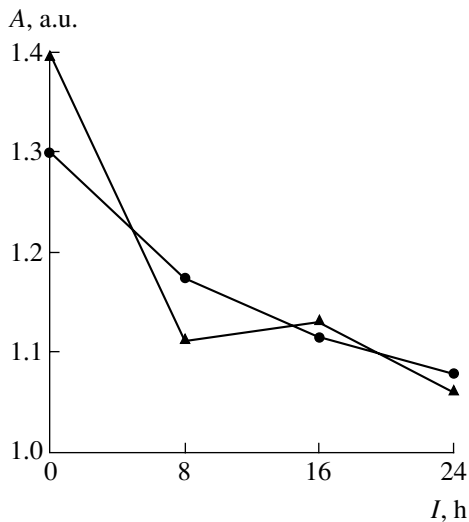
Fig. 4. The plots of maximum photoacoustic signal intensity A (normalized to the average photoacoustic response far from indentation) versus sample annealing time t for two radial cracks in the same Al_2O_3–SiC–TiC ceramic sample.

thermal properties of the material and (ii) the PAMPD sensitivity to the internal stresses is determined mostly by the effect of these stresses on the elastic properties and thermal expansion coefficient. Note that an analogous situation was observed in silicon nitride ceramics [6–11].

To more profoundly elucidate the relationship between photoacoustic response and internal stresses, we studied variation of the PAMPD response with the annealing time. Figure 4 shows the plots of maximum

PAMPD signal intensity (normalized to the average photoacoustic response) for two radial cracks in the same sample. After each annealing at 800°C, the sample temperature was decreased at a sufficiently slow rate (about 10°C/min) in order to minimize the effect of thermal stresses on the crack growth. However, the regions of material in the vicinity of crack vertices occur in a significantly nonequilibrium thermodynamic state [12], so that even weak thermal stresses can affect the crack growth. This circumstance probably accounts for some increase in the photoacoustic response signal observed after a 16-h annealing at one of the radial crack vertices. Nevertheless, Fig. 4 clearly reveals a general tendency of the PAMPD signal to decrease with increasing annealing time. The experimental data on the photoacoustic response variation in the course of annealing of the Al_2O_3–SiC–TiC ceramics are well consistent with the commonly accepted opinion that annealing favors a decrease in the level of internal stresses [13].

Thus, the experimental results showed a high sensitivity of the PAMPD response with respect to internal stresses in Al_2O_3–SiC–TiC ceramics. Together with the results of our previous experiments on silicon nitride ceramics [6–11], these data confirm the conclusion that the method of photoacoustic piezoelectric measurements can be used for the investigation of internal stresses in solids. The observed decrease in intensity of the PAMPD signal from the radial crack vertices with increasing annealing time can be considered as evidence for a direct relationship between the photoacoustic piezoelectric signal and the level of internal stresses. The results of the photodeflection signal measurements in the Al_2O_3–SiC–TiC ceramics showed that (similarly to the case of silicon nitride ceramics) the relationship between photoacoustic response and internal stresses is not related to the effect of internal stresses on the thermal properties of samples.

REFERENCES

1. A. Rosencwaig, in *Progress in Photothermal and Photoacoustic Science and Technology* (Prentice-Hall, Englewood Cliffs, 1994), Vol. 2, pp. 1–23.

2. J. H. Cantrell, M. Qian, M. V. Ravichandran, and K. W. Knowles, Appl. Phys. Lett. **57** (18), 1870 (1990).

3. H. Zhang, S. Gissinger, G. Weides, and U. Netzelmann, J. Phys. IV **4**, C7-603 (1994).

4. R. M. Burbelo and M. K. Zhabitenko, in *Progress in Natural Science* (Taylor and Francis, London, 1996), Suppl. Vol. 6, pp. 720–723.

5. F. Jiang, S. Kojima, B. Zhang, and Q. Yin, Jpn. J. Appl. Phys., Part 1 **37** (5B), 3128 (1998).

6. K. L. Muratikov, A. L. Glazov, D. N. Rose, *et al.*, Pis'ma Zh. Tekh. Fiz. **23** (3), 44 (1997) [Tech. Phys. Lett. **23**, 188 (1997)].

7. K. L. Muratikov, A. L. Glazov, D. N. Rose, and J. E. Dumar, Pis'ma Zh. Tekh. Fiz. **24** (21), 40 (1998) [Tech. Phys. Lett. **24**, 846 (1998)].

8. K. L. Muratikov, A. L. Glazov, D. N. Rose, and J. E. Dumar, in *Proceedings of the 10th International Conference "Photoacoustic and Photothermal Phenomena," 10 ICPPP, Rome, 1998*, AIP Conf. Proc. **463**, 187 (1999).

9. K. L. Muratikov, A. L. Glazov, D. N. Rose, and J. E. Dumar, in *Proceedings of the 3rd International Congress on Thermal Stresses, "Thermal Stresses'99," Cracow, 1999*, p. 669.

10. K. L. Muratikov and A. L. Glazov, Zh. Tekh. Fiz. **70** (8), 69 (2000) [Tech. Phys. **45**, 1025 (2000)].

11. K. L. Muratikov, A. L. Glazov, D. N. Rose, and J. E. Dumar, J. Appl. Phys. **88** (5), 2948 (2000).

12. V. S. Ivanova, A. S. Balankin, I. Zh. Bunin, and A. A. Oksogoev, *Synergetics and Fractals in Materials Science* (Nauka, Moscow, 1994).

13. G. N. Chernyshev, A. L. Popov, V. M. Kozintsev, and I. I. Ponomarev, *Residual Stresses in Deformed Solids* (Nauka, Moscow, 1996).

Translated by P. Pozdeev

On the Possibility of Suppressing the Saturation of Photoelectric Amplification of Weak Optical Emission in Semiconductors by Forming Near-Contact Variband Layers

V. A. Kholodnov and A. A. Drugova

ORION Research, Development, and Production Corporation, State Scientific Center of the Russian Federation, Moscow, Russia

Received January 25, 2001

Abstract—It is demonstrated that saturation of the photoelectric amplification coefficient G with increasing voltage V applied to a sample can be suppressed by introducing a variband layer near a current contact to which the minority charge carriers are driven by the electric field. This effect is considered in the case of interband photogeneration and recombination mechanisms operative, for example, in CdHgTe-based materials widely used for detecting weak emission in the wavelength intervals of $\lambda = 8$–12 and 3–5 μm [1]. © *2001 MAIK "Nauka/Interperiodica"*.

As is known [1–6], the photoelectric amplification coefficient $G(V)$ initially grows with increasing voltage V applied to a sample and then usually saturates despite insignificant field-induced charge carrier heating. The saturation effect does not take place only in cases of ambipolar carrier mobility ($\mu = 0$) or completely absent recombination of minority carriers on the current contacts ($x = 0$ and $x = W$, Fig. 1). However, in practice $\mu \neq 0$ and a more or less pronounced recombination of minority carriers on the current contacts always takes place.

Let us consider the most unfavorable case, whereby the rate of recombination on the contacts is so high that the concentrations of nonequilibrium holes $\Delta p(x)$ and electrons $\Delta n(x)$ at the current contacts are zero (the regime of extracting contacts [3–5]):

$$\Delta n(0) = \Delta p(0) = \Delta n(W) = \Delta p(W) = 0. \quad (1)$$

Under conditions (1), the saturation of G with increasing V is most pronounced [1, 2].

The photoinduced electric field strength $E_{ph}(x) = E - E_0$ must satisfy the macroscopic Poisson equation [1, 7–14],

$$\frac{dE_{ph}}{dx} = \frac{4\pi q}{\in}(\Delta p - \Delta n), \quad (2)$$

where E and E_0 are the electric field strengths in an exposed and unexposed sample (in the coordinate system of Fig. 1a, $E_0 \geq 0$), $\in$ is permittivity, and q is the electron charge.

For a weak illumination intensity, we may employ an approximation linear with respect to the specific carrier production rate g. Under the conditions considered,

following the standard quasineutrality approximation [1, 7–14], we obtain

$$\Delta n(x) = \Delta p(x), \quad (3)$$

$$\frac{dI_{ph}^{(p)}}{dx} = q\left(g - \frac{\Delta p}{\tau}\right) = \left(-\frac{dI_{ph}^{(n)}}{dx}\right), \quad (4)$$

$$I_{ph}^{(n)} = q\mu_n(n_e E_{ph} + E_0 \Delta p) + qD_n\frac{d\Delta p}{dx},$$

$$I_{ph}^{(p)} = q\mu_p\{p_e E_{ph} + (E_0 + E_{var})\Delta p\} - qD_p\frac{d\Delta p}{dx}, \quad (5)$$

where $I_{ph}^{(n)}$ and $I_{ph}^{(p)} = I_{ph} - I_{ph}^{(n)}$ are the electron and hole
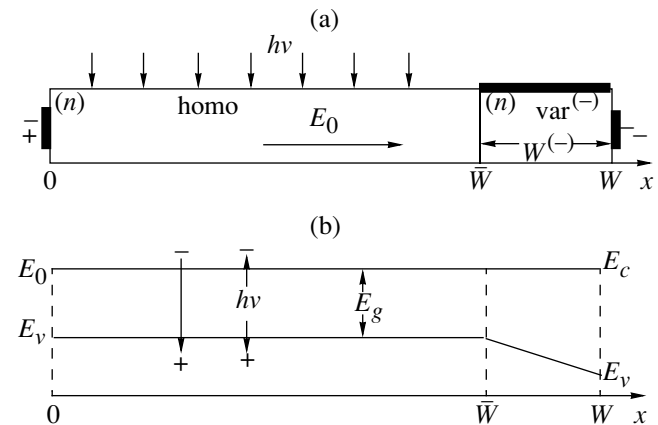
Fig. 1. (a) Schematic diagram showing an n-type sample, illumination direction, and applied voltage polarity; (b) an energy band diagram for the sample with $E_{\text{var}}^{(-)} = -E_0$; E_c and E_v are the conduction band bottom and the valence band top, respectively; $E_g \cong 0.1$ eV is the bandgap.

components of the total photocurrent density I_{ph}; τ is the nonequilibrium carrier lifetime; n_e and p_e are the equilibrium electron and hole densities; μ_n, μ_p and D_n, D_p are the mobilities and diffusion coefficients of electrons and holes, respectively; $E_{var} = -(1/q)(\partial E_g/\partial x)$ is the field strength in the variband layer [15–18]; and E_g is the bandgap width. As is seen from Eq. (2), relationship (3) is valid provided that

$$\frac{\in}{4\pi}\left|\frac{dE_{ph}}{dx}\right| \ll q|\Delta p|, \qquad (6)$$

while relationships (5) are valid in materials with the electron affinity independent of the molar composition (in practice, this condition is satisfied, e.g., in CdHgTe [19, 20]).

As is known, variband structures (featuring gradual spatial variation of the molar composition) are characterized by a much lower density of defects than the analogous heterostructures. For this reason, we will assume that the interface ($x = \overline{W}$, Fig. 1) between homogeneous layer {homo} and variband layer {var$^{(-)}$} contains neither recombination centers nor charged states. In this case, Eqs. (2) and (4) indicate that $I_{ph}^{(n)}(x)$, $I_{ph}^{(p)}(x)$, and $E_{ph}(x)$ are continuous at the $x = \overline{W}$ interface. Then Eq. (5) yields the relationships

$$2E_0\Delta p(\overline{W} - 0) = (2E_0 + E_{var}^{(-)})\Delta p(\overline{W} + 0), \qquad (7)$$

$$2D_p\left(\left.\frac{\partial\Delta p}{\partial x}\right|_{x = W + 0} - \left.\frac{\partial\Delta p}{\partial x}\right|_{x = \overline{W} - 0}\right) \qquad (8)$$
$$= \mu_p E_{var}^{(-)}\Delta p(\overline{W} + 0),$$

which are valid for any bandgap profile $E_g(x)$. We will assume that E_g in the variband layer {var$^{(-)}$} is a linear function of the coordinate x, which implies that $E_{var} \equiv E_{var}^{(-)} = $ const (Fig. 1). As is seen from Eqs. (7) and (8), in this problem formulation (analogous to that studied in [21]) the functions $\Delta p(x)$ and $\partial\Delta p/\partial x$ exhibit discontinuity at $x = \overline{W}$ (attempts at fitting $\Delta p(x)$ as in [21] are incorrect).

Below we assume that the sample studied belongs to a homogeneously doped n-type and restrict the consideration to a zero approximation with respect to a small parameter $\varepsilon \equiv p_e/(bn_e) \ll 1$, where $b = \mu_n/\mu_p$. In this approximation, Eqs. (5) yield

$$E_{ph} = \frac{I_{ph} + q(D_p - D_n)(\partial\Delta p/\partial x)}{q\mu_n n_e}$$
$$- \frac{(b + 1)E_0 + E_{var}}{bn_e}\Delta p, \qquad (9)$$

where E_0 is independent of the coordinate x. Using relationships (1), (4), (5), (7), and (9), we may readily derive approximate expressions for the distribution $\Delta p(x)$ in a sample with a uniformly illuminated homogeneous layer (Fig. 1). Assuming for simplicity that $\mu_{n,p}$, $D_{n,p}$, and τ values are independent of x, we obtain for the homogeneous layer ($0 \le x < \overline{W}$)

$$\Delta p(x) = \Delta\bar{p}(x) \equiv \left\{1 + \frac{\exp(\bar{x}_1 - \bar{w}_1) - \exp(\bar{w}_2 - \bar{x}_2)}{\exp(\bar{w}_2) - \exp(-\bar{w}_1)}\right\}g\tau$$
$$+ \frac{\exp(\bar{x}_1) - \exp(-\bar{x}_2)}{\exp(\bar{w}_1) - \exp(-\bar{w}_2)}\{\Delta p(\overline{W} - 0) - g\tau\}, \qquad (10)$$

where

$$\bar{x}_{1,2} \equiv x/\overline{L}_{1,2}, \quad \bar{w}_{1,2} \equiv \overline{W}/\overline{L}_{1,2},$$
$$\overline{L}_{1,2} = L_p\frac{\bar{r}}{\sqrt{1 + \bar{r}^2} \pm 1} \qquad (11)$$
$$\bar{r} = 2\frac{L_p}{\bar{d}_p}, \quad L_p = \sqrt{D_p\tau}, \quad \bar{d}_p = \mu_p E_0\tau.$$

By the same token, in the variband layer {var$^{(-)}$} ($\overline{W} < x \le W \equiv \overline{W} + W^{(-)}$):

$$\Delta p(x) = \Delta p^{(-)}(x) \equiv \frac{2E_0}{2E_0 + E_{var}^{(-)}}$$
$$\times \frac{\exp(x_1^{(-)} - \tilde{w}_1^{(-)}) - \exp(\tilde{w}_2^{(-)} - x_2^{(-)})}{\exp(-w_1^{(-)}) - \exp(w_2^{(-)})}\Delta p(\overline{W} - 0), \qquad (12)$$

where

$$x_{1,2}^{(-)} \equiv \frac{x}{L_{1,2}^{(-)}}, \quad \tilde{w}_{1,2}^{(-)} \equiv \frac{W}{L_{1,2}^{(-)}},$$
$$L_{1,2}^{(-)} = L_p\frac{r^{(-)}}{\sqrt{1 + (r^{(-)})^2} \pm 1}, \qquad (13)$$
$$r^{(-)} = 2\frac{L_p}{d_p^{(-)}}, \quad d_p^{(-)} = \mu_p(E_0 + E_{var}^{(-)})\tau.$$

Using relationships (8)–(13), we may readily derive expressions the $G(V)$ in a system with arbitrary values of the load resistance R_l. To demonstrate the possibility of suppressing the saturation of $G(V) \equiv I_{ph}/(qg\overline{W})$, let us study in more detail the case when

$$E_{var}^{(-)} = -E_0. \qquad (14)$$
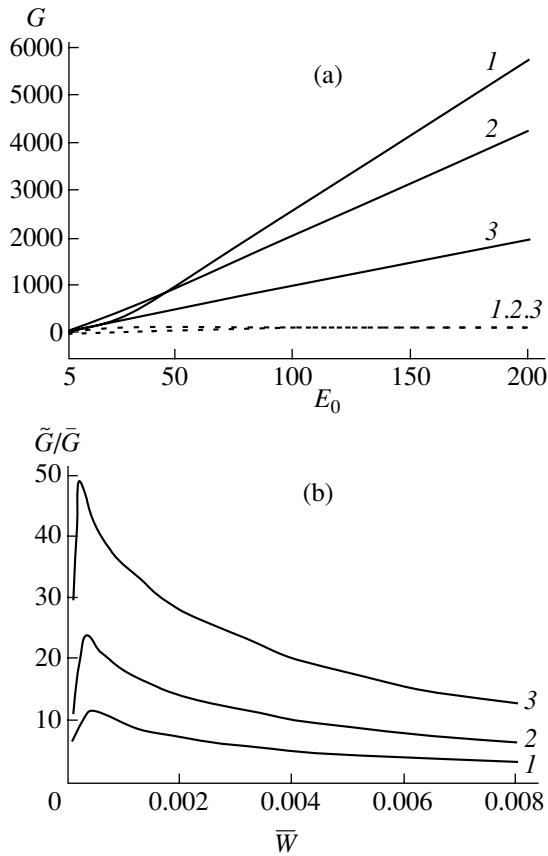
Fig. 2. Behavior of the photoelectric amplification coefficient G for n-CdHgTe with $E_{var}^{(-)} = -E_0$ and a variband layer at the minus contact: (a) plots of $\tilde{G}$ versus E_0 for samples with various homogeneous layer widths $\overline{W} = 5 \times 10^{-5}$ (1), 2×10^{-3} (2), 8×10^{-3} cm (3); dashed line represents the $\overline{G}$ value for a usual homogeneous layer with the thickness $\overline{W}$; (b) plots of $\tilde{G}/\overline{G}$ versus homogeneous layer thickness $\overline{W}$ for various $E_0 = 50$ (1), 100 (2), 200 V/cm (3). Bandgap width, $E_g \cong 0.1$ eV; Temperature $T = 77$ K; electron and hole mobilities $\mu_n = 1.9 \times 10^5$ cm^2/(V s) and $\mu_p = 600$ cm^2/(V s), respectively; nonequilibrium carrier lifetime $\tau = 10^{-6}$ s [1–5, 19, 20]; variband layer thickness $W^{(-)} = 3 \times 10^{-3}$ cm.

Restricting the consideration to a short-circuited chain ($R_l = 0$), we obtain

$$\Delta V \equiv \int_0^W E_{ph} dx = 0. \tag{15}$$

Under the conditions selected,

$$G = \tilde{G} \equiv \frac{\overline{W}}{\overline{W} + W^{(-)}} \frac{1 + \zeta_1^{(1)}}{1 + \zeta_1^{(2)}} \overline{G}$$

$$+ \zeta_2 \frac{2\bar{d}_n L_p th(W^{(-)}/2L_p) + L_p^2 - L_n^2}{\overline{W}(\overline{W} + W^{(-)})} th\left(\frac{W^{(-)}}{L_p}\right), \tag{16}$$

where

$$\overline{G} = \frac{(\mu_n + \mu_p)E_0 \tau}{\overline{W}} \tag{17}$$

$$\times \left\{ 1 - 4\frac{L_p}{\overline{W}} \sqrt{1 + (\bar{d}_p/2L_p)^2} \frac{sh(\bar{w}_1/2)sh(\bar{w}_2/2)}{sh\{(\bar{w}_1 + \bar{w}_2)/2\}} \right\}$$

is a well-known expression for a homogeneous sample (without a near-contact variband layer) [1–6, 22] obtained from (16) for $W^{(-)} = 0$, and

$$\zeta_1^{(1)} = \left\{ \alpha_1 \frac{\alpha_2 + 2\exp(-\bar{w}_1)}{1 - \exp(-\bar{w}_1)} \right.$$

$$\left. - \alpha_2 \frac{2\exp(\bar{w}_2) - \alpha_1}{\exp(\bar{w}_2) - 1} \right\} \frac{th(W^{(-)}/L_p)}{4\bar{r}\alpha}, \tag{18}$$

$$\zeta_1^{(2)} = \frac{\alpha_2 + \alpha_1 \exp(-\bar{w}_1 - \bar{w}_2)}{1 - \exp(-\bar{w}_1 - \bar{w}_2)} \frac{th(W^{(-)}/L_p)}{2\bar{r}}, \tag{19}$$

$$\zeta_2 = \frac{\alpha_1 - 2\alpha\exp(-\bar{w}_2) + \alpha_2 \exp(-\bar{w}_1 - \bar{w}_2)}{2\bar{r} + \alpha_2 th(W^{(-)}/L_p) + \{\alpha_1 th(W^{(-)}/L_p) - 2\bar{r}\}\exp(-\bar{w}_1 - \bar{w}_2)}, \tag{20}$$

$$\bar{d}_n = \mu_n E_0 \tau, \quad \alpha = \sqrt{1 + \bar{r}^2}, \quad \alpha_{1,2} = \alpha \pm 1. \tag{21}$$

For large $E_0 \equiv V/W$ values, which provide for

$$\bar{d}_p \gg 2L_p; \quad \overline{W}; \quad \frac{L_p}{\overline{W}}L_p, \tag{22}$$

expression (17) acquires the following form:

$$G = \tilde{G}_\infty \equiv \frac{\overline{W} + \{2L_p/(b+1)\}th(W^{(-)}/L_p)}{\overline{W} + W^{(-)}} \overline{G}_\infty$$

$$+ \frac{\tau}{t_n^{(W)}} th\left(\frac{W^{(-)}}{2L_p}\right) th\left(\frac{W^{(-)}}{L_p}\right), \tag{23}$$

where $\overline{G}_\infty = (b+1)/2$, and $t_n^{(W)}$ is the electron transit

time from the (−) to (+) contact in the field E_0:

$$t_n^{(W)} = \frac{\overline{W} + W^{(-)}}{\mu_n E_0}. \qquad (24)$$

Relationships (23) and (24) indicate that $G(V)$ exhibits no saturation when $W^{(-)} \neq 0$ ($\tilde{G}_\infty > \overline{G}_\infty$, Fig. 2). A physical mechanism of the $G(V)$ saturation suppression is based on a diffusion character of the $\Delta p(x)$ distribution in the variband layer {var$^{(-)}$} under condition (14) (as well as under the condition $\mu = 0$ [1, 9, 22–24]). As a result, the photoexcited carriers are not (in contrast to the homogeneous case) held against the minus contact (where a strong recombination takes place) even at large values of $E_0 = V/W$.

It should be recalled that initially we assumed the condition of quasineutrality (6) to be valid. This condition is really valid almost everywhere except for the narrow regions in the vicinity of the points where $\Delta p(x) = 0$. Under condition (14), these points occur only on the current contacts. In the general case, such points may exist in the bulk of sample as well. The same situation takes place in the macroscopic analysis of a problem of charge carrier photogeneration in both homogeneous [11–14] and variband [25, 26] semiconductors featuring strong surface recombination. However, the analysis [25, 26] shows that the size of the regions where condition (6) is formally broken is equal by the order of magnitude to the carrier mean free path with respect to momentum. In the macroscopic theory, this value is a physical zero and, hence, the quasineutrality approximation is valid.

It should be noted that, using the method developed [22, 24, 27, 28] for the recombination on impurity centers, it is possible to construct a mathematically more correct (and free of the recourse to the quasineutrality condition (6)) solution to the problem under consideration for arbitrary values of the variband fields near both current contacts (including the case of a sample containing no homogeneous layer [21]), naturally, under the condition of continuity of both electron ($I_{ph}^{(n)}$) and hole ($I_{ph}^{(p)}$) photocurrents and (in contrast to the case considered in [21]) of the photoinduced electric field $E_{ph}(x)$.

REFERENCES

1. A. Rogalski *et al.*, *Infrared Photon Detectors* (SPIE Opt. Engin. Press, Bellingham, 1995).

2. Y. J. Shacham-Diamand and I. Kidron, Infrared Phys. **21**, 105 (1981).

3. *Optical and Infrared Detectors*, Ed. by R. J. Keyes (Springer-Verlag, New York, 1977; Radio i Svyaz', Moscow, 1985).

4. D. L. Smith, F. K. Lo, and J. D. Genova, J. Vac. Sci. Technol. **21** (1), 259 (1982).

5. C. T. Elliot, in *Handbook on Semiconductors*, Ed. by C. Hilsum (North-Holland, Amsterdam, 1982), Vol. 4, pp. 727–798.

6. H. Beneking, IEEE Trans. Electron Devices **ED-29** (9), 1420 (1982).

7. R. A. Smith, *Semiconductors* (Cambridge Univ. Press, Cambridge, 1978; Mir, Moscow, 1982).

8. V. L. Bonch-Bruevich and S. G. Kalashnikov, *Physics of Semiconductors* (Nauka, Moscow, 1990).

9. E. S. Rittner, in *Proceedings of the 1st Photoconductivity Conference, Atlantic City, 1954* (Wiley, New York, 1956), pp. 215–268.

10. J. S. Blakemore, *Semiconductor Statistics* (Pergamon, Oxford, 1962; Mir, Moscow, 1964).

11. G. E. Pikus, *Fundamentals of Theory of Semiconductor Devices* (Nauka, Moscow, 1965).

12. R. H. Bube, *Photoelectronic Properties of Semiconductors* (Cambridge Univ. Press, Cambridge, 1992).

13. S. M. Ryvkin, *Photoelectric Effects in Semiconductors* (Fizmatgiz, Leningrad, 1963; Consultants Bureau, New York, 1964).

14. I. Auth, D. Genzow, K. Herrmann, *Photoelektrische Erscheinungen* (Akademie-Verlag, Berlin, 1977; Mir, Moscow, 1980).

15. A. M. Vasil'ev and A. P. Landsman, *Semiconductor Photoconverters* (Sov. Radio, Moscow, 1971).

16. P. R. Emtage, J. Appl. Phys. **33** (6), 1950 (1962).

17. L. J. van Ruyvent and F. E. Williams, Am. J. Phys. **35** (7), 705 (1967).

18. T. Gora and F. Williams, Phys. Rev. **177** (3), 1179 (1969).

19. P. Migliorato and A. White, Solid-State Electron. **26** (1), 65 (1983).

20. D. L. Smith, Appl. Phys. Lett. **45** (1), 83 (1984).

21. V. G. Savitskiĭ and B. S. Sokolovskiĭ, Fiz. Tekh. Poluprovodn. (St. Petersburg) **31** (1), 3 (1997) [Semiconductors **31**, 1 (1997)].

22. V. A. Kholodnov, Proc. SPIE **3819**, 98 (1999).

23. V. A. Kholodnov and A. A. Drugova, Pis'ma Zh. Tekh. Fiz. **23** (2), 80 (1997) [Tech. Phys. Lett. **23**, 82 (1997)].

24. V. A. Kholodnov, Pis'ma Zh. Éksp. Teor. Fiz. **67** (9), 655 (1998) [JETP Lett. **67**, 685 (1998)].

25. V. A. Kholodnov and A. A. Drugova, Proc. SPIE **3819**, 67 (1999).

26. V. A. Kholodnov and A. A. Drugova, Pis'ma Zh. Tekh. Fiz. **26** (5), 49 (2000) [Tech. Phys. Lett. **26**, 202 (2000)].

27. V. A. Kholodnov and A. A. Drugova, Proc. SPIE **4340**, 29 (2000).

28. V. A. Kholodnov, A. A. Drugova, and N. E. Kurochkin, in *Abstracts of the 25th International Conference of the Physics of Semiconductors, 25 ICPS, Osaka, 2000*, Part I, p. 239.

Translated by P. Pozdeev

A Mechanism of Chaotic Mixing in an Elementary Deterministic Flow

M. V. Budyansky and S. V. Prants

Il'ichev Pacific Oceanological Institute, Russian Academy of Sciences, Vladivostok, Russia
e-mail: prants@mail.ru
Received January 9, 2001

Abstract—A typical mechanism of the chaotic mixing of a passive impurity was theoretically and numerically elucidated using an elementary model of interaction between a point vortex and a periodic plane flow. The chaotic transfer and mixing, appearing as a result of the transversal intersection of stable and unstable manifolds of a hyperbolic stationary point, may lead to far-reaching consequences in geophysical flows. © *2001 MAIK "Nauka/Interperiodica".*

The chaotic (meaning exponentially sensitive with respect to the initial conditions) motion of passive impurity particles may take place in flows which are laminar in the Eulerian representation. This phenomenon, referred to as the Lagrangian turbulence or chaotic advection, was observed in both laboratory and numerical experiments using flows of various types (see review [1] and references therein).

The aim of this study was to elucidate a mechanism of the appearance of a chaotic motion of passive impurity particles using a model system comprising a point vortex interacting with a periodic two-dimensional (2D) flow of incompressible liquid. Such models are very convenient for a theoretical analysis of the chaotic advection development and can provide a knowledge base for understanding the passive impurity transfer and mixing processes under both laboratory conditions and in natural media. In particular, the horizontal chaotic mixing in models of this type adequately describes the effective heat and salinity homogenization in mesoscale oceanic structures and in shallow seas or estuaries [2].

The velocity field of a 2D incompressible flow is determined by a stream function. For a point vortex on the background of a flow containing stationary and periodic (with a frequency ω) components, this stream function can be presented in the following dimensionless form:

$$\Psi = \Psi_0 + \xi\Psi_1 = \ln\sqrt{x^2 + y^2} + \epsilon x + \xi x\sin\tau, \quad (1)$$

where $\tau = \omega t$, x, and y are the normalized time and Cartesian coordinates and ϵ and ξ are the normalized velocities of particles in the stationary and nonstationary flow components, respectively. Using the stream function, the equations of motion of a passive impurity can be written in the Hamiltonian form

$$\dot{x} = -\frac{\partial\Psi}{\partial y} = -\frac{y}{x^2 + y^2},$$

$$\dot{y} = \frac{\partial\Psi}{\partial x} = \frac{x}{x^2 + y^2} + \epsilon + \xi\sin\tau. \quad (2)$$

In the absence of perturbations ($\xi = 0$), the phase portrait of the dynamic system (2) comprises a set of closed and open (infinite) trajectories, separated by a separatrix loop passing through a stationary (fixed) saddle point with the coordinates $(-1/\epsilon;\ 0)$. In the polar coordinates $x = \rho\cos\varphi$ and $y = \rho\sin\varphi$, this problem is readily integrated in quadratures as

$$\epsilon d\tau = \left[1 - \left(\frac{E - \ln\rho}{\epsilon\rho}\right)^2\right]^{-1/2} d\rho, \quad (3)$$

where E is the conserved energy value. The motions of particles possible in the vortex–stationary flow system are very simple: the particles are either entrained by the vortex and move in periodic orbits inside a separatrix loop or move along infinite trajectories in the free flow region outside the loop. Note that the stable branch of the separatrix, by which the imaging point approaches the saddle, and the unstable branch, by which the point moves away from the saddle, coincide in the integrable autonomous vortex–stationary flow system.

Upon switch-on of the external periodic perturbation, even possessing a very small amplitude ξ, the unperturbed separatrix exhibits splitting [3]. For system (2) possessing one and a half degrees of freedom,

the condition of splitting is determined by analysis of the Poincaré integral

$$I(\alpha) = \int_{-\infty}^{\infty} \{\Psi_0, \Psi_1\}[x_s(\tau - \alpha), y_s(\tau - \alpha)]d\tau, \quad (4)$$

where $\{\Psi_0, \Psi_1\}$ is the Poisson bracket for a stationary stream function Ψ_0 and a periodic perturbation Ψ_1 obeying expression (1); $[x_s(\tau - \alpha), y_s(\tau - \alpha)]$ is a solution on the separatrix with a real parameter α. If the function $I(\alpha)$ possesses simple zeros, then the stable and unstable manifolds of the stationary (fixed) saddle point exhibit transversal intersection (for the proof, see [4]). Upon directly taking the integral (4), we obtain a periodic function

$$I(\alpha) = \sin\alpha \int_{-\infty}^{\infty} \dot{x}_s \cos\tau d\tau - \cos\alpha \int_{-\infty}^{\infty} \dot{x}_s \sin\tau d\tau, \quad (5)$$

which apparently possesses simple zeros for $\dot{x}_s(\tau) \neq 0$. The transversal intersection of manifolds leads to the formation of a homoclinic structure in the vicinity of the saddle point of the unperturbed system. This complicated structure is illustrated by Fig. 1 showing a fragment of the Poincaré section at the time instants $2\pi n$ ($n = 0, 1, 2, \ldots$) for a family of trajectories originating at $\tau = 0$ from a small vicinity of the saddle point with $\xi = 0.01$. This is a typical homoclinic structure for Hamiltonian systems (see, e.g., [5]), which contains an infinite set of both periodic and random trajectories. This structure is a nucleus for the formation of a stochastic layer for an arbitrarily small perturbation in the deterministic flow. As the perturbation ξ increases, the layer grows and gradually fills all the energetically accessible phase space.

The transversal intersection of the stable $H^{(+)}$ and unstable $H^{(-)}$ manifolds is the mechanism leading to stretching and folding of the liquid phase element and, hence, to the effective mixing. A characteristic mixing time, called the correlation splitting time and representing a statistical characteristic of the process, is inversely proportional to the maximum Lyapunov index λ—a purely dynamic characteristic. We calculated the λ values and topographic λ-maps (these results are not reported here) using an algorithm proposed in [6], which provide quantitative characteristics of the dynamic chaos depending on the initial conditions and the perturbation ξ.

In order to illustrate the particle advection dynamics with a horseshoe-type mapping [5], we have calculated the evolution of an ensemble of particles in the regions of laminar and turbulent (in the Lagrangian sense) flow. Figure 2 shows the evolution of a small spot, comprising ~10^4 tracers in the region of the saddle point, calculated at the time instants $\tau = 0, 2\pi, 4\pi,$ and 6π. The spots
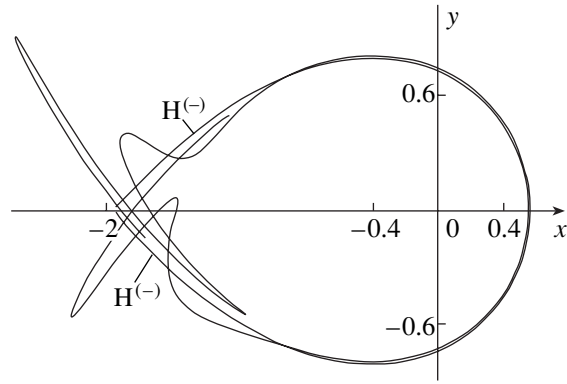

Fig. 1. Transversal intersection of stable and instable saddle manifolds as a nucleus of the homoclinic chaos ($\epsilon = 0.5$; $\xi = 0.01$).
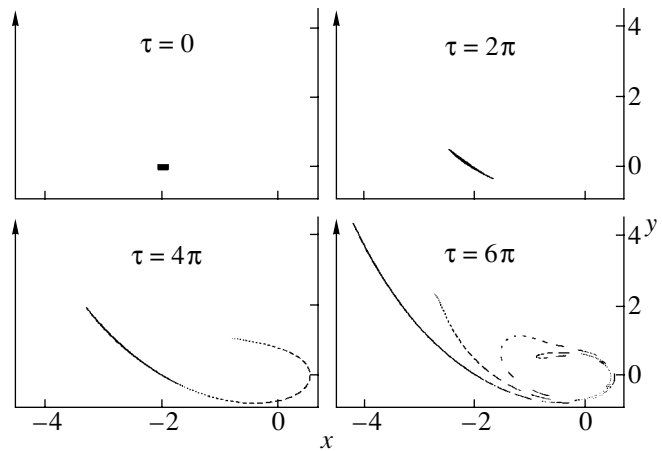

Fig. 2. Time evolution of a passive impurity liquid phase drop in the chaotic flow region ($\epsilon = 0.5$; $\xi = 0.1$).

exhibit an evident stretching deformation followed by folding, which is typical of the horseshoe mapping. The spot perimeter grows exponentially with time, while the spot area (invariant of the Hamiltonian system) remains unchanged. This leads to a significant increase in the rate of the usual turbulent impurity diffusion (if this takes place), because the chaotic advection development markedly increases the boundary between the impurity and liquid.

The motion of passive impurity particles in a nonstationary flow significantly depends on their initial positions. For moderate values of the perturbation ξ, there is a preserved core surrounding the vortex, which consists of closed instantaneous stream lines corresponding to invariant cures in the Poincaré section. Particles occurring in this region perform strictly periodic motions. For particles occurring in the core, there are effective "barriers" hindering their penetration into the free flow region. Near the separatrix loop, the invariant curves break to form the invariant Cantorian manifolds (cantors). The motion along these curves is analogous

to the motion along invariant curves, except for the slits through which the tracers may diffuse from the core vicinity to the free flow region. This nontrivial transfer of the tracers may lead to far-reaching consequences in geophysical flows, as manifested by the anomalous transport of contaminants, heat, and other passive impurities in vortex structures of the ocean and atmosphere.

REFERENCES

1. H. Aref, Philos. Trans. R. Soc. London, Ser. A **333**, 273 (1990).

2. V. F. Kozlov and K. V. Koshel', Izv. Akad. Nauk, Fiz. Atmos. Okeana **35** (1), 137 (1999).

3. H. Poincaré, Acta Math. **13**, 1 (1890).

4. V. V. Kozlov, *Symmetry, Topology and Resonances in Hamiltonian Mechanics* (Udmurt. Gos. Univ., Izhevsk, 1995).

5. A. J. Lichtenberg and M. A. Lieberman, *Regular and Stochastic Motion* (Springer-Verlag, New York, 1983; Mir, Moscow, 1984).

6. L. E. Kon'kov and S. V. Prants, Pis'ma Zh. Éksp. Teor. Fiz. **65** (11), 801 (1997) [JETP Lett. **65**, 833 (1997)].

Translated by P. Pozdeev

A Nonlinear Dynamics of Stimulated Phonon Emission in a Nonautonomous Acoustic Quantum Generator under Superlow-Frequency-Modulated Pumping Conditions

D. N. Makovetskiĭ

Usikov Institute of Radiophysics and Electronics, National Academy of Sciences of Ukraine, Kharkov, Ukraine
e-mail: makov@ire.kharkov.ua

Abstract—A nonlinear resonance was experimentally observed in a ruby acoustic quantum generator operating in the region of 10^{10} Hz with electromagnetic pumping modulated at a superlow frequency. The resonance is manifested by slow regular self-detunings in the microwave spectra of stimulated phonon emission. The self-detuning period T_{SD} strongly depends on $\Delta_L \equiv \omega_m - \omega_L$, where ω_m is the modulation frequency and ω_L is the resonance frequency varying from 9.8 to ~5 Hz when the magnetic field detuning grows from 0 to 60 Oe. The direction of motion of a mode cluster along the frequency axis is uniquely determined by the sign of Δ_L. As the $|\Delta_L|$ value decreases to 0.05 Hz, the self-detuning period increases to very large values $T_{SD} > 100$ s. These large-scale collective motions take place against the background of small-scale low-frequency chaotic oscillations in intensity of the generated phonon modes, while the mode widths remain almost as narrow (< 1 kHz) as those in the autonomous regime. © *2001 MAIK "Nauka/Interperiodica".*

The process of regular and chaotic stimulated emission of microwave phonons in a multimode nonautonomous acoustic quantum generator was experimentally observed and studied [1–3] for $\omega_m \approx \omega_R \approx 20$–300 Hz, where ω_m is the pumping modulation frequency and ω_R is the relaxation frequency (depending on the pumping level) of a nonequilibrium autonomous acoustic system. The existence of a single dominating component $\exp(i\omega_R t)$ for the transient processes in the autonomous acoustic quantum generator reflects the collective character of a multimode stimulated emission [4, 5] in the quantum generators of class B [6], an acoustic analog of which is represented by a system studied in [1–3]. As a result, the nonlinear dynamics of the integral intensity of the multimode stimulated phonon emission $J_\Sigma(t)$ in a nonautonomous acoustic quantum generator operating at $\omega_m \approx \omega_R$ is satisfactorily described by a single-mode model [6].

Outside the region of the nonlinear low-frequency resonance indicated above, the pronounced dependence of the mode variables on the order parameter J_Σ is violated. Even in a two-mode regime of the class B quantum generator, evolution of the partial components $J_{1,2}(t)$ qualitatively differs from $J_\Sigma(t)$ [5]. In particular, the system may exhibit manifestations of a new nonlinear resonance at a frequency $\omega_L \ll \omega_R$, which is related to the intermode energy exchange.

In this study, a nonlinear superlow-frequency resonance in an acoustic quantum generator was experimentally observed for the first time at $\omega_m \approx \omega_L \lesssim 10$ Hz. This resonance leads to a manifold narrowing of the

microwave spectrum of stimulated phonon emission and to the appearance of slow regular self-detunings at still lower frequencies depending on the parameter $\Delta_L \equiv \omega_m - \omega_L$.

The experiments were performed at $\omega_m = 2$–20 Hz with an acoustic quantum generator [1–3] with electromagnetic pumping at a frequency of $\Omega_P = 2.3 \times 10^{10}$ Hz and the mode frequencies Ω_N of the generated phonons occurring near a maximum of the noninverted acoustic paramagnetic resonance line $\Omega_S = 9.12 \times 10^9$ Hz. Since the sound velocity in the system studied was $\approx 10^6$ cm/s, the wavelengths of the generated microwave acoustic field were close to optical ($\lambda_N \approx 1$ μm). The intermode spacing was $\Omega_N - \Omega_{N-1} = 3.1 \times 10^5$ Hz and the total number of modes reached $N_0^{\max} = 23$ at a nonmodulated pumping power of $P = 1.2 \times 10^{-2}$ W and a cavity quality factor of $Q_P = 10^4$.

The main element of the acoustic quantum generator studied is a solid-state microwave acoustic Fabry–Pérot resonator made of a paramagnetic ruby crystal ($Al_{2(1-x)}O_3 : Cr^{3+}_{2x}$, $x \approx 3 \times 10^{-4}$) and possessing an intrinsic mode Q-factor of $Q_N \approx 10^6$. One of the resonator acoustic mirrors was coated with a textured piezoelectric ZnO film capable of detecting longitudinal acoustic oscillations. These oscillations were excited in the ruby crystal lattice by the paramagnetic Cr^{3+} ions during the spin transitions $S_3 \longrightarrow S_2$ with simultaneous pumping of the transitions $S_1 \longrightarrow S_3$ and $S_2 \longrightarrow S_4$
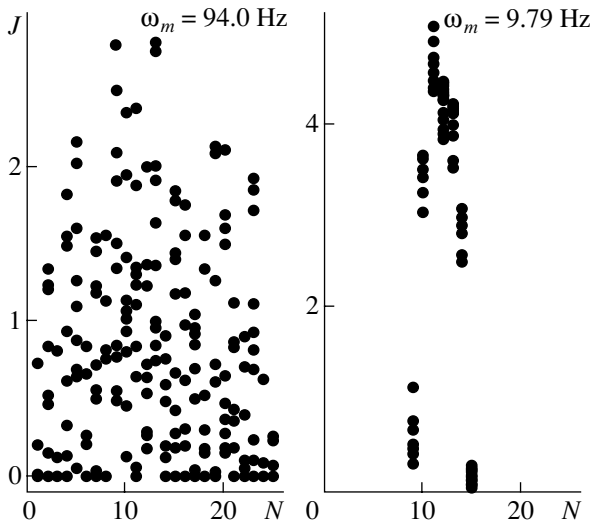
Fig. 1. Stroboscopic spectra of a stimulated microwave phonon emission of an acoustic quantum generator with the electromagnetic pumping modulated in the region of low-frequency (left diagram) and superlow-frequency (right diagram) nonlinear resonances. N is the mode number; J is the instantaneous intensity of the stimulated emission normalized to the intensity of the central (maximum power) mode of the autonomous generation.

(S_i are the ground spin multiplet levels numerated in the order of increasing energy). All the experiments were performed by measuring the microwave spectra of the longitudinal acoustic oscillations at a temperature of $\theta = 1.8$ K in a magnetic field within the interval $|\Delta H| \leq 100$ Oe, where $\Delta H = H - H_0$ and $H_0 = 3920$ Oe. The magnetic field vector $\mathbf{H}$ was always oriented at an angle of $54°44'$ with respect to the optical axis of the ruby crystal, which was necessary to ensure the condition $S_3 - S_1 = S_4 - S_2$.

A special feature distinguishing this experiment from those described in [1–3] was the use of a pulse lock-in method for detecting the microwave acoustic spectra. The essence of the method is as follows. A stimulated phonon emission generated in the crystal is converted by the piezoelectric film into an electromagnetic signal transmitted to a microwave spectrum analyzer. In the normal state, a beam of the input oscilloscope in the spectrum analyzer is shut off. The oscilloscope is periodically open by strobe pulses only within very short time intervals $\Delta t_{\mathrm{str}} \ll T_m$ ($T_m = 2\pi/\omega_m$), with the strobing period T_{str} being equal exactly to the period of external pumping modulation T_m. At each lock-in time instant, the beam displayed a set of points on the oscilloscope screen indicating an instantaneous frequency distribution of the phonon mode intensity.

The shutter of a camera making photographs of the oscilloscope screen is open within a certain registration time interval t_{reg}, which is set as $t_{\mathrm{reg}} = nT_m$ ($n \gg 1$ being an integer). Therefore, each camera shot represents a series of superimposed point sets. If the period of inten-

sity oscillations for all of the generated phonon modes coincides with the external modulation period T_m, a spectrum measured in this stroboscopic regime must contain a singe point representing each mode.

A different situation takes place when the intensity oscillations of the generated phonon modes are not in phase with the modulation factor. For example, if the oscillation period is doubled simultaneously for all the modes, the number of points on the image would double as well. An especially illustrative pattern is observed for the stimulated emission periodicity breakage, whereby the distribution of points on the image becomes chaotic, the intermode correlation is lost, etc.

It is important to note that both qualitative and quantitative information can be obtained concerning the degree of spectral ordering, the character of regular and irregular detunings in the mode structure, etc. The proposed method is essentially a generalization of the well-known Poincaré method of sections (see, e.g., [6]) to the case of a multimode system. A highly illustrative character—one of the main advantages of the Poincaré method—is fully inherited in the proposed approach.

Figure 1 shows typical stroboscopic spectra of the stimulated phonon emission measured at $\omega_m = 94.0$ Hz (i.e., in the region of a low-frequency resonance $\omega_m \approx \omega_R$) and at $\omega_m = \omega_L = 9.79$ Hz (at the maximum of the superlow-frequency resonance observed for the first time). The measurements were performed for $n = 10$. As is clearly seen, a low-frequency destabilization of the generation process is manifested primarily by a strong chaotic amplitude modulation of the phonon modes (left diagram in Fig. 1). This is accompanied by a certain broadening of the spectrum ($N_R^{(\mathrm{max})} = 25$) as compared to that observed in the autonomous regime. The variation of ω_m from 70 to 200 Hz does not lead to qualitative changes of the general pattern (in agreement with the data reported previously for $J_\Sigma(t)$ [1–3]).

On the contrary, a superlow-frequency destabilization of the generation process is manifested by a pronounced (manifold) narrowing of the spectrum ($N_L^{(\mathrm{max})} = 7$) on the background of a significantly lower mode amplitude modulation (right diagram in Fig. 1). However, a much more pronounced feature is the appearance of self-detunings in the microwave phonon spectrum for ω_m deviating from the maximum of the superlow-frequency resonance at $\omega_L = 9.79$ Hz. The self-detuning process is manifested by the motion of the region of localization of this relatively narrow mode cluster along the frequency axis at a retained localization (width) of each mode. In other words, new modes are sequentially "fired" on one side of the cluster and approximately the same number of modes are "extinguished" on the other side, up to a complete generation breakdown in a certain final portion of the frequency axis. This is usually followed by a short-time refractority state, after which the generation is fired again in the

opposite (starting) portion of the frequency axis and the entire process of collective motions is multiply repeated at a period of $T_{SD} \gg T_m$.

Figure 2 shows a series of stimulated phonon emission spectra measured for $\Delta_L = -0.23$ Hz and $\Delta_H = 0$. A time interval of $T_E \approx 2.5$ s between sequential exposures E_K in Fig. 2 (in contrast to Fig. 1) is selected to be much greater than T_m. For the Δ_L value indicated above, the self-detuning period is $T_{SD} \approx 14$ s. The results of experiments showed that the T_{SD} value strongly depends on both the absolute value and sign of Δ_L and varies from a few tenths of a second for $|\Delta_L| \approx 1$ Hz up to very large values $T_{SD} > 100$ s for $|\Delta_L| < 0.05$ Hz. The direction of motion of the mode cluster is determined by the sign of Δ_L: for the virtual cluster maximum position denoted by Ω_B, the direction is such that $\mathrm{sgn}(d\Omega_B/dt) = -\mathrm{sgn}\Delta_L$.

The analogous character of self-detunings in the microwave phonon spectrum in the region of the superlow-frequency resonance is retained on the whole in a rather broad range of Δ_H. Moreover, in the entire region of $|\Delta_H| < 10$ Oe, even the ω_L value remains virtually the same (close to 9.8 Hz). Only for a still greater detuning of the spin system with respect to the magnetic field (under these conditions, even an autonomous acoustic quantum generator may exhibit some insufficiently studied generation features [7]), the resonance frequency ω_L begins to drop significantly (approximately by half for $|\Delta_H| \approx 60$ Oe). Here (because of a decrease in the level of pumping, which passes via a wing of the paramagnetic resonance line), the stimulated phonon emission intensity drops by more than one order of magnitude. A change in the sign of Δ_H does not influence the self-detuning process (in contrast to the case of changing the sign of Δ_L considered above).

On the whole, the dynamics of the collective motions described above is somewhat analogous to that of autowaves [8]. Indeed, the observed moving spectral structures (like the usual autowaves) are independent (within certain limits) of perturbations in the control parameters and probably result from a self-organization in the open dissipative system of an acoustic quantum generator. The energy of external excitation (in our case, a pumping field) is spent for maintaining this state, while selective external factors only switch on certain internal processes changing the system behavior. Although the motions observed in our experiments occur in the spectral "space," these phenomena naturally reflect the corresponding processes in the real physical space of a distributed active system of the acoustic quantum generator studied.

It should be emphasized that the above-described self-detunings in the phonon spectra of a nonautonomous acoustic quantum generator, as well as the recently observed nonlinear phenomena in electromagnetic masers [9] and autonomous acoustic quantum
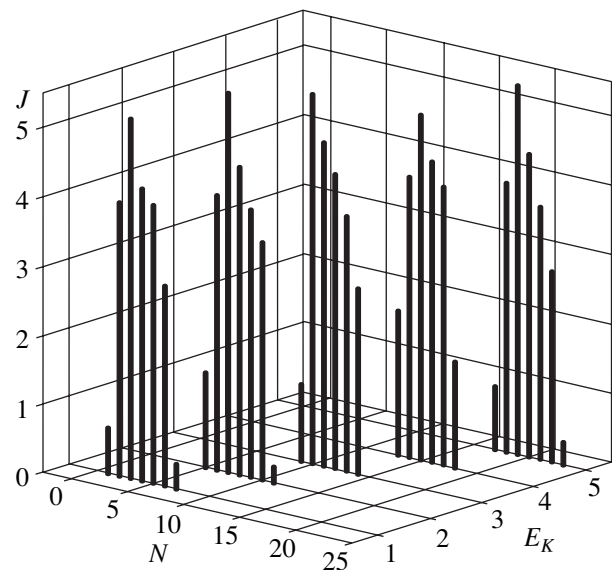
Fig. 2. A series of stimulated phonon emission spectra measured for small detunings ($\Delta_L = -0.23$ Hz) of the modulation frequency relative to the superlow-frequency resonance maximum. E_K is the number of sequential exposure for the spectra taken at an interval of $T_E \approx 2.5$ s (other notations as in Fig. 1).

generators [7, 10], possess an essentially nonthermal character. Although the lower characteristic frequencies of the motions observed in this study fall within a millihertz frequency range, all these motions are related to the microwave field self-action through a spin system of a paramagnet in the absence of the so-called phonon bottleneck effect [11] (and of the resulting phonon avalanche [12]). Therefore, no overheating of the stochastic phonon subsystem takes place in the spectral range of $\approx 10^8$ Hz corresponding to a width of the acoustic paramagnetic resonance on the $S_2 \longleftrightarrow S_3$ transition in a ruby crystal. The observed frequencies of the chaotic amplitude modulation occur below 10^3 Hz, while the microwave modes of the stimulated phonon emission remain very broad ($\Delta\Omega_N < 10^{-7} \, \Omega_N$) for both $\omega_m \approx \omega_R$ and $\omega_m \approx \omega_L$. In this respect, behavior of the studied system qualitatively differs from that of the optical quantum generators of class A featuring a large-scale breakage of coherency (by the hydrodynamics turbulence type [13, 14] of the stimulated emission).

REFERENCES

1. E. M. Ganapol'skiĭ and D. N. Makovetskiĭ, Zh. Tekh. Fiz. **59** (10), 202 (1989) [Sov. Phys. Tech. Phys. **34**, 1220 (1989)].

2. E. M. Ganapol'skiĭ and D. N. Makovetskiĭ, Zh. Tekh. Fiz. **62** (2), 187 (1992) [Sov. Phys. Tech. Phys. **37**, 218 (1992)].

3. E. M. Ganapol'skiĭ and D. N. Makovetskiĭ, Dokl. Akad. Nauk Ukr., No. 6, 69 (1993).

4. K. Weisenfeld, C. Bracikowski, G. James, and R. Roy, Phys. Rev. Lett. **65** (14), 1749 (1990).

5. M. Georgiou and P. Mandel, IEEE J. Quantum Electron. **QE-30** (3), 854 (1994).

6. A. M. Samson, L. A. Kotomtseva, and N. A. Loĭko, *Auto-Oscillations in Lasers* (Nauka i Tekhnika, Minsk, 1990).

7. E. M. Ganapol'skiĭ and D. N. Makovetskiĭ, Pis'ma Zh. Tekh. Fiz. **20** (21), 65 (1994) [Tech. Phys. Lett. **20**, 882 (1994)].

8. V. A. Vasil'ev, Yu. M. Romanovskiĭ, and V. G. Yakhno, *Autowave Processes* (Nauka, Moscow, 1987).

9. D. N. Makovetskiĭ, A. A. Lavrinovich, and N. T. Cherpak, Zh. Tekh. Fiz. **69** (5), 101 (1999) [Tech. Phys. **44**, 570 (1999)].

10. D. N. Makovetskiĭ, Radiofiz. Élektron. **4** (2), 91 (1999).

11. A. A. Antipin, L. D. Livanova, and A. A. Fediĭ, Fiz. Tverd. Tela (Leningrad) **20** (6), 1783 (1978) [Sov. Phys. Solid State **20**, 1030 (1978)].

12. V. A. Golenishchev-Kutuzov, V. V. Samartsev, and B. M. Khabibulin, *Pulsed Optical and Acoustical Spectroscopy* (Nauka, Moscow, 1988).

13. K. Staliunas and C. O. Weiss, J. Opt. Soc. Am. B **12** (6), 1142 (1995).

14. C. O. Weis, M. Vaupel, K. Staliunas, *et al.*, Appl. Phys. B: Lasers Opt. **B68** (2), 151 (1999).

Translated by P. Pozdeev

On the Mechanisms of Nonlinear Optical Attenuation in Fullerene-Containing π-Conjugated Organic Systems

N. V. Kamanina

Vavilov Optical Institute, State Scientific Center of the Russian Federation, St. Petersburg, 199034 Russia
e-mail: kamanin@ffm.ioffe.rssi.ru
Received February 6, 2001

Abstract—The nonlinear optical transmission properties of fullerene-containing π-conjugated organic structures based on 2-cyclooctylamino-5-nitropyridine, 2-(*n*-prolinol)-5-nitropyridine, *N*-(4-nitrophenyl)-(L)-prolinol, and photosensitive polyimide were studied. The laws of the nonlinear optical attenuation phenomenon are established and the possible mechanisms of the laser radiation attenuation in the visible range are formulated. It is shown that an adequate explanation of the optical attenuation effect requires taking into account the reverse saturated absorption, the Förster transfer mechanism, the absorption due to free carriers, and the complex formation. © *2001 MAIK "Nauka/Interperiodica".*

A currently important problem in the physics of condensed media and biomedicine is related to the task of protecting the human eye and the sensors of instruments detecting high-power light beams from radiation damage. Therefore, the search for new systems capable of serving as effective nonlinear optical absorbers implies the necessity of studying the physical processes involved in the interaction of light with absorbing substances. The discovery of fullerenes stimulated the search for media absorbing laser radiation in a broad range of frequencies and intensities. The study of fullerene-containing π-conjugated organic compositions is of special interest because these compounds readily manifest the light-induced nonlinear optical effects and their physical properties can be varied within broad limits by introducing various dopant molecules.

Among the numerous nonlinear optical effects, a special place belongs to the optical attenuation of laser radiation. Interpretations of this effect in various media are frequently based on different mechanisms. In the case of solutions, the attenuation of laser beams is believed (although this is a matter of discussion) to be determined to a considerable extent by the light scattering; in liquid crystals, an important role belongs to the ability of liquid-crystalline dipoles to reorient themselves under the action of external fields; in composite materials, the dominating role belongs to intermolecular interaction.

In thin films of pure fullerenes, the reverse saturated absorption due to transitions from excited vibrational electron levels of molecules is manifested and considered as the main attenuation mechanism in the visible spectral range. This is related to the unique optical properties of fullerene molecules [1–3]. The optical attenuation effect is determined by the formation of excited states of fullerene molecules, with a light absorption cross section exceeding that in the ground state. If a laser radiation pulse duration is ~10–20 ns (i.e., exceeds the singlet–triplet interconversion time of 1.2 ns), the attenuation effect is manifested by the $T_n \longrightarrow T_1$ transition scheme.

At present, however, the main laws of the laser radiation attenuation in fullerene-containing π-conjugated organic systems featuring pronounced intramolecular complex-formation processes have not been established, mechanisms adequately describing these laws have not been formulated, comparative experiments with both simple and complex organic matrices sensitized by fullerenes have not been carried out in sufficient amount, and consistent investigations aimed at explaining this phenomenon have not yet been undertaken. We will demonstrate that the fullerene-containing π-conjugated organic molecules offer a convenient model system for the verification of several mechanisms capable of describing the attenuation of laser radiation propagating in such nonlinear optical media.

The first experimental results [4–6] obtained from the study of optical and mass spectra, diffraction efficiency, photoconductivity, and photosensitivity of fullerene-containing π-conjugated organic compositions showed that these are promising materials for nonlinear optical attenuators, in which a threshold energy density characterizing the optical shutter is controlled by varying the percentage content of C_{60} or C_{70} additive, rather than by changing the type of sensitizing dopant.

In this study, we performed for the first time a systematic investigation of the main laws and mechanisms of the optical attenuation of laser radiation in four π-conjugated organic systems based on 2-cyclooctylamino-5-nitropyridine (COANP), 2-(*n*-prolinol)-5-
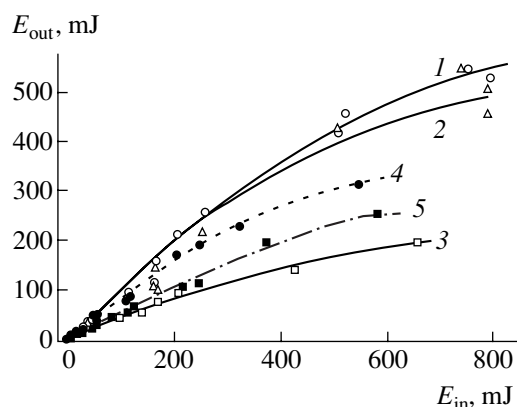
Fig. 1. The plots of output radiation energy (E_{out}) versus input energy (E_{in}) for thin fullerene-containing films: (*1*) COANP–0.5 wt % C_{70}; (*2, 3*) COANP–5 wt % C_{70} compositions with the COANP/plasticizer ratios 1 : 1 and 2 : 1, respectively; (*4, 5*) PI-6B containing 0.2 and 0.5 wt % C_{70}, respectively.

nitropyridine (PNP), *N*-(4-nitrophenyl)-(L)-prolinol (NPP), and polyimide 6B (PI-6B). The results showed that all the established features have to be taken into account in the development of modern nonlinear optical absorbers for the visible spectral range.

The experiments were performed with the above photosensitive compounds in the form of 3–5% solutions in tetrachloroethane, which were sensitized by C_{60} or C_{70} fullerenes added to a concentration of 0.1–5 wt %. Thin films based on COANP, PNP, and NPP were prepared with nonphotosensitive polyimides (PI-81A and PI-81B) additives (plasticizing agents) increasing the film-forming properties of solutions. The compositions studied were applied by centrifuging onto glass substrates with preliminarily deposited conducting layers (necessary for the subsequent photoconductivity measurements). The sample film thicknesses varied within 1–5 μm. For comparative tests, we also prepared thin films of nonphotosensitive polyimides 81A and 81B containing 1 wt % of C_{60} or C_{70} fullerenes.

The optical attenuation of laser radiation in the fullerene-containing media described above was studied using a single-pass scheme [3]. The radiation source was based on a pulsed Nd:YAG laser operating at a pulse duration of 15 ns. The wavelength of the incident radiation upon the second-harmonic conversion was 532 nm. The laser spot diameter on a sample was 3–3.5 mm. We have measured the energy incident onto and transmitted through the sample. The incident radiation energy was varied with the aid of calibrated light filters.

Figure 1 shows the plots of output radiation energy (E_{out}) versus input energy (E_{in}) for thin fullerene-containing films of COANP and PI-6B. Curve *1* refers to a COANP–0.5 wt % C_{70} system, curves *2* and *3* show the transmission of COANP-based films with 5 wt % C_{70} differing by the ratio of COANP to a film-forming additive (1 : 1 and 2 : 1, respectively), and curves *4* and *5* represent the data for PI-6B films with 0.2 and 0.5 wt % C_{70}, respectively. The curves were constructed for the experimental points using a polynomial approximation with an error of ~5%. As seen from these data, all the sensitized (fullerene-containing) systems exhibit incident beam energy attenuation by a factor of 3–3.5 for an input energy of E_{in} ~ 550–600 mJ. For the film thicknesses indicated above (several microns), this input energy corresponds to an incident energy density of ~3–4 J/cm².

Thus, the samples exhibit a sufficiently high optical attenuation level that conforms to the rated values and allows the materials studied to be applied in attenuators of intense laser beams [7]. Since the compositions studied represent molecular systems characterized by the absorption cross section in the excited state exceeding that in the ground state (for PI-6B, the ratio of the absorption cross sections of triphenylamine– fullerene and diimide–triphenylamine complexes were calculated in [8]), the higher attenuation capacity of the compositions with a greater fullerene content is certainly related to the phenomenon of reverse saturated absorption. However, in addition to the concentration dependence manifested in this test, it is necessary to take into account the spectral features and the molecular structures of COANP and polyimide matrices.

Indeed, the absorption spectrum of a fullerene-containing PI-6B overlaps with the fluorescence spectrum of the pure polyimide matrix in the vicinity of the laser radiation wavelength (532 nm). This implies that the composition studied satisfies the resonance conditions for excitation of a photosensitive system by the Förster mechanism [9]. This mechanism is valid under the conditions of weak binding between the interacting components. The superposition of the fluorescence and absorption spectrum is indicative of the overlap of electron shells of the two molecules (fullerene and polyimide), which may account for the charge carrier (and excitation energy) transfer over limited distances between these molecules.

In order to additionally verify the possibility that this mechanism may contribute to the optical attenuation of laser radiation, we prepared thin-film samples sensitized simultaneously by fullerenes and a Malachite Green (MG) dye. In the latter case, the radiation was attenuated by a factor of 8–10, which exceeds the level observed in the samples sensitized separately by either fullerene or MG. The degree of attenuation by the fullerene–dye combination was even greater than that in the compositions containing twice the amount of any one sensitizer alone. Thus, taking into account that the fluorescence spectrum of MG overlaps with the absorption spectrum of a fullerene-containing PI-6B, a multistep excitation transfer takes place between a donor fragment of the polyimide molecule (tripheny-

lamine) and fullerene, MG and fullerene, and triphenylamine and MG in a π-conjugated organic matrix sensitized simultaneously by several agents. In addition, the electron affinities of an acceptor polyimide fragment (diimide), MG dye, and fullerene are 1.12, 1.6, and 2.65 eV, respectively. This indicates that fullerene is a stronger electron acceptor than both the intramolecular fragment of the π-conjugated organic structure and the dye and, probably, also the intramolecular fragment of PI (fullerene may form a charge-transfer complex with the donor fragment of polyimide).

The Förster energy transfer mechanism and the possible complex formation agree quite well with the results of conductivity measurements in fullerene-containing PI-6B films. Both conductivity and photoconductivity of the fullerene-sensitized samples were 10–15 times greater than the values in pure (fullerene-free) polymer films. Taking into account that the activation energy for conductivity in polyimides coincides with that for the carrier mobility, so that the conductivity is determined predominantly by the carrier mobility rather than concentration, we may estimate the mobility of charge carriers in PI-6B films with the C_{70} fullerene. It was found that the carrier mobilities were higher by one order of magnitude in sensitized samples than in pure polymer films. The estimates were obtained for a current of $\sim 7.2 \times 10^{-10}$ and 8×10^{-9} A for the pure and sensitized (0.2 wt % C_{70}) samples, respectively; the applied voltage, 70 V; the film thickness $d = 1$ μm; and the dielectric constant $\varepsilon \sim 3$. For the conductivity measurements, the second (upper) electrode was made of gold and had a diameter of 2 mm. Taking into account the shape of the current–voltage characteristics, the mobilities were calculated using the Child–Langmuir formula [10]. Note that an increase in the charge carrier mobility implies a change in the chain length in the polyconjugated system, which probably takes place due to a fullerene molecule substituting for (or dominating over) the intramolecular acceptor fragment of the organic molecule as a result of the intermolecular interaction. A possible modification of the polyconjugated chain in fullerene-containing polyimide structures is confirmed by the fact that an increase in the fullerene content in a π-conjugated organic matrix is accompanied by a bathochromic shift that was previously reported in [4].

As for the COANP-based structures (see curves *1–3* in Fig. 1), the effect of optical attenuation of laser radiation in this composition can be explained taking into account the presence of an additional absorption band at 490–520 nm for the fullerene-sensitized samples, which is absent in the spectra of pure COANP films. The laser radiation wavelength (532 nm) falls within the interval of existence of this band. In addition, it was established that the absorption in this region increases with the fullerene concentration and exhibits a "red" shift (i.e., it shifts toward longer wavelengths). The absorption spectra of C_{70} and COANP are close, which
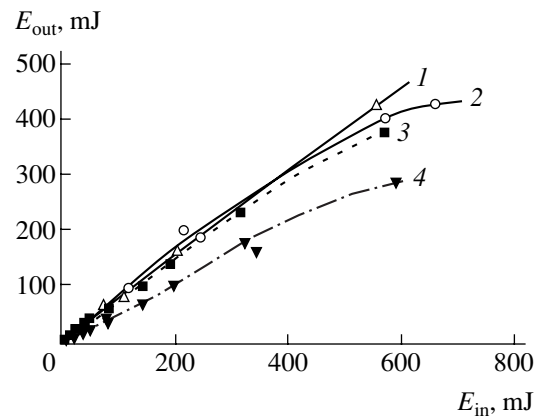
Fig. 2. The plots of output radiation energy (E_{out}) versus input energy (E_{in}) for thin fullerene-containing films: (*1*) PNP–1.0 wt % C_{70}; (*2*) PNP–1.0 wt % C_{60}; (*3*) NPP–1.0 wt % C_{70}; (*4*) NPP– 1.0 wt % C_{60} (PNP or NPP to plasticizer ratio, 1 : 1).

implies a strong electric dipole–dipole interaction between the electron degrees of freedom of the fullerene and COANP molecules [5]. The presence of such interaction explains the spectral features of fullerene-sensitized COANP and confirms the possibility of complex formation in fullerene-containing COANP-based compositions.

The occurrence of complex formation in COANP, PNP, and NPP compositions with fullerenes is confirmed by the following data, The acceptor fragment of COANP, PNP, and NPP molecules is an NO_2 group linked to a donor fragment via a benzene ring. While the individual NO_2 molecule or radical possess an electron affinity of 2.3 eV, this value for an NO_2 group conjugated with a benzene ring decreases to only 0.54 eV [11] and becomes lower by more than four orders of magnitude than the electron affinity of fullerene. Thus, a fullerene molecule in the compositions studied is a stronger electron acceptor than the intramolecular acceptor fragments of COANP, PNP, and NPP molecules. The photoconductivity data obtained by measuring the current–voltage characteristics of the film samples are also consistent with the possible complex formation. Moreover, since the charge carriers transferred to fullerene molecules are delocalized, the fact that the photoconductivity increases in fullerene-sensitized samples is indicative of the presence of free carriers in the system. Therefore, the absorption due to these carriers must be taken into account in explaining the nonlinear optical transmission properties of fullerene-containing π-conjugated media in the visible spectral range.

It must be pointed out that the spectra of PNP- and NPP-based compositions with a C_{60} fullerene exhibit some increase in absorption at 532 nm, while no such increase is observed in the spectra of analogous compositions with a C_{70} fullerene. Apparently, a significant

role in the nonlinear absorption of the former compositions (see curves *2* and *4* in Fig. 2) belongs to the closely spaced intrinsic resonance absorption line of C_{60}. Moreover, it was demonstrated [12] that laser-stimulated electron–hole pair production may lead to a photoinduced absorption increase in the region of optical transitions forbidden in C_{60} molecules and to a longwave shift of the allowed transitions. This effect probably leads to a more favorable matching between the wavelength used in our experiments and the absorption bands of fullerene-containing PNP and NPP films.

It should be noted that comparative experiments with polymeric systems containing no intramolecular donor–acceptor complexes (PI-81A and PI-81B) and with simple organic molecules (azulene, naphthalene) showed no evidence of nonlinear optical transmission unless the radiation energies reached levels considerably exceeding those used in this study (even with a fullerene content several times greater than the concentrations used for sensitization of the π-conjugated organic systems studied). Thus, we may suggest that a necessary prerequisite for the nonlinear optical attenuation effect in a medium is the presence of weakly bound π-electrons and the existence of an initial donor–acceptor interaction, which is increased by fullerene molecules. The fullerene-enhanced donor–acceptor interaction not only accounts for the optical attenuation phenomenon, but may qualitatively explain an increase in the efficiency of hologram recording [6] in fullerene-containing samples of the compositions studied. Apparently, a field gradient appearing upon changing the pathway of charge transfer (from an intramolecular donor fragment to fullerene molecule, rather than to the intramolecular acceptor fragment) is capable of producing a photorefractive effect in fullerene-containing structures interacting with laser radiation in the visible spectral range. The photorefractive effect leads to significant changes in the light-induced refraction, which was manifested in the holographic experiments in both nano- and picosecond intervals.

Conclusions. We have studied the nonlinear optical transmission properties of four fullerene-containing π-conjugated organic systems and the related phenomenon of nonlinear attenuation of laser radiation in the visible ($\lambda = 532$ nm) spectral range. The experimental results are explained in terms of the reverse saturated absorption, the Förster energy transfer mechanism, the absorption due to free carriers, and the complex formation. It is established that an effective manifestation of the nonlinear optical properties in a system requires that the system would feature the intramolecular donor–acceptor interaction, which may increase in the presence of fullerenes. The films containing no intramolecular donor–acceptor complexes showed no evidence of the nonlinear optical transmission (even with a rather high C_{60} or C_{70} fullerene content) unless the incident radiation energies reached a level of ~2 J/cm^2. The reported results may be useful for investigations of the phenomenon of nonlinear optical attenuation in the visible spectral range in other π-conjugated organic structures and for the development of nonlinear optical absorbers functioning in a broad spectral (with allowance for the bathochromic shift) and energy range (with an incident energy density exceeding ~1 J/cm^2).

REFERENCES

1. *The Fullerenes*, Ed. by H. W. Kroto, J. E. Fischer, and D. E. Cox (Pergamon, Oxford, 1993).

2. A. Eletskiĭ and B. M. Smirnov, Usp. Fiz. Nauk **165** (9), 977 (1995) [Phys. Usp. **38**, 935 (1995)].

3. V. P. Belousov, I. M. Belousov, V. P. Budtov, *et al.*, Opt. Zh. **64** (12), 3 (1997) [J. Opt. Technol. **64**, 1081 (1997)].

4. N. V. Kamanina, L. N. Kaporskii, and B. V. Kotov, Opt. Commun. **152** (4-6), 280 (1998).

5. N. Kamanina, A. Barrientos, A. Leyderman, *et al.*, Mol. Mater. **13** (1-4), 275 (2000).

6. N. V. Kamanina, L. N. Kaporskii, V. N. Sizov, and D. I. Stasel'ko, Opt. Commun. **185** (4-6), 363 (2000).

7. Haiping Xia, Congshan Zhu, and Fuxi Gan, Proc. SPIE **3136**, 57 (1997).

8. Y. A. Cherkasov, N. V. Kamanina, E. L. Alexandrova, *et al.*, Proc. SPIE **3471**, 254 (1998).

9. N. V. Kamanina, Opt. Commun. **162** (4-6), 228 (1999).

10. F. Gutman and L. E. Lyons, *Organic Semiconductors* (Wiley, New York, 1967).

11. L. V. Gurvich, G. V. Karachevtsev, V. N. Kondrat'ev, Yu. A. Lebedev, V. K. Medvedev, V. K. Potapov, and Yu. S. Khodeev, *Energies of Chemical Bond Breakage, Ionization Potentials and Electron Affinity* (Nauka, Moscow, 1974).

12. A. V. Bazhenov, A. V. Gorbunov, M. Yu. Maksimuk, and T. N. Fursova, Zh. Éksp. Teor. Fiz. **112** (1), 246 (1997) [JETP **85**, 135 (1997)].

Translated by P. Pozdeev

A Bistable Optical Element Based on a Magnetic Grating

V. A. Tabarin and G. A. Shadrin

Surgut State University, Surgut, Tyumen oblast, 628400 Russia
Received January 16, 2001

Abstract—The results of a theoretical and experimental investigation of a bistable hybrid amplitude element based on a magnetic grating formed in the yttrium iron garnet (YIG) crystal are presented. In particular, the bistable operation mode, the feedback circuit parameters, and the element transfer characteristic are calculated. The experimental setup and the measurement procedure are described. © *2001 MAIK "Nauka/Interperiodica".*

This research is based on the effect of the domain structure ordering in an external magnetic field. It is known that a band domain structure (BDS) [1] can form in ferrite crystals with a quality factor exceeding unity. This structure may serve as a phase grating [2]. Processes induced in the magnetic grating (MG) by the varying magnetic field can be used for creating a bistable hybrid optical diffraction element [3].

Ferrite crystals usually possess a labyrinth domain structure [1] resulting from spontaneous magnetization in the absence of an external magnetic field. An external magnetic field applied perpendicularly to the surface of a ferrite sample causes ordering of the magnetic domains and, at a certain field intensity, a band domain structure is formed that consists of alternating bands with oppositely oriented domains. By increasing the field intensity, one can change the MG period and the domain structure dimensions. At a sufficiently large field intensity, the domain structure disappears and the crystal passes into a single-domain state.

The proposed bistable optical device operates as follows (Fig. 1). A laser radiation with the wavelength $\lambda = 1.15$ μm is incident onto an YIG disk *2*. The transmitted beam reflected by mirror *3* enters photodetector *5* whose rectified current is amplified in the feedback device (FD) *7* and applied to the Helmholtz coils *8*. Initially, the intensity of the radiation entering photodetector *6* is almost zero. If the intensity of the radiation incident onto disk *2* increases, the field generated by the coils also grows and, when its intensity exceeds a certain threshold level, creates band domains in the disk, which causes the appearance of a diffraction pattern. The intensity of the radiation focused by lens *4* and entering photodetector *6* is equal to the total intensity of the diffraction maxima of higher orders. Hence, the output intensity is a nonlinear function of the input intensity (Fig. 2). Recording this function with decreasing intensity of the input radiation, we will observe a hysteresis phenomenon.

Denote the intensity of the radiation incident on the disk (the input signal) by I_0. The radiation passed through the disk can be separated into two parts with intensities I_1 and I_2. Here I_1 is the intensity of the radiation entering photodetector *5*. This radiation is formed either by the zero-order maximum of the diffraction pattern or (in the case of a single-domain state) by the nondiffracted beam. The beam with intensity I_2 is formed by the radiation of the higher order maxima focused onto the sensitive area of photodetector *6* (Fig. 1).

The main setup parameters are as follows. The disk diameter and thickness are 3 and 0.4 mm, respectively. Intensities I_0, I_1, and I_2 are equal respectively to 10, 5, and 1.4 mW. The distance from disk to photodetector is 1 m.
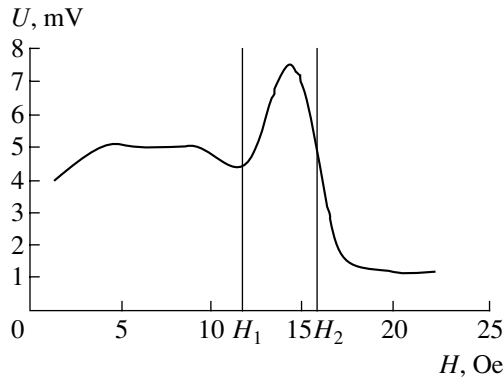
The intensity of light in the photodetector *6* plane can be found using the following formula [2]:

$$I_2 = I_0 \frac{\sin^2 u}{u^2} \frac{\sin^2 Nv}{\sin^2 v}, \qquad (1)$$

where $u = \dfrac{b}{\lambda}\sin\phi$ and $v = \dfrac{d}{\lambda}\sin\phi$ are the diffraction parameters, λ is the wavelength of the laser radiation, ϕ
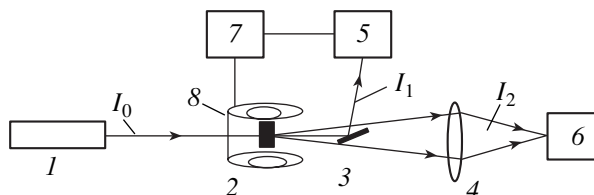

Fig. 1. Experimental setup: (*1*) He–Ne laser operating at $\lambda = 1.15$ μm; (*2*) main unit; (*3*) flat mirror; (*4*) collecting lens; (*5*, *6*) photodetectors (phototransistors); (*7*) feedback device (a current amplifier); (*8*) Helmholtz coils; (I_0) intensity of the input beam; (I_1) intensity of the zero-order maximum; (I_2) intensity of the higher-order diffraction maxima.

Fig. 2. Experimental curve of the intensity of the radiation entering photodetector *6* (Fig. 1) vs. the coil current. The labyrinth domain structure, the BDS, and the single-domain state are formed at currents ranging from 0 to H_1, from H_1 to H_2, and exceeding H_2, respectively.
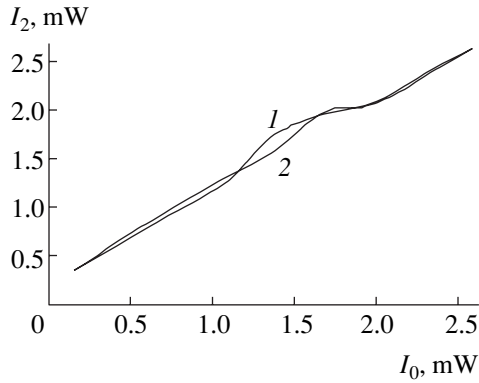
Fig. 3. Experimental plots of intensity I_2 vs. I_0. Curves *1* and *2* are obtained for increasing and decreasing I_0, respectively.
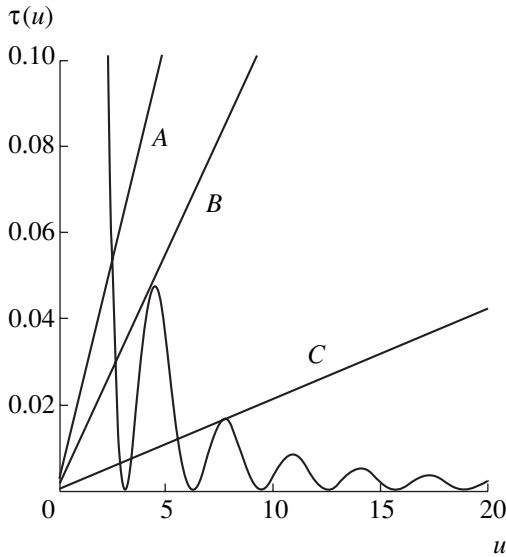
Fig. 4. Transmittance $\tau(u)$ of the optical element vs. the diffraction parameter u. Inclined straight lines connect parameters u and τ for various intensities I_0.

is the diffraction angle, d is the grating period, b is the size of domains oriented along the field, and N is the total number of bands across the sample diameter.

On the other hand, the intensity of the radiation incident onto photodetector *5* can be represented as:

$$I_1 = \gamma_1 I_0, \quad \gamma_1 = \exp(\alpha\delta), \tag{2}$$

where α is the absorption coefficient of the ferrite crystal and δ is the crystal thickness.

The transmittance of the bistable element studied is given by the formula

$$\tau = \frac{I_2}{I_0} = \frac{\sin^2 u}{u^2} \frac{\sin^2 Nv}{\sin^2 v}. \tag{3}$$

If $d \approx 2b$, relationship (3) can be rewritten as

$$\tau = \frac{I_2}{I_0} = \frac{\sin^2 u}{u^2} \frac{\sin^2 2Nu}{\sin^2 2u}. \tag{4}$$

Introduce an approximate dependence of the domain thickness b on the intensity I_1 in the form

$$b \approx b_0 + k_b I_1, \tag{5}$$

where b_0 is the width of domains oriented along the field in the just formed BDS.

Evidently, $k_b = k_1 k_2$, where k_1 is a coefficient related to the variation in the domain width with increasing intensity of magnetic field and k_2 is the gain of the feedback device.

For the setup used in this study, $k_1 = 250$ m/A, $k_2 = 50000$ A/W, and $k_b = 7.5 \times 10^6$ m/W. Using these data, we can write the relationship between the diffraction parameter u and the intensity I_1 as $u = u_0 + kI_1$, where u_0 is the diffraction parameter without feedback and $k = \gamma_1 \frac{k_b}{\lambda} \sin\phi = 6.8 \times 10^7$ 1/W.

In order to ensure a bistable operation, function $u(I)$ (a straight line) must intersect the plot of function $\tau(u)$ at no less than three points (Fig. 4). As can be seen from Fig. 3, the straight lines falling between lines *B* and *C* have three intersection points, which indicates the existence of a bistable operation mode.

The theoretical value of the maximum mean transmittance τ can be calculated using the formula [1]:

$$\tau = \frac{h}{h_{\mathrm{opt}}} \frac{4}{\pi^2} \sin^2(\arctan\Psi) \exp[-(2/\Psi)\arctan\Psi], \tag{6}$$

where h is the crystal thickness, $h_{\mathrm{opt}} = \theta_f^{-1}\arctan\Psi$, Ψ is the magnetooptic figure of merit, and θ_f is the Faraday rotation factor. Transmittance τ calculated by formula (7) equals 16%.

The experimental value of the maximum mean transmittance τ can be evaluated by formula $\tau = \gamma_2 \dfrac{I_2}{I_1}$, where $\gamma_2 = \exp(\beta\delta)$, β is the absorption coefficient of the optical system, and δ is the optical thickness. The experimental value of transmittance τ equals 14%. Thus, theoretical values of transmittance τ are in close agreement with experimental data.

The above results indicate the possibility of creating a bistable optical element based on a magnetic grating and an external optoelectronic feedback.

REFERENCES

1. V. V. Randoshkin and A. Ya. Chervonenkis, *Magnetooptics* (Énergoatomizdat, Moscow, 1990).

2. A. M. Balbashov and A. Ya. Chervonenkis, *Magnetic Materials for Microelectronics* (Énergiya, Moscow, 1979).

3. H. Gibbs, *Optical Bistability: Controlling Light with Light* (Academic, New York, 1985; Mir, Moscow, 1988).

Translated by A. Kondrat'ev

Trace Development Behind a Pulsed-Periodic Energy Source

V. N. Zudov

Institute of Theoretical and Applied Mechanics, Siberian Division, Russian Academy of Sciences,
Novosibirsk, Russia
e-mail: zudov@itam.nsc.ru
Received January 25, 2001

Abstract—A two-dimensional nonstationary problem of the trace development behind a pulsed-periodic energy source occurring in a supersonic flow is considered. © *2001 MAIK "Nauka/Interperiodica".*

Introduction. Problems pertaining to the nonstationary propagation of the shock waves and aeroacoustic perturbations in continuous media, which appear in various fields of research, are extremely difficult for both numerical and experimental modeling. Examples include the processes involved in body streamlining under the action of a pulsed-periodic energy supply from an external source. The control efficiency in this system is determined by a nonstationary flow structure [1]. Here, the experimental difficulties hinder observations of the trace development behind the thermal source. For this reason, a recourse to mathematical modeling is obviously necessary in order to provide for a better understanding and prediction of the observed phenomena. The use of a pulsed-periodic energy supply for stabilizing the process of burning and increasing the efficiency of fuels represents another possible application of the modeling results [1]. In this system, the energy source initiates the subsequent development of the combustion front.

The above problems are analogous to a certain extent, since both systems contain a localized thermal source at a given position in the flow. The results obtained in [1] for the influence of the energy pulse repetition frequency on the characteristics of streamlining for a cone and a hemisphere served as a base [2] for subsequently determining the aerodynamic characteristics of bodies streamlined by a nonstationary (with respect to parameters) gas flow. Distinctive features of this study are that (i) the main attention is paid to the formation and development of the trace structure behind an energy source, (ii) various source models are considered, and (iii) the Godunov method was specially developed in application to problems of this class.

This paper considers some elements of an original method developed by the author and presents the results of calculations for a localized energy source of variable power streamlined by a supersonic flow of the ideal gas. The model adopted is described by a system of two-dimensional nonstationary equations of gas dynamics with preset source power and its distribution in the localization region. Some questions pertaining to the numerical modeling of the effect of a pulsed thermal source on the supersonic flow structure are considered. The results of calculations yield distributions of the gasodynamic parameters for the nonstationary process under consideration. The calculations were performed by an explicit straightforward scheme without shock wave separation.

Problem formulation. A pulsed-periodic localized thermal energy source occurs in a supersonic flow of the ideal gas. The symmetry axis of the source is parallel to the velocity vector of the oncoming flow. The incident flow velocity is assumed to be constant across the flow and independent of time. The source power varies with time according to a preset law and depends on the source position in space. The task is to calculate a nonstationary variation of the gasodynamic characteristics of the flow for the time-dependent source power. The regimes with a time-independent (constant) source power are also considered.

The problem has been formulated within the framework of two-dimensional nonstationary Euler equations with a constant adiabatic exponent. The energy supply to the flow was modeled by a source term in the energy balance equation. The system of equations was solved using a scheme of the Godunov type. The numerical fluxes on the computational cell faces were determined using the HLLEM solver method [5, 6]. In this form, the scheme has a second order of accuracy with respect to the spatial variables.

Boundary conditions. The boundary conditions were realized using the layers of cells surrounding the computational region. The entrance (left-hand) boundary condition described constant parameters of a homogeneous supersonic flow. This boundary is sufficiently remote from the source, so that nonstationary perturbations originating at the pulsed source would not affect the oncoming flow. The entrance boundary conditions were changed in the course of computations. The outer (upper) boundary conditions admitted the possibility of a nonzero flux, which was achieved by setting the corresponding input and output Riemann invariants. This method allowed the perturbations propagating both inside the region under consideration (along the charac-
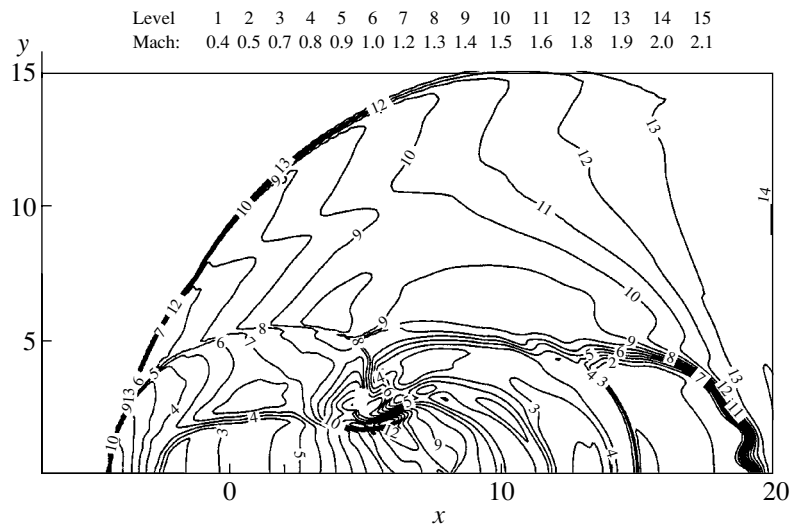
Fig. 1. The pattern of Mach number isolines for an elliptical energy source.

teristics corresponding to negative eigenvalues) and outside (along the characteristics corresponding to positive eigenvalues) to be taken into account. The exit (right-hand) boundary was also sufficiently remote from the source so that it would be possible to ignore the longitudinal gradients of the flow parameters. This boundary was characterized by nonreflecting boundary conditions [4]. Since the energy source axis is the axis of symmetry, the fluxes across this line are zero.

Results of calculations. The problem was solved for three models of the energy source. The first model used a source term (the same as in [3]) representing a spherical source with a Gaussian energy distribution and a time-dependent power. The calculation was performed for the following incident flow parameters: $\gamma = 1.4$; $M_\infty = 3.0$; source radius, 1; source center coordinates, $y = 0$, $x = 1$.

The source is switched on at the beginning of each period T for a time τ, so that it operates a pulsed-periodic mode. The source power is a periodic function of time. The numerical calculations were performed for a supercritical energy supply regime, in which case the flow contains regions of a subsonic flow pulsating with time. This flow exhibits some features that have to specially noted. First, the flux in and behind the energy supply region is characterized by a significantly (5- to 10-fold) reduced density. Second, there is a local zone of subsonic flow in and behind the energy supply region. The size of this zone, albeit pulsating with time, is insignificant and does not exhibit any evolution. The results of these model calculations confirmed the conclusions made in [3].

In the experiments with a pulsed-periodic laser described in [1], it was noted that the energy source formed in the flow had an extended shape. This conclusion was based on the analysis of the flow shadow photographs. Therefore, one of the possible approximations is offered by a source having the shape of an elongated

ellipsoid of revolution. The numerical calculations were performed for the following parameters: the Mach number of the incident flow, 2; the ratio of the ellipsoid semiaxes, 5 : 1; and the small semiaxis length, 1 mm. The effective calculated radius, outside of which no energy was supplied, was dependent on the coordinate x. Figure 1 shows the results of numerical calculations for this model, which were performed for a supercritical energy supply regime. This flow exhibits the following features. First, the flux in and behind the energy supply region is characterized by a more significantly (10- to 15-fold) reduced density. Second, there is a nonlocal zone of subsonic flow in and behind the energy supply region. The transverse dimensions of this region still pulsated with time, but the zone length was significant and even extended beyond the computation region boundary.

In a mathematical model of the energy source proposed previously [3], the dissipated energy is dependent on the density of the medium which sharply decreases in the course of the energy supply. The results of experiments reported in [1] showed that the energy absorbed by the medium during each pulse is approximately constant. This factor was taken into account in the third source model. In addition, the shape of the energy dissipation region was selected to represent a cylinder, which is most consistent with the experiment. According to the experimental data [1], the absorbed energy per pulse is $E_0 = 0.04$ J at a pulse repetition frequency of 45 kHz. In this case, the energy absorbed by a unit mass of the medium per unit time is

$$e = \frac{E_0}{m\tau}, \tag{1}$$

where m is the mass of the region to which the energy is supplied and τ is the time of energy dissipation. For the experimental conditions studied, $\tau = 1$ µs, $T = 22.2$ µs, the cylinder radius and length were 1 and 8.5 mm, respectively. The figure shows the results of these calcu-
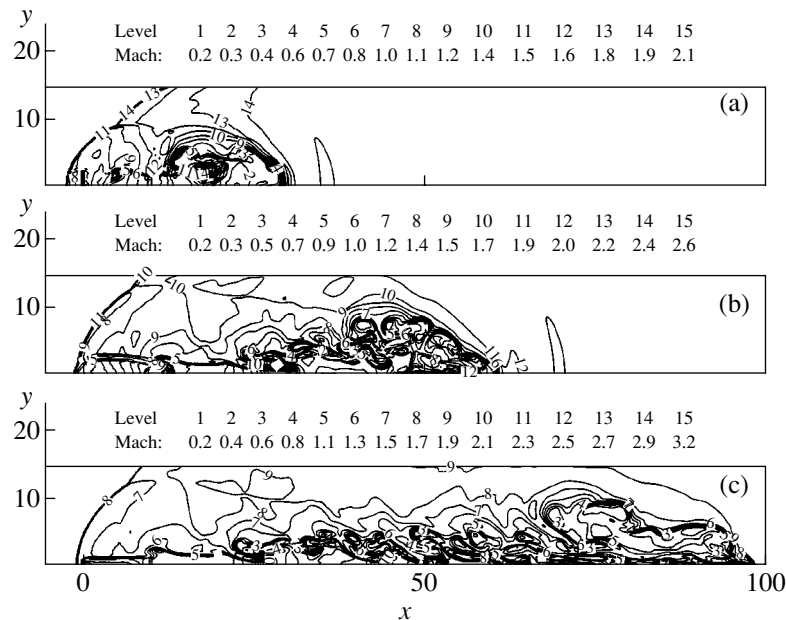
Fig. 2. The pattern of Mach number isolines for a cylindrical energy source at various time instants $t = 5.77$ (a); 14.95 (b); 25.67 (c).

lations demonstrating a distribution of the Mach number in the trace developed behind the model energy source.

The process of the trace development and evolution with time exhibits the following features. The source trace represents a cocurrent stream formed on the background of the total flow. The first to form is the trace head, which has a length of about 15–20 mm. This is followed by the trace body. The trace contour resembles an arrow moving along the flow away from the source (Fig. 2b) An important feature of the trace structure is the presence of vortex zones in the flow. Each vortex zone contains recurrent streams and is characterized by increased temperature. This is related to the fact that, for the pulse repetition frequency selected, the interval between sequential pulses was not large. The vortices are formed due to a difference in height between two sequential pulses. This difference appears because a thermal spot produced by the first pulse spreads and shifts down the flow, while the next pulse is just formed and occupies a significantly smaller space. The trace structure developed according to the proposed model qualitatively agrees with that observed in experiment. For a quantitative comparison between model calculation and experiment, it is necessary to measure the flow parameters in the trace.

Behind the cylindrical source (as well as behind the elliptical one), there is a significantly extended zone of subsonic flow. The transverse size of this zone (occupied by the vortex-like structures) increases with the distance from the source. For $x = 100$ mm (which is 11.8 times the source length), the trace radius is 15 times the source radius.

The presence of the vortex zones may serve as a good base for the ignition region formation. The vortex

zones would improve the mixing of fuel and oxidizer, while increased temperature in these zones would favor the ignition process.

Conclusions. (1) Selection of the source model significantly affects the results of numerical calculations. The formation of flow separation regions (vortex zones with recurrent streams) may serve a base for improved combustion processes.

(2) The source trace represents a cocurrent stream formed behind the energy source on the background of the total flow. The source energetics probably influences the cocurrent stream intensity.

(3) The pulse repetition frequency must be sufficiently high so as to ensure the permanent vortex zone formation.

REFERENCES

1. P. K. Tret'yakov and V. I. Yakovlev, Dokl. Akad. Nauk **365** (1), 58 (1999) [Dokl. Phys. **44**, 178 (1999)].

2. S. V. Guvernyuk and A. B. Samoĭlov, Pis'ma Zh. Tekh. Fiz. **23** (9), 1 (1997) [Tech. Phys. Lett. **23**, 333 (1997)].

3. P. Yu. Georgievsky and V. A. Levin, in *Proceedings of International Conference on the Methods of Aerophysical Research, Novosibirsk, 1998,* Part II, p. 58.

4. K. W. Thompson, J. Comput. Phys. **68** (1), 1 (1987).

5. A. Harten, B. Enquist, S. Osher, and S. R. Chakravarty, J. Comput. Phys. **71**, 231 (1987).

6. B. Einfeldt, SIAM J. Numer. Anal. **25** (2), 294 (1988).

Translated by P. Pozdeev

Nonparaxial Gaussian Beams: 3. Optical Vortices

A. V. Volyar, V. G. Shvedov, T. A. Fadeeva, and E. A. Konshu

Simferopol State University, Simferopol, Ukraine

Received July 18, 2000

Abstract—It is shown that an arbitrary nonparaxial laser vortex near a focal plane in the free space should be represented as a discrete superposition of intrinsic vortices possessing elliptical cross sections. The intrinsic vortices, albeit degenerate with respect to the propagation constants, exhibit a characteristic spectrum of singularities and topological phases. © *2001 MAIK "Nauka/Interperiodica".*

It is commonly accepted that optical vortices in the free space are characterized by two parameters: the topological charge κl ($l = 0, 1, 2, \ldots, k = \pm 1$ being the charge sign) and the spirality $\sigma = \pm 1$ indicating the direction of rotation of the electric vector [1]. However, this representation satisfactorily describes only the properties of paraxial laser beams with the crossover radii ρ much greater than the light wavelength λ ($\rho/\lambda \gg 1$). However, there are many practically important cases in which the optical fields are characterized by the transverse dimensions comparable with the wavelength. An example is offered by fields in the low-mode optical fibers or in the vicinity of the focal plane of a short-focus microobjective. The fields of optical vortices in weakly guiding fibers were studied in sufficient detail elsewhere [2].

The properties of wave fields in the focal plane of a strongly focused beam is of special interest even from a theoretical standpoint: a satisfactory description of these waves showing acceptable agreement with the experiment can be obtained neither in the beam optics approximation nor within the framework of the popular quantum-mechanical WKB method. The reason is that the focal wave fields are essentially vectorial, not admitting a scalar description. Moreover, the presence of stationary (cusp) points and anomalous phases separates these fields off into a special class of wave caustics, relates them to the optical catastrophes of certain types [3], and stipulates using a definite approach to their structural analysis.

The purpose of this study was to analyze both theoretically and experimentally the rigorous solutions to the Maxwell equations describing the optical vortex modes beyond the paraxial barrier.

Let us first obtain an exact solution to the scalar Helmholtz wave equation

$$(\nabla^2 + k^2)\Psi = 0 \qquad (1)$$

in the form of a wavefunction

$$\Psi = A j_m(kR) P_m^l(\cos\theta) e^{il\varphi}, \qquad (2)$$

where $j_m(x)$ is the mth order Bessel spherical function of the first kind, $P_m^l(x)$ is the Legendre associated polynomial ($m = 0, 1, 2, \ldots; l = 0, 1, 2, \ldots$), and Ψ is the azimuthal angle. We select the radius R so as to provide that the special z axis would be continued to the complex plane: $R = \sqrt{r^2 + (z + iz_0)^2}$, where $r^2 = x^2 + y^2$, z_0 is a real parameter and $\cos\theta = (z + iz_0)/R$.

Consider a nonparaxial optical vortex propagating in the positive direction of the z axis in the free space. The boundary conditions are selected in the approximate form according to Davis [4], which allow the exact solution (2) to pass into a solution valid for a paraxial beam in the entire paraxial region for $kz_0 \longrightarrow \infty$. If the paraxial solution is taken in the form

$$\tilde{\Psi} = \frac{1}{\zeta}\left(\frac{x + iky}{\rho\zeta}\right)^l \exp\left(-\frac{r^2}{\rho^2\zeta}\right), \quad \zeta = 1 - i\frac{z}{z_0}, \qquad (3)$$

then the exact solution (2) with $l = m$ passes into a paraxial solution (3) as $kz_0 \longrightarrow \infty$, provided that $A_l = \dfrac{2^l l!}{(2l)! i^l}\dfrac{kz_0}{\sinh(kz_0)}$. Moreover, this transition is also possible for all $m > l$. However, this implies that every paraxial optical vortex with a topological charge l corresponds to an infinite number of discrete states (2). Each exact solution (2) represents a scalar field potential for the eigenmode of a nonparaxial optical vortex. This situation is analogous to the case of an optical fiber excited by the field of a nonparaxial laser beam. The beam field can be expanded into series with respect to eigenmodes of the fiber. In our case the field of the paraxial optical vortex should be represented as a series

The mode fields of nonparaxial optical vortices ($m = l$)

Electric field **e**

Mode	e_x	e_y	e_z
$LV(e_y) + i\sigma LV(e_x)$	$\sigma k\mathcal{R}^l Z F_{l+1}$	$ik\mathcal{R}^l Z F_{l+1}$	$kl\mathcal{R}^{l-1}F_l(\sigma - \kappa)$ $-\sigma kr^{1-\sigma\kappa}\mathcal{R}^{l+\sigma\kappa}F_{l+1}$
$LV(h_y) + i\sigma LV(h_x)$	$(l(l-1)\mathcal{R}^{l-2}(1-\sigma\kappa) + k^2\mathcal{R}^l)F_l$ $-(l\mathcal{R}^{l-1}(x[2-\sigma\kappa]+i\sigma y)$ $+\mathcal{R}^l)F_{l+1} + xr^{1-\sigma\kappa}\mathcal{R}^{l+\sigma\kappa}F_{l+2}$	$(il(l-1)\mathcal{R}^{l-2}(\kappa-\sigma) + i\sigma k^2\mathcal{R}^l)F_l$ $+(l\mathcal{R}^{l-1}(y[2\sigma\kappa-1]-i\kappa x)$ $-i\sigma\mathcal{R}^l)F_{l+1} + yr^{1-\sigma\kappa}\mathcal{R}^{l+\sigma\kappa}F_{l+2}$	$-Z(l(1-\sigma\kappa)\mathcal{R}^{l-1}F_{l+1}$ $-r^{1-\sigma\kappa}\mathcal{R}^{l+\sigma\kappa}F_{l+2})$
TE	$kl\kappa\mathcal{R}^{l-1}F_l + ik\mathcal{R}^l y F_{l+1}$	$kl\mathcal{R}^{l-1}F_1 - ik\mathcal{R}^l x F_{l+1}$	0
TM	$-Z(l\mathcal{R}^{l-1}F_{l+1} - \mathcal{R}^l x F_{l+2})$	$-Z(il\kappa\mathcal{R}^{l-1}F_{l+1} - \mathcal{R}^l y F_{l+2})$	$\mathcal{R}^l(k^2 F_l - F_{l+1} + Z^2 F_{l+2})$

Magnetic field **h**

Mode	$h_x/\sqrt{\varepsilon_0/\mu_0}$	$h_y/\sqrt{\varepsilon_0/\mu_0}$	$h_z/\sqrt{\varepsilon_0/\mu_0}$
$LV(e_y) + i\sigma LV(e_x)$	$(l(l-1)\mathcal{R}^{l-2}(1-\sigma\kappa) + k^2\mathcal{R}^l)F_l$ $-(l\mathcal{R}^{l-1}(x[2-\sigma\kappa]+i\sigma y)$ $+\mathcal{R}^l)F_{l+1} + xr^{1-\sigma\kappa}\mathcal{R}^{l+\sigma\kappa}F_{l+2}$	$(il(l-1)\mathcal{R}^{l-2}(\kappa-\sigma) + i\sigma k^2\mathcal{R}^l)F_l$ $+(l\mathcal{R}^{l-1}(y[2\sigma\kappa-1]-i\kappa x)$ $-i\sigma\mathcal{R}^l)F_{l+1} + yr^{1-\sigma\kappa}\mathcal{R}^{l+\sigma\kappa}F_{l+2}$	$-Z(l(1-\sigma\kappa)\mathcal{R}^{l-1}F_{l+1}$ $-r^{1-\sigma\kappa}\mathcal{R}^{l+\sigma\kappa}F_{l+2})$
$LV(h_y) + i\sigma LV(h_x)$	$-\sigma k\mathcal{R}^l Z F_{l+1}$	$-ik\mathcal{R}^l Z F_{l+1}$	$-kl\mathcal{R}^{l-1}F_l(\sigma-\kappa)$ $+\sigma kr^{1-\sigma\kappa}\mathcal{R}^{l+\sigma\kappa}F_{l+1}$
TE	$-Z(l\mathcal{R}^{l-1}F_{l+1} - \mathcal{R}^l x F_{l+2})$	$-Z(il\kappa\mathcal{R}^{l-1}F_{l+1} - \mathcal{R}^l y F_{l+2})$	$\mathcal{R}^l(k^2 F_l - F_{l+1} + Z^2 F_{l+2})$
TM	$-kl\kappa\mathcal{R}^{l-1}F_l - ik\mathcal{R}^l y F_{l+1}$	$-kl\mathcal{R}^{l-1}F_1 + ik\mathcal{R}^l x F_{l+1}$	0

$$\Psi_\| = J_l(R)\left(\frac{\mathcal{R}}{R}\right)^l, \; F_l(R) = \frac{j_l(R)}{R^l}, \; \mathcal{R} = (x + i\kappa y), \; Z = z + iz_0, \; \sigma = \pm 1, \; \kappa = \pm 1$$

with respect to the eigenmodes of a nonparaxial beam. However, in contrast to the fiber case, the intrinsic fields of a nonparaxial vortex are degenerate with respect to the quantum number k since the beam in the free space propagates with the speed of light c. As will be shown below, the beam modes are nondegenerate with respect to both the spectrum of phase singularities and the spectrum of topological phases.

Using a standard method for the passage from scalar Whittaker potentials to vectorial wave fields [5], we arrive at the expressions for eigenmodes of a nonparaxial vortex (see table). There are six groups of fields: even $LV(e_x)$ and $LV(e_y)$; odd $LV(h_x)$ and $LV(h_y)$; and azimuthally-symmetric TE and TM modes. Figure 1 shows typical intensity distributions in the focal plane for the even and odd modes with $l = m = 1$.

It is necessary to emphasize certain important features of the eigenmodes of a nonparaxial vortex. First, the state of the optical vortex is characterized by a set of three quantities: $\{l, \sigma, m\}$. Second, the intensity distributions for the modes with predominantly linear polarization loses axial symmetry both in the vicinity of the focal caustic and far from the focal plane. A detailed analysis showed that the field symmetry is bro-

ken as a result of the nonsymmetric distribution of negative energy fluxes in the region of phase singularities (Airy's fringes). In fact, the Poynting vector field lines in these zones appear as loops and circles. This modification of the field symmetry leads to changes in the state of polarization. Far from the focal plane, the light becomes inhomogeneously polarized. In order to restore a nearly axial symmetry of the nonparaxial vortex field, it is convenient to use a superposition of the even modes $LV(e_y) + i\sigma LV(e_x)$ (Fig. 1c) or the odd modes $LV(h_y) + i\sigma LV(h_x)$. An important circumstance is the asymmetry of electric and magnetic fields and the loss of phase synchronism between these fields, which is manifested in the topological phase difference.

The above analysis implies a difference in behavior of the intrinsic and nonintrinsic fields in the vicinity of the focal caustic, which can be verified experimentally. Indeed, if a paraxial laser beam possesses the intensity and polarization distributions structurally close to those of the eigenmode field, then the beam structure near the focal plane will be stable with respect to small increments in both z and r coordinates. Otherwise, the field structure will exhibit sharp variations. These qualitative
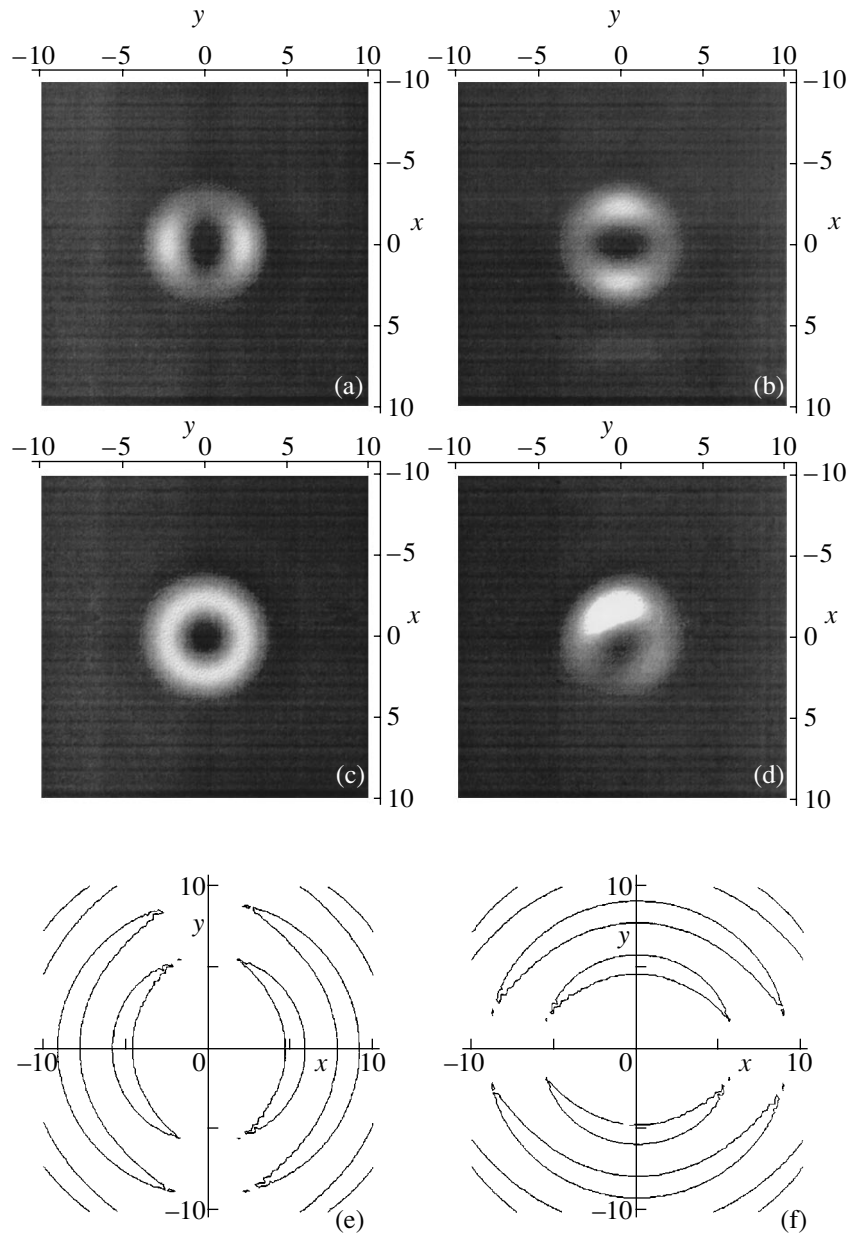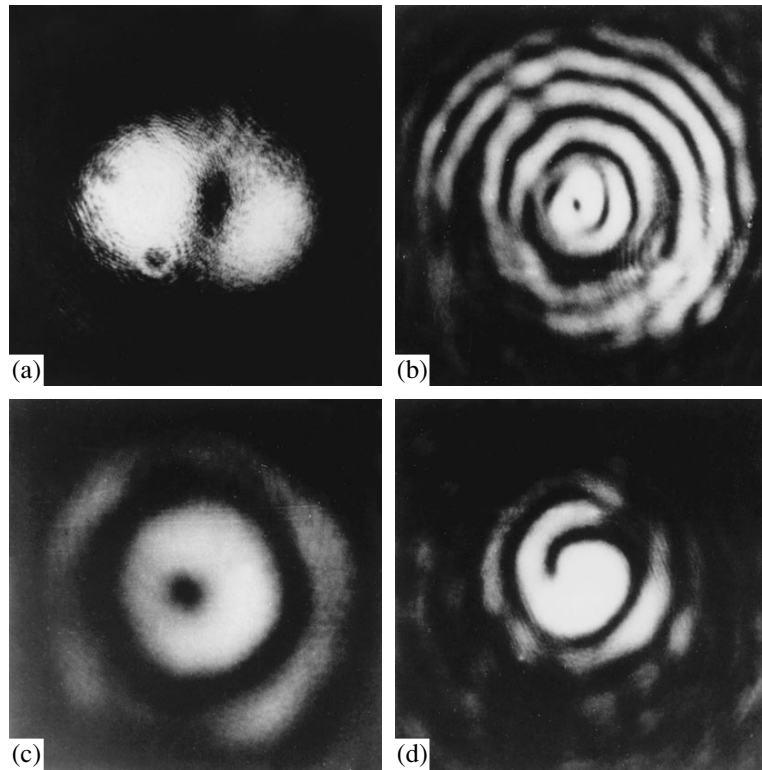
Fig. 1. The maps of intensity distribution in the focal plane for the linearly polarized (a) $LV(e_x)$ and (b) $LV(e_y)$ eigenmodes, (c) circularly polarized $LV(e_y) + iLV(e_x)$ modes, and (d) a superposition of modes with different weights $0.35LP(e_y) - LV(e_y) + 0.78LV(e_x)$; the lines of phase singularities $P_z(x, y) = 0$ in the phase plane $z = 0$ ($kz_0 = 1$) for (e) $LV(e_x)$ and (f) $LV(e_y)$ eigenmodes.

considerations served a base for the experiments descried below.

We used a fundamental-frequency Gaussian beam emitted by a 40-mW He–Ne laser operating at a wavelength of $\lambda = 0.6328$ μm. A 100-μm-thick plane-parallel glass plate was introduced into the beam so that the plate right angle was tangent to the beam axis. By slightly tilting the plate, it was possible to obtain an optical vortex with an elliptical cross section in the beam behind the diaphragm. The optical vortex formation in the initially smooth beam is caused by the field singularity breakage from a sharp edge of the plate or

from the wedge formed by the plate edges. Using this method, it was possible to obtain optical fields with the intensity distributions depicted in Fig. 2a and 2c. The structure of these fields corresponds to $LV(e_y)$ and $LV(h_y)$ modes (Figs. 1a and 1b).

Then the beam with this field structure was directed into a holographic microscope and focused with a 100× microobjective. Another 100× microobjective projected the focal image onto the observation plane. If the field structure in the observation plane exhibits no variations in response to slight displacements of the second

Fig. 2. Microphotographs of the field intensity distribution in (a, c) the paraxial region and (b, d) in the focal region of a $100^\times$ microobjective: (a) $LP(e_y)$ eigenmode analog at the microscope entrance; (b) $LP(e_y)$ eigenmode in the focal plane; (c) paraxial optical vortex with slightly shifted dislocation ($l = 1$); (d) the field of this paraxial vortex in the focal plane.

microobjective, we may conclude that the initial field corresponds with high precision to the eigenmode of a nonparaxial vortex (Fig. 2b). On the contrary, a linearly polarized paraxial vortex (Fig. 2c) entering the microscope leads to breakage of the beam structure in the vicinity of the focal caustic (Fig. 2d). A comparison of the field shows that an arbitrary optical vortex field behind the paraxial barrier can be represented as a sum of eigenmodes.

REFERENCES

1. A. V. Volyar, V. Z. Zhilaĭtis, V. G. Shvedov, *et al.*, Opt. Atmos. Okeana **11** (11), 1199 (1998).

2. K. N. Alexeyev, T. A. Fadeyeva, A. V. Volyar, and M. S. Soskin, Semicond. Phys. Quantum Electron. Optoelectron. **1** (1), 1 (1998).

3. T. Poston and I. Stewart, *Catastrophe Theory and Its Applications* (Pitman, London, 1978; Mir, Moscow, 1980).

4. L. W. Davis, Phys. Rev. A **19** (3), 1177 (1979).

5. G. P. Agrawal and P. N. Patanyak, Phys. Rev. A **22** (3), 1159 (1980).

Translated by P. Pozdeev